Dissertation

Characterization of the structural and functional impact of autism-associated SHANK3 missense mutations

Zur Erlangung des Doktorgrades der Naturwissenschaften am Fachbereich Chemie der Fakultät für Mathematik, Informatik und Naturwissenschaften der Universität Hamburg

**doctor rerum naturalium
(Dr. rer. nat.)**

im   März 2022

eingereichte Dissertation,

vorgelegt von   M.Sc. Michael Bucher

Gutachter

Prof. Dr. Wolfram Brune

Institute for Biochemistry and Molecular Biology, University of Hamburg, Hamburg, Germany

Dr. Froylan Calderon de Anda

RG Neuronal Development, Center for Molecular Neurobiology Hamburg, University Medical Center Hamburg-Eppendorf, Hamburg, Germany

Disputation

01. Juli 2022

Mitglieder der Prüfungskommission

Prof. Dr. Kay Grünewald

Institute for Biochemistry and Molecular Biology, University of Hamburg, Center for Structural Systems Biology, Hamburg

Prof. Dr. Marina Mikhaylova

RG Neuronal Protein Transport, Center for Molecular Neurobiology Hamburg, University Medical Center Hamburg-Eppendorf, Hamburg, Germany

RG Optobiology, Institute of Biology, Humboldt-University Berlin, Germany

Prof. Dr. Henning Tidow

Institute for Biochemistry and Molecular Biology, University of Hamburg, Hamburg, Germany

Practical work was conducted between July 2017 and December 2021 in the research group "Neuronal Protein Transport" at the Center for Molecular Neurobiology Hamburg (ZMNH), University Medical Center Hamburg-Eppendorf in frame of the Graduate Program in Molecular Biology.

Supervisors

Prof. Dr. Marina Mikhaylova

RG Neuronal Protein Transport, Center for Molecular Neurobiology Hamburg, University Medical Center Hamburg-Eppendorf, Hamburg, Germany

Prof. Dr. Wolfram Brune

Institute for Biochemistry and Molecular Biology, University of Hamburg, Hamburg, Germany

Co-Supervisors

Prof. Dr. Matthias Kneussel

Institute for Molecular Neurogenetics, Center for Molecular Neurobiology Hamburg, University Medical Center Hamburg-Eppendorf, Hamburg, Germany

Dr. Michael R. Kreutz

RG Dendritic Organelles and Synaptic Function, Center for Molecular Neurobiology Hamburg, University Medical Center Hamburg-Eppendorf, Hamburg, Germany

Publications

Direct and indirect effects of tubulin post-translational modifications on microtubule stability: insights and regulations
Bär J., Popp Y., **Bucher M.**, Mikhaylova M.
Biochim. Biophys. Acta, Mol. Cell Res., 2022, Review
DOI: 10.1016/j.bbamcr.2022.119241

Caldendrin and myosin V regulate synaptic spine apparatus localization via ER stabilization in dendritic spines
Konietzny A., Grendel J., Kadek A., **Bucher M.**, Han Y., Hertrich N., Dekkers D.H.W., Demmers J.A.A., Grünewald K., Uetrecht C., Mikhaylova M.
The EMBO Journal, 2021, Research Article, DOI: 10.15252/embj.2020106523

Autism associated *SHANK3* missense point mutations impact conformational fluctuations and protein turnover at synapses
Bucher M., Niebling S., Han Y., Molodenskiy D., Hassani Nia F., Kreienkamp H.J., Svergun D., Kim E., Kostyukova A.S., Kreutz M.R., Mikhaylova M.
eLife, 2021, Research Article, DOI: 10.7554/eLife.66165

Molecular dynamics simulations of ASD-associated SHANK3 variants.
Niebling S., **Bucher M**. and Mikhaylova, M.
Bio-protocol, 2021; bio-protocol.org/prep1479.

SATB2-LEMD2 interaction links nuclear shape plasticity to regulation of cognition-related genes
Feurle P., Abentung A., Cera I., Wahl N., Ablinger C., **Bucher M.**, Stefan E., Sprenger S., Teis D., Fischer A., Laighneach A., Whitton L., Morris D. W., Apostolova G., & Dechant G.
The EMBO Journal, 2021, Research Article, DOI: 10.15252/embj.2019103701

- *This publication did not result from practical work conducted in the frame of this dissertation but relates to previous work, which was done as part of a master thesis project.*

Cytoskeletal makeup of the synapse: Shaft versus spine
Bucher M., Fanutza T., Mikhaylova M.
Cytoskeleton, 2020, Review, DOI: 10.1002/cm.21583

Abstract

Autism-spectrum disorders (ASDs) constitute a set of complex neurodevelopmental disorders associated with characteristic social cognition and communication impairments as well as repetitive behaviors, restricted interests, or intellectual disabilities. These phenotypic traits may additionally be accompanied by other neurological or psychiatric co-morbidities such as epilepsy or depression and generally show a strong variance in their occurrence and severity. It is estimated that approximately 1% of the worldwide population may be affected by ASD, underlining the clinical relevance and the need to understand the mechanisms and origins of ASDs. Due to the high frequency of autism-associated mutations occurring in genes coding for synaptic proteins, ASDs are increasingly understood as synaptopathies. Thereby, synapses constitute the central neuronal communication sites whose structure and function strongly depends on their molecular integrity. One of the central molecular regulators of excitatory glutamatergic synapses is the post-synaptic scaffolding protein SH3 and multiple ankyrin repeat domains protein 3 (SHANK3), which links ionotropic and metabotropic glutamate receptors in the post-synaptic plasma membrane to the synaptic actin cytoskeleton. This functional versatility is reflected by the interaction of SHANK3 with multiple synaptic signaling proteins covering a variety of different pathways. Consequently, mutations in the *SHANK3* gene have been implicated in the development of both syndromic and idiopathic ASDs. Besides copy-number variants (CNVs) and truncating mutations, numerous autistic patients were described carrying SHANK3 missense mutations for which several different pathogenic processes including modified dendritic spine morphologies, altered SHANK3 ligand binding affinities, epigenetic mechanisms or altered SHANK3 phosphorylation states have been described. A comprehensive study linking the molecular impact of such missense mutations on the structure and dynamics of SHANK3 itself to the corresponding synaptic phenotype is however largely missing. The present work therefore aims to provide insight into i) structural perturbations of SHANK3 elicited by two selected missense-mutations, R12C and L68P, previously identified in autistic patients, both located within the same domain ii) resulting alterations in the synaptic interactome, subcellular localization and dynamics of SHANK3 to identify new signaling pathways and cellular alterations relevant for the development of ASD and iii) the cellular and network impact of the L68P mutation in a corresponding knock-in mouse model. Using a broad range of techniques including small-angle X-ray scattering (SAXS), nano differential scanning fluorimetry (nanoDSF), circular dichroism (CD) and fluorescence spectroscopy as well as molecular dynamics (MD) simulations, structural alterations within SHANK3 were characterized and revealed changes in the folding, structural stability, and nanosecond peptide backbone dynamics of SHANK3 mutants. Furthermore, a novel concentration-dependent mode of SHANK3 homodimerization was identified by SAXS, which is not impaired by the studied mutations. Overall, mutation-induced structural changes are highlighted as initial breaking points for pathogenic processes. Thereby, the clear distinguishability of structural alterations induced by the respective mutation serves as potential explanation for the broad range of observed mutation-induced pathological alterations. These include, among others, a rearrangement of the synaptic interactome as mass spectrometry demonstrated both gain- and loss-of-function for several SHANK3 interaction partners, from which a potentially new ASD-associated pathogenic pathway could be identified involving the

interaction of SHANK3 with SynGAP. On a cellular level, total internal reflection-fluorescence recovery after photobleaching (TIRF-FRAP) experiments showed that the R12C mutation significantly increases the diffusional mobility of SHANK3 in primary hippocampal neurons and revealed the ability of both mutants to alter the mobility of individual interaction partners such as cortactin. An increased tendency to form dendritic clusters, which partially represent active synapses, was additionally evident especially for the L68P mutation. Finally, morphological abnormalities of the post-synaptic density (PSD) nanostructure as well as reduced numbers of excitatory and inhibitory post-synaptic puncta were identified in a humanized mouse model of ASD carrying the L68P mutant human *SHANK3* knock-in. These cellular alterations were ultimately found to result in synaptic transmission impairments of heterozygous and homozygous *SHANK3* L68P mice. Collectively, the present work provides a comprehensive set of data on a molecular, cellular and functional level to correlate missense mutation-induced alterations in the structure and dynamics of SHANK3 to the corresponding synaptic phenotype. This puts ASD elicited by SHANK3 missense mutations in the context of conformational diseases and might thus contribute to the design and development of new therapeutic strategies involving the use of pharmacological chaperones aiming to reconstitute the native protein fold to alleviate the associated disease phenotype.

Zusammenfassung

Autismus-Spektrum-Störungen (ASDs) stellen eine Reihe komplexer Entwicklungs-störungen des Nervensystems dar, die mit charakteristischen Beeinträchtigungen der sozialen Kognition und Kommunikation sowie mit repetitiven Verhaltensweisen, eingeschränkten Interessen oder intellektuellen Defiziten assoziiert sind. Zusätzlich können diese phänotypischen Merkmale gemeinsam mit anderen neurologischen oder psychiatrischen Komorbiditäten wie Epilepsie oder Depression auftreten, variieren jedoch generell stark in deren Auftreten und Schweregrad. Die weltweite Prävalenz von ASDs wird auf etwa 1% geschätzt, was deren klinische Relevanz und die Notwendigkeit, die entsprechenden Mechanismen und Ursprünge der Erkrankung zu verstehen, unterstreicht. Aufgrund der starken Häufung Autismus-assoziierter Mutationen in Genen, die synaptische Proteine kodieren, werden ASDs zunehmend als „Synaptopathien" verstanden. Synapsen repräsentieren dabei die zentralen neuronalen Kommunikationsstellen, deren Struktur und Funktion stark von deren molekularer Integrität abhängt. Einer der wichtigsten molekularen Regulatoren exzitatorischer glutamaterger Synapsen ist dabei das post-synaptische Gerüstprotein SHANK3, welches ionotrope und metabotrope Glutamatrezeptoren in der post-synaptischen Plasmamembran mit dem synaptischen Aktin-Zytoskelett verknüpft. Diese funktionelle Vielseitigkeit zeigt sich in der Interaktion von SHANK3 mit einer großen Bandbreite synaptischer Signalproteine, die eine Vielzahl verschiedener Signaltransduktionswege abdecken. Mutationen in dem *SHANK3* Gen wurden dementsprechend sowohl mit der Entwicklung syndromischer als auch idiopathischer Formen von ASDs in Verbindung gebracht. Neben Patienten mit veränderter Kopienzahl von *SHANK3* oder trunkierenden Mutationen wurden auch zahlreiche autistische Patienten beschrieben, die SHANK3 Missense-Mutationen tragen. Für letztere wurden mehrere verschiedene pathogene Prozesse beschrieben, wie die Veränderung der Morphologie dendritischer Spines, veränderte Affinitäten von SHANK3 Liganden, epigenetische Mechanismen oder auch Veränderungen der Phosphorylierung von SHANK3. Eine umfassende Studie, die molekulare Auswirkungen solcher Missense-Mutationen auf die Struktur und Dynamik von SHANK3 untersucht und mit dem entsprechenden synaptischen Phänotyp verbindet, fehlt jedoch weitgehend.

Die vorliegende Arbeit soll daher einen Einblick in die folgenden Aspekte geben: i) strukturelle Veränderungen von SHANK3, die durch zwei ausgewählte Missense-Mutationen, R12C und L68P, welche zuvor in autistischen Patienten identifiziert wurden und in derselben Proteindomäne lokalisiert sind, hervorgerufen werden ii) daraus resultierende Veränderungen des synaptischen Interaktoms, der subzellulären Lokalisation und Dynamik von SHANK3, um neue Signaltransduktionswege und andere zelluläre Veränderungen zu identifizieren, die für die Entwicklung von ASDs relevant sind und iii) den Einfluss der L68P Mutation auf die Struktur und Funktion von hippocampalen Nervenzellen in einem entsprechenden „knock-in" Mausmodell. Der individuelle Einfluss der R12C und L68P Mutation auf die Struktur von SHANK3 wurde mit Hilfe verschiedener Methoden wie Kleinwinkel-Röntgenstreuung (SAXS), Nano-Differential-Scanning-Fluorimetrie (nanoDSF), Zirkulardichroismus (CD)- und Fluoreszenzspektroskopie sowie Molekulardynamik (MD)-Simulationen im Detail untersucht und zeigte Veränderungen in der Faltung, strukturellen Stabilität und Nanosekunden-Dynamik des Grundgerüsts mutierter Proteine. Des Weiteren wurde

mittels SAXS eine neue, konzentrationsabhängige Art der SHANK3 Homodimerisierung entdeckt, die durch keine der beiden untersuchten Mutationen beeinträchtigt wurde. Insgesamt werden mutationsinduzierte strukturelle Veränderungen als Ausgangspunkt für pathogene Prozesse hervorgehoben. Dabei dient die klare Unterscheidbarkeit der durch die jeweilige Mutation hervorgerufenen strukturellen Veränderungen als mögliche Erklärung für das breite Spektrum der beobachteten mutationsbedingten pathologischen Veränderungen. Dazu gehört unter anderem eine Umstrukturierung des synaptischen Interaktoms, da mittels Massenspektrometrie sowohl ein Funktionsgewinn als auch ein Funktionsverlust für mehrere SHANK3-Interaktionspartner nachgewiesen werden konnte, wodurch ein potenziell neuer ASD-assoziierter pathogener Signaltransduktionsweg identifiziert werden konnte, der die Interaktion von SHANK3 mit SynGAP beinhaltet. Auf zellulärer Ebene zeigten TIRF-FRAP-Experimente einerseits, dass die R12C-Mutation die Diffusionsmobilität von SHANK3 in primären Hippocampus-Neuronen signifikant erhöht und andererseits, dass beide Mutanten in der Lage sind die Mobilität einzelner Interaktionspartner wie Cortactin zu verändern. Zusätzlich konnte insbesondere für die L68P Mutation eine verstärkte Tendenz zur Bildung von dendritischen Clustern nachgewiesen werden, welche zum Teil aktive Synapsen darstellen. Schließlich wurden morphologische Veränderungen der Nanostruktur der post-synaptischen Dichte (PSD) sowie eine verringerte Anzahl exzitatorischer und inhibitorischer post-synaptischer Punkte in einem humanisierten ASD-Mausmodell identifiziert, das die L68P-Mutante des menschlichen *SHANK3* Gens trägt. Diese zellulären Veränderungen resultierten in einer Beeinträchtigung der synaptischen Transmission bei heterozygoten und homozygoten *SHANK3* L68P Mäusen. Insgesamt liefert die vorliegende Arbeit umfassende Daten auf molekularer, zellulärer und funktioneller Ebene und korreliert die durch Missense-Mutationen hervorgerufenen Veränderungen in der Struktur und Dynamik von SHANK3 mit dem entsprechenden synaptischen Phänotyp. Dies stellt ASDs, die durch SHANK3 Missense-Mutationen verursacht werden, in den Kontext von Konformationskrankheiten und könnte somit zur Entwicklung neuer therapeutischer Strategien beitragen, die den Einsatz pharmakologischer Chaperone zur Wiederherstellung der nativen Proteinfaltung vorsehen, um den damit verbundenen Krankheitsphänotyp zu lindern.

Contents

List of Figures

Abbreviations

AMPAR	2-amino- 3-(3-hydroxy-5-methyl-isoxazol-4-yl) propanoic acid receptor
ANOVA	Analysis of Variance
ASD	Autism-spectrum disorder
CaM	Calmodulin
CaMKII	Calcium/calmodulin-dependent protein kinase II
CD	Circular dichroism
CORAL	Complexes with random loops
DIV	Day(s) in vitro
DMEM	Dulbecco's Modified Eagle's Medium
DTT	Dithiothreitol
E/I	Excitation/Inhibition
EEG	Electroencephalography
eGFP	Enhanced green fluorescent protein
F-actin	Filamentous actin
FCS	Fetal calf serum
FRAP	Fluorescence recovery after photobleaching
GABA	Gamma-aminobutyric acid
GKAP	Guanylate kinase-associated proteins
HEK293T	Human embryonic kidney cell line expressing the SV40 T-antigen
ICC	Immunocytochemistry
iGluR	Ionotropic glutamate receptor
IP	Immunoprecipitation
LTD	Long-term depression
LTP	Long-term potentiation
MAGUK	Membrane-associated guanylate kinase
MDS	Molecular dynamics simulations
mEPSC.	Miniature excitatory post-synaptic current
mGluR	Metabotropic glutamate receptor
mIPSC	Miniature inhibitory post-synaptic current
nanoDSF	Nano differential scanning fluorimetry
NMDAR	N-methyl-D-aspartate receptor
ORF	Open reading frame

PBS	Phosphate-buffered saline
PCR	Polymerase chain reaction
PDDF	Pair distance distribution function
PLL	Poly-L-lysine
PPI	Protein:Protein-interaction
PSD	Post-synaptic density
RT	Room temperature
SAPAP1	SAP90/PSD-95-associated protein 1
SAXS	Small-angle X-ray scattering
SEC	Size-exclusion chromatography
SEM	Standard error of the mean
SHANK3	SH3 and multiple ankyrin repeat domains protein 3
STED	Stimulated emission depletion
SUMO	Small ubiquitin-like modifier
SynGAP	Synaptic Ras GTPase-activating protein
TEM	Transmission electron microscopy
TIRF	Total internal reflection
UV	Ultraviolet
WT	Wildtype

1 Introduction

1.1 Neuronal structure and function

1.1.1 Neuronal morphology

As a highly plastic organ, the brain actively produces behavior and cognitive states, senses the environment, and organizes perception, which is achieved by a huge number of neuronal circuits or networks differing in their structure and function (Figure 1A). The precise regulation of excitatory and inhibitory signals within a neuronal network allows fine tuning of network activity and output, which is essential for physiological brain function (Figure 1B). These circuits comprise a plethora of anatomically and functionally interconnected nerve cells or neurons, which constitute the basic signaling unit of the brain (Kandel, 2013).
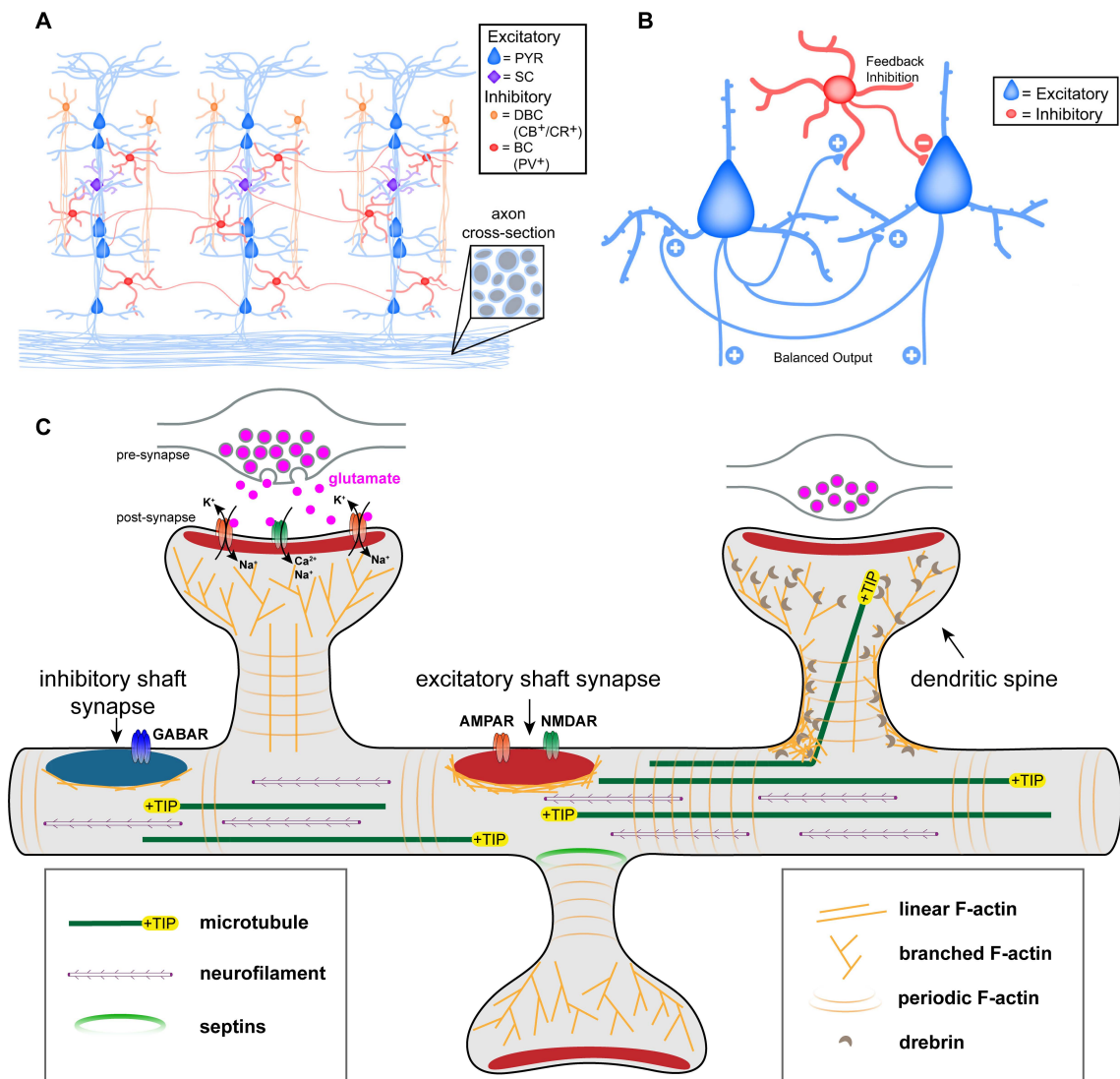
Figure 1: Structural and functional organization of neurons on a network, cellular and sub-cellular level

(A) Typical connectivity of a neocortical circuit containing excitatory cells such as pyramidal (PYR) neurons or stellate cells (SC) as well as inhibitory neurons such as basket cells (BC) or double bouquet cells (DBC). CB^+/CR^+, calbindin- or calretinin-positive; PV^+, parvalbumin-positive; adapted from (Tatti et al., 2017). (B) The output of a neural circuit critically depends on the ratio of excitation and inhibition, which is mediated by the activity of different excitatory and inhibitory neurons and is often altered in various neuropsychiatric diseases; adapted from (Tatti et al., 2017). (C) Schematic illustration of excitatory synaptic transmission elicited by release of the neurotransmitter glutamate from pre-synaptic vesicles in axonal boutons of principle neurons. Binding of glutamate to post-synaptic NMDA and AMPA receptors allows sodium and calcium ions to cross the cell membrane thereby inducing a rapid membrane depolarization. Furthermore, the cytoskeletal architecture of spines and dendrites is shown; adapted from (Bucher et al., 2020).

In the human brain approximately 10^{11} neurons can be classified into several hundred subtypes, which are additionally supported by glial cells giving rise to an enormous cellular complexity (Masland, 2004; Zeng & Sanes, 2017). Neurons represent a morphologically and functionally specialized class of excitable cells and are capable of electro-chemical information transfer by building up a resting membrane potential and utilizing regulated chemical neurotransmitter release. The morphological specialization includes a cell body (soma), from which multifunctional branched structures termed neuronal dendrites as well as a single long axon are extending (Richards & Van Hooser, 2018; Spruston, 2008). While axons provide locations to transmit information by neurotransmitter release, dendrites provide corresponding locations to receive axonal input (Richards & Van Hooser, 2018). Notably, the shape of neuronal somata as well as the structure of dendritic arborizations and the localization and length of axons strongly varies between species, brain regions and neuronal subtypes (Benavides-Piccione et al., 2020; Richards & Van Hooser, 2018). A highly abundant neuronal cell type are pyramidal neurons, which are predominantly found in brain regions associated with higher cognitive functions such as the cerebral cortex, hippocampus or amygdala (Spruston, 2008). These neurons are characterized by a pyramidal or teardrop-shaped soma, from the base of which several downward-directed dendrites emerge, representing the basal dendritic arbor (Benavides-Piccione et al., 2020). Additionally, a prominent apical dendrite emerges from the upper pole of the soma of pyramidal neurons, from which several oblique dendrites spread (Benavides-Piccione et al., 2020). In general, the biophysical and computational properties of neurons to receive, process and transmit information is strongly tied to the morphology and overall architecture of these cells (Richards & Van Hooser, 2018).

1.1.2 Pre-synaptic organization and neurotransmission

Intercellular communication between neurons occurs at specialized contact sites termed synapses. Morphologically, synapses adopt many distinct structures and shapes depending on the neuronal subtype and its localization in the brain (Yuste & Bonhoeffer, 2004). Nonetheless synapses share some common structural features including the synaptic cleft, which represents an approximately 20 - 40 nm wide discontinuity between the communicating cells and separates the synapse in a pre-synaptic and a post-synaptic part. While both hippocampal and cortical pre-synapses appear as axonal

boutons (Figure 1C), detailed morphological knowledge about neocortical pre-synapses is more limited as compared to hippocampal synapses (Rollenhagen & Lübke, 2006; Yuste & Bonhoeffer, 2004).

The high structural and functional diversity of synapses is reflected on a subcellular and molecular level. However, for the same type of synapse, several commonalities can be identified in terms of subcellular and molecular organization and composition. The pre-synapse generally represents a specialized compartment containing synaptic vesicles (SVs) filled with neurotransmitters as well as a dense matrix of cytoskeletal, scaffolding and signaling proteins to localize and organize these SVs (Fejtova & Gundelfinger, 2006). In the axon, directional signal propagation is achieved by an action potential (AP) or spike, which is initiated at the axon initial segment (AIS) by voltage-gated sodium (Na_v) channels if the cellular membrane potential exceeds a certain activation threshold of approximately -50 mV (Bean, 2007; Leterrier, 2018). Upon arrival of the AP at pre-synaptic terminals of the axon, voltage-gated calcium (Ca_v) channels open and allow the influx of Ca^{2+} ions thereby triggering the membrane fusion of SVs and hence the release of neurotransmitter into the synaptic cleft (Figure 1C; Dolphin & Lee, 2020). Among others, multiple different pre-synaptic factors influence synaptic strength including the number of neurotransmitter release sites (active zones), the number and type of participating Ca^{2+} channels or the size of SVs (Atwood & Karunanithi, 2002). Subsequently, information transfer occurs when the neurotransmitter diffuses through the synaptic cleft and binds to corresponding post-synaptic receptors. Neurotransmitters thus represent a synaptic communication unit and are able to modulate the post-synaptic resting membrane potential (-60 to -70 mV) in both directions, thereby producing either excitatory depolarizing or inhibitory hyperpolarizing responses. The type of neurotransmitter released from vesicles within the axon may therefore be used as a distinctive feature between neuronal subtypes based on the signal which is transmitted. While glutamate serves as major excitatory neurotransmitter in the brain, gamma-aminobutyric acid (GABA) acts as an inhibitory transmitter. However, also other morphological, physiological or molecular characteristics are applicable to distinguish between neuronal subtypes (Zeng & Sanes, 2017).

1.1.3 Post-synaptic organization and signal processing

For excitatory synapses the post-synaptic compartment typically forms characteristic membrane protrusions known as dendritic spines. Within dendritic spines a dense submembranous structure known as the post-synaptic density (PSD) serves as organizational unit and also consists of various cytoskeletal, scaffolding and signaling molecules (Chen et al., 2008; Sheng & Kim, 2011; Ziff, 1997). PSDs tend to exhibit a disc-like shape with a mean diameter of 300 - 400 nm and a mean thickness of approximately 30 - 60 nm but are generally highly heterogenous and correlate with the size of the dendritic spine (Sheng & Kim, 2011; X. Yang & Specht, 2019). It has been reported that the PSD can be divided into two main regions, which differ in their size and molecular composition - the core layer and the pallial layer (Dosemeci et al., 2016). The core layer is enriched in proteins of the membrane-associated guanylate kinase (MAGUK) family such as PSD-95 and in guanylate kinase-associated proteins (GKAPs) and forms a dense matrix of protein filaments creating a stable platform for both glutamate receptors in the post-synaptic membrane as well as components of deeper PSD layers (Dosemeci et al., 2016). On the other hand, the pallial layer of the PSD

extends the core layer and contains several additional scaffolding proteins of the SHANK/ProSAP family and the homer family as well as signaling proteins such as the Synaptic Ras GTPase-activating protein (SynGAP) or Calcium/calmodulin-dependent protein kinase II (CaMKII). Besides the PSD, filamentous actin (F-actin) represents the major component to establish the spine architecture and can undergo rapid and dynamic rearrangement to couple synaptic activity to structural adaptation of dendritic spines (Bucher et al., 2020). This coupling is largely mediated by direct and indirect interactions of scaffolding and signaling proteins with the post-synaptic F-actin cytoskeleton (Bucher et al., 2020; Mikhaylova et al., 2018; Salomaa et al., 2021).

Upon release of glutamate from excitatory pre-synaptic terminals, binding to PSD-anchored ionotropic glutamate receptors (iGluRs) as well as metabotropic glutamate receptors (mGluRs) occurs. The iGluR family comprises three different major classes of receptors: 2-amino- 3-(3-hydroxy-5-methyl-isoxazol-4-yl) propanoic acid (AMPA), N-methyl-D-aspartate (NMDA) and kainate receptors (Traynelis et al., 2010). These glutamate receptors represent multi-subunit transmembrane proteins, which are ligand-gated ion channels and allow the selective influx of Na^+ and Ca^{2+} ions into the post-synapse as well as the efflux of potassium ions after binding to glutamate (Fig. 1C; Traynelis et al., 2010; Voglis & Tavernarakis, 2006). More precisely, the immediate response to pre-synaptic glutamate release is mediated by AMPA receptors (AMPARs), which open and conduct Na^+ ions leading to a rapid depolarization of the post-synaptic membrane. NMDA receptors (NMDARs) in contrast are additionally voltage-sensitive and require the removal of an internal Mg^{2+} block to be activated. If the initial AMPAR-mediated depolarization exceeds a certain threshold, also NMDARs open and allow the additional influx of Ca^{2+} ions. Finally, the rise of the post-synaptic Ca^{2+} concentration converts the AP into a biochemical downstream signal. Overall, the complex organization of pre- and post-synaptic compartments allows optimal intercellular signal propagation and integration and facilitates sophisticated information processing by synaptic transmission

1.1.4 Synaptic plasticity

The frequency and amplitude of the post-synaptic Ca^{2+} influx determines the precise molecular reaction pathways downstream to facilitate an individual biochemical interpretation of the pre-synaptic stimulus (Kennedy, 2016). It has been demonstrated extensively that neurons in general and synapses in particular adapt to their input, which is commonly referred to as synaptic plasticity (Voglis & Tavernarakis, 2006). Several different adaptive mechanisms have been shown to either potentiate (long-term potentiation, LTP) or depress (long-term depression, LTD) synaptic transmission depending on the neuronal stimulation (Kotaleski & Blackwell, 2010). While repeated depolarization at a frequency of approximately 10 - 100 Hertz (Hz) with large Ca^{2+} influx amplitude is necessary to induce LTP in the corresponding synapses, low frequency (1 - 5 Hz) stimulation with low Ca^{2+} amplitudes elicits LTD (Kennedy, 2016). Functionally, these principles have been generally implicated as fundamental basis for learning and memory formation in the hippocampus and cortex (Kennedy, 2016). Importantly, however, many different pre- and post-synaptic forms and mechanisms of synaptic plasticity have been described and span a timeframe from milliseconds to minutes, hours, days and even longer and vary between brain regions and cell types (Citri & Malenka, 2008). Consequently, also short-term plasticity has been described to play an

important role for short-lasting forms of memory or adaptations to sensory inputs. Furthermore, additional mechanisms such as metaplasticity or synaptic scaling exist to balance and stabilize these forms of LTP and LTD to prevent the formation of epileptogenic excitation or complete quiescence in neural circuits (Citri & Malenka, 2008).

The multitude of synaptic plasticity mechanisms requires a complex network of underlying signaling pathways which reflect and integrate the structural and functional changes associated with potentiated or depressed synaptic transmission. Especially Ca^{2+} sensing proteins are, among others, crucially involved in translating excitatory ion fluxes into specific short-term and long-term molecular rearrangements of potentiated synapses (Higley & Sabatini, 2012; Sheng & Kim, 2011, 2002). One of the most prominent post-synaptic Ca^{2+} sensing proteins in glutamatergic synapses is calmodulin (CaM), which undergoes a conformational change after Ca^{2+} binding resulting in a stimulated protein:protein interaction (PPI) with CaMKII. Following activation of CaMKII by Ca^{2+}- and CaM-binding, phosphorylation of specific AMPAR subunits occurs leading to an increased insertion of AMPARs into the post-synaptic membrane and thus to increased EPSCs after subsequent synaptic activation (Voglis & Tavernarakis, 2006). In the hippocampus, CaM in parallel also activates the adenylyl cyclase (AC) types 1 and 8, which produce the second messenger cyclic AMP (cAMP) and thus lead to an activation of protein kinase A (PKA). Since PKA is involved in the phosphorylation of AMPAR GluA1 subunits, it directly modifies the opening probability of AMPARs (Kotaleski & Blackwell, 2010). Simultaneously, high Ca^{2+} influx triggers multiple remodeling processes of the PSD and post-synaptic actin cytoskeleton, which becomes larger and more branched giving rise to an overall enlarged spine head (Kennedy, 2016). Overall, several different and partially overlapping or parallel signaling pathways result in morphological and functional changes to establish LTP. However, the maintenance of these changes over a longer time period depends on local protein synthesis and *de novo* transcription to provide the potentiated synapse with sufficient proteins (Citri & Malenka, 2008).

While LTP is primarily associated with the activation of kinase signaling cascades, LTD is thought to predominantly involve the activation of phosphatase cascades including the Ca^{2+}/CaM - dependent phosphatase calcineurin (Citri & Malenka, 2008). This suggests that in both scenarios similar processes might be responsible for the modulation of synaptic transmission. Consequently, NMDAR-dependent LTD is mediated by dephosphorylation of protein kinase C (PKC) and PKA substrates such as the AMPAR subunit GluA1 resulting in a decreased opening probability of AMPARs. Furthermore, a loss of synaptic AMPARs by dissociation from their scaffolds within the PSD followed by clathrin- and dynamin-dependent endocytosis has been shown during LTD, which represents the counterpart to an increased synaptic AMPAR insertion during LTP (Citri & Malenka, 2008). Apart from this, also other forms such as mGluR-dependent LTD or endocannabinoid-mediated LTD have been described. Taken together, it is now established that memories and experiences are encoded in neural circuits by a regulated distribution of synaptic weights, which is realized by various distinct mechanisms of synaptic plasticity (Citri & Malenka, 2008; Kennedy, 2016; Kotaleski & Blackwell, 2010).

1.2 Autism-spectrum disorder (ASD) as synaptic disease

ASD is currently thought to affect approximately 1% of the human population and is characterized by a broad spectrum of behavioral and cognitive conditions of varying severity including impairments in communication and reciprocal social interaction as well as restricted, repetitive behaviors and interests (Fakhoury, 2015; Lord et al., 2020). Patients diagnosed with ASD often present comorbidities such as intellectual disability (ID) or seizure disorders suggesting a high genetic contribution and heritability of ASD (Lord et al., 2020). Indeed, ASD is described as pervasive and heterogenous neurodevelopmental disorder with more than 100 genes or genomic loci associated with autism (Lord et al., 2020). Consequently, many theories have been proposed to explain the pathophysiology of ASD on various levels ranging from alterations in the early postnatal brain volume to local patterns of neuronal hypo- or hyperconnectivity and a disbalance of the excitation/inhibition (E/I) ratio up to dysregulated synaptic signaling pathways (Fakhoury, 2015).

Many of these ASD-associated genetic risk loci represent protein coding regions relevant for synaptic structure and function (Figure 2; Guang et al., 2018; Zoghbi & Bear, 2012). Therefore, ASD and the associated ID may be seen as a disorder of synapse structure and function, termed a "synaptopathy". Furthermore, the physiological role of synaptic proteins, which have been found to be mutated in ASD patients or which have been associated with the pathogenesis of ASD allow a more precise investigation of individual synaptic signaling pathways relevant for ASD. It has been conservatively estimated that approximately 10 - 20% of autistic patients carry a rare *de novo* point mutation or copy number variation (CNV) resulting in thousands of different highly penetrant mutations, which have been identified (Abrahams & Geschwind, 2008; Lord et al., 2020; Zoghbi & Bear, 2012). Although defined individual rare variants only account for a small fraction of ASD cases, their contribution to understanding the disease etiology is expected to be very high as the observed functional effect is almost always due to the variant itself (Iossifov et al., 2014). On the other hand 80 - 90% of ASD cases remain without an identified causal factor (idiopathic ASD) and are expected to result from interactions of multiple common variants with low individual penetrance and functional relevance from which an understanding of the disease etiology can hardly be obtained (Abrahams & Geschwind, 2008; Bodmer & Bonilla, 2008). Overall, this gives rise to an enormous underlying complexity and individuality of disease-related molecular perturbations.

Consequently, most of the currently available knowledge of ASD-associated synaptic pathways or molecular processes has been obtained from investigating the impact of highly penetrant rare variants (i.e. mostly missense mutants) of synaptic proteins (Figure 2). Most synaptic proteins for which ASD-associated missense variants have been identified and studied may be grouped into three different categories: cell-adhesion molecules (CAMs) such as neurexins (NRXNs) and neuroligins (NLGNs), signaling molecules like SynGAP or CaMKII and scaffolding proteins including SHANK3 or PSD-95 (Betancur et al., 2009; Guang et al., 2018; Santini & Klann, 2014; Soler et al., 2018).

1.2.1 ASD-associated cell-adhesion molecules

CAMs are crucially involved in the establishment of pre- and post-synaptic contacts and provide anchors for scaffolding proteins, which in turn stabilize neurotransmitter

receptors and assemble a plethora of different signaling molecules (Betancur et al., 2009). One of the best studied ASD-associated CAMs are NLGNs, for which different rare variants and CNVs especially for *Nlgn3* and *Nlgn4x* have been associated with both syndromic and nonsyndromic autism (Betancur et al., 2009; Singh & Eroglu, 2013). NLGNs represent post-synaptic transmembrane proteins and interact with pre-synaptic NRXNs, thereby forming trans-synaptic adhesions. These NLGN-NRXN pairs have been related to the regulation of excitatory and inhibitory synapse function and maturation (Varoqueaux et al., 2006). Importantly, it has been pointed out that the elimination of NLGNs in *Nlgn1-Nlgn2-Nlgn3* triple-knockout mice does not lead to reduced synapse numbers but rather affects the recruitment of neurotransmitter receptors to excitatory and inhibitory synapses (Varoqueaux et al., 2006). In line with this it was shown that overexpression of NLGN1 selectively potentiates excitatory synaptic responses, while overexpression of NLGN2 potentiates exclusively inhibitory synaptic responses (Chubykin et al., 2007). Hence, NLGNs specify the functional development of synapses and act as activity-dependent molecular instructors by regulating whether a synapse may become excitatory or inhibitory as well as facilitating or depressing (Chubykin et al., 2007). Furthermore, NLGNs exert a synaptic validation function by determining whether a given synapse will be stable or transient but are not required for the initial formation of synapses (Chubykin et al., 2007). Overall, NLGNs are necessary for the development of use-dependent neuronal circuits as well as for the determination and maintenance of the E/I ratio within these circuits (Betancur et al., 2009; Chubykin et al., 2007). This highlights the importance of activity-dependent regulation of synaptic connectivity in the pathogenesis of ASD.

1.2.2   ASD-associated synaptic signaling molecules

Besides the pathogenic potential of CAM-mediated alterations of the E/I ratio and activity-dependent development of neural circuits, ASD may also arise from dysregulated synaptic signal integration and transduction by mutations found in crucial synaptic signaling molecules. Among others, a rare missense mutation of CaMKII, which directly senses and integrates NMDAR-mediated post-synaptic Ca^{2+} influx, has been found in an autistic patient (Stephenson et al., 2017). This mutation was described to disrupt the catalytic activity of CaMKII and to result in reduced interactions with crucial post-synaptic binding partners such as SHANK3. Furthermore, the mutation disrupts synaptic targeting of CaMKII and results in a reduced dendritic spine density and AMPAR-mediated synaptic transmission (Stephenson et al., 2017). Due to the central role of CaMKII in regulating synaptic structure and function, it is conceivable that individual interaction partners or regulated proteins of CaMKII might also be associated with ASD. This is the case for SynGAP, which preferentially localizes to the PSD by binding to PSD-95/DLG/ZO-1 (PDZ) domain "slots" of PSD-95 and gets phosphorylated by CaMKII after synaptic activation (Walkup et al., 2016; Yang et al., 2013). This phosphorylation event has been shown to strongly decrease the affinity of SynGAP for these PDZ domains and to result in a rapid dispersion of SynGAP out of the spine head thereby triggering downstream signaling cascades involving Ras and Rac1, which stimulates spine enlargement and increased AMPAR insertion into the post-synaptic membrane to facilitate LTP (Araki et al., 2015; Walkup et al., 2016; Yang et al., 2013). In a mouse model of *Syngap1* haploinsufficiency-induced ID most of the observed cognitive defects could be attributed to an altered function of glutamatergic pyramidal neurons in the

forebrain (Ozkan et al., 2014). Here, an increased excitatory synaptic strength and thus altered E/I balance as well as abnormal cortical discharges were observed as a result of the developmental impact of the SynGAP loss-of-function mutation (Ozkan et al., 2014). This was interpreted as an early synapse maturation effect, which leads to increased dendritic spine volumes during development thereby compromising the ability of synaptic downscaling in response to the cortical hyperexcitability (Ozkan et al., 2014). In line with this, rare missense and truncating mutations in the human *SYNGAP1* gene have been found to cause ID, autism and a special form of epilepsy in various patients (Berryer et al., 2013; Jimenez-Gomez et al., 2019). This highlights that rare variants occurring in signaling molecules may have profound and very distinct effects on multiple levels and pathways (Fig. 2).

1.2.3 ASD-associated scaffolding proteins

To facilitate and regulate the function of such post-synaptic signaling molecules including CaMKII and SynGAP, interactions with various scaffolding proteins of the PSD are necessary. Post-synaptic scaffolding proteins are generally considered as master organizers of the PSD and are crucial for synaptic structure and function (Verpelli et al., 2012). They are involved in clustering and trafficking of glutamate receptors at the post-synaptic membrane, actively regulate signaling events and provide molecular links between synaptic activity and the reorganization of the actin cytoskeleton (Verpelli et al., 2012). Furthermore, it has been shown that scaffolding proteins act as regulators of neurite outgrowth and dendrite development in immature neurons likely by serving as adaptor molecules or targeting elements for cytoskeleton regulating proteins (Vessey & Karra, 2007). Many synaptic scaffolding proteins represent multi-domain proteins which are differently enriched in PDZ domains (Kim & Sheng, 2004). These PDZ domains facilitate specific PPIs between the scaffolds and other synaptic protein targets and may be arranged as tandem-PDZ supramodules, which additionally enhance binding specificity and affinity to individual targets in a synergistic manner (Feng & Zhang, 2009). One of the most prominent scaffolds is the postsynaptic density protein 95 (PSD-95), which is also known as SAP90 and is coded by the *DLG4* gene. PSD-95 is highly abundant in the PSD and contains three PDZ domains, which among others bind to GluN2A and GluN2B subunits of the NMDAR, to the $K_v1.4$ K^+ ion channel or to NLGNs (Kim & Sheng, 2004). Besides the PSD-95/MAGUK family, other PSD scaffolds include the homer family consisting of homer1-3 with several isoforms each, the SH3 and multiple ankyrin repeat domains (SHANK) family including the proteins SHANK1-3 with all of their isoforms as well as the GKAP family (also known as PSD-95/SAP90-associated proteins or SAPAPs; Ting et al., 2012).

Due to their central role for synapse structure, function and development, post-synaptic scaffolding proteins have been strongly associated with the development of ASD (Monteiro & Feng, 2017; Sala et al., 2015; Ting et al., 2012; Xing et al., 2016). Interestingly, these scaffolding proteins are often associated with syndromic autism, which is accompanied with other neurological and neurodevelopmental disorders. From the PSD-95 family, the *DLG1* gene (which is coding for the SAP97 protein) has been associated with the 3q29 microdeletion syndrome characterized by mental retardation, dysmorphic facial features, ataxia and autism (Willatt et al., 2005). On the other hand, the *SHANK* gene family has been associated with Phelan-McDermid syndrome (PMS), primarily caused by 22q13 deletion, which comprises absent or severely delayed speech,

neonatal hypotonia, facial dysmorphism and partially also ASD, ID and the presence of seizures, which will be described in more detail in the following chapter (Guilmatre et al., 2014).
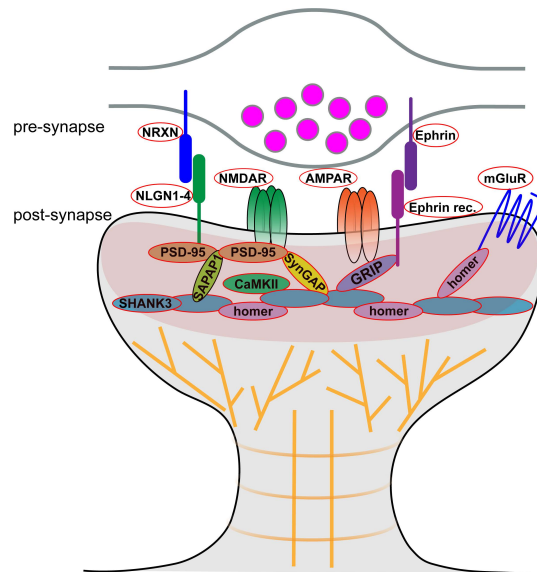
Figure 2: Synaptic proteins commonly associated with ASD
The scheme depicts a selection of post-synaptic scaffolding and signaling proteins as well as trans-synaptic adhesion molecules commonly associated with ASD (red circles). Many scaffolding proteins such as SHANK3, PSD-95 or homer directly or indirectly bind to and anchor glutamate receptors to the PSD and thus crucially contribute to the regulation of synaptic transmission and plasticity. Signaling molecules such as CaMKII or SynGAP integrate post-synaptic Ca^{2+} spikes and activate corresponding downstream pathways such as the reorganization of the synaptic actin cytoskeleton. Trans-synaptic adhesion molecules such as neurexins and neuroligins regulate synaptic connectivity by connecting pre- and post-synaptic compartments and facilitate trans-synaptic signaling processes.

1.3 SHANK-protein associated synaptic diseases: Shankopathies

One of the best studied excitatory synaptic scaffolds is the *SHANK* gene family, which has been implicated in the pathogenesis of various neurodevelopmental and psychiatric disorders including ASD, schizophrenia or ID (Gauthier et al., 2010; Monteiro & Feng, 2017). SHANK proteins are encoded by the *Shank1*, *Shank2* and *Shank3* genes, which show a brain region specific expression pattern in the mouse brain (Figure 3A; Monteiro & Feng, 2017). In general, however, the expression of SHANKs is not restricted to the central nervous system (CNS) and the *Shank3* gene has been shown to be ubiquitously expressed throughout a plethora of different human tissues (Lilja et al., 2017). Each of the *Shank* genes harbors multiple intragenic promoters and alternative splicing sites giving rise to a substantial number of transcripts and protein isoforms (Monteiro & Feng, 2017). Particularly the expression of SHANK3 isoforms has been demonstrated to be cell-type specific and developmentally regulated and further depends on neuronal activity and epigenetic modifications (Wang et al., 2014). In glutamatergic synapses, SHANK3 represents an integral part of the pallial layer of the PSD, where it is organized in subsynaptic nanodomains or clusters (Figure 3B; MacGillavry et al., 2013). The canonical SHANK3a isoform consists of five different domains plus a proline-rich stretch, which includes the binding sites for homer1 and cortactin among others.

The domains comprise a SHANK/ProSAP N-terminal (SPN) domain, an ankyrin repeat region (ARR), a Src homology 3 (SH3) domain followed by a PDZ domain and a C-terminal sterile alpha motif (SAM; Monteiro & Feng, 2017). The SPN domain interacts, among others, with signaling proteins relevant for the regulation of F-actin structure and dynamics such as R-Ras, H-Ras or Rap1, all belonging to the Ras superfamily of small GTPases (Cai et al., 2020; Lilja et al., 2017). This interaction was shown to inhibit integrin activation by sequestration of active Rap1 and R-Ras (Lilja et al., 2017). The ARR domain interacts with cytoskeletal proteins such as α-fodrin, the cell adhesion protein δ-catenin or sharpin, a component of the linear ubiquitin chain assembly complex (LUBAC; Böckers et al., 2001; Hassani Nia et al., 2020; Lim et al., 2001). Both the SH3 and PDZ domain of SHANK3 have been shown to associate with the C-terminal region of the voltage-gated L-type Ca^{2+} channel $Ca_v1.3$, an interaction which is necessary and sufficient for synaptic clustering of $Ca_v1.3$ (Zhang et al., 2005). For the PDZ domain, additional binding partners such as SAPAP1 and the GluA1 subunit of AMPARs have been described (Boeckers et al., 1999; Uchino et al., 2006). The proline-rich stretch located between the PDZ- and the SAM-domain, which contains the binding sites for homer1 and cortactin, serves as important link to the spinous F-actin cytoskeleton and to other scaffolds of the PSD (Macgillavry et al., 2016; Naisbitt et al., 1999; Tu et al., 1999). Ultimately, the C-terminal SAM domain is necessary to establish the localization of SHANK3 to dendritic spines as well as to promote activity-dependent oligomerization within the PSD (Baron et al., 2006; Boeckers et al., 2005). Taken together, SHANK3 acts as a linking element between ionotropic and metabotropic glutamate receptors at the post-synaptic membrane and downstream cytoskeletal elements and therefore occupies a central role for the regulation of synaptic structure and function.
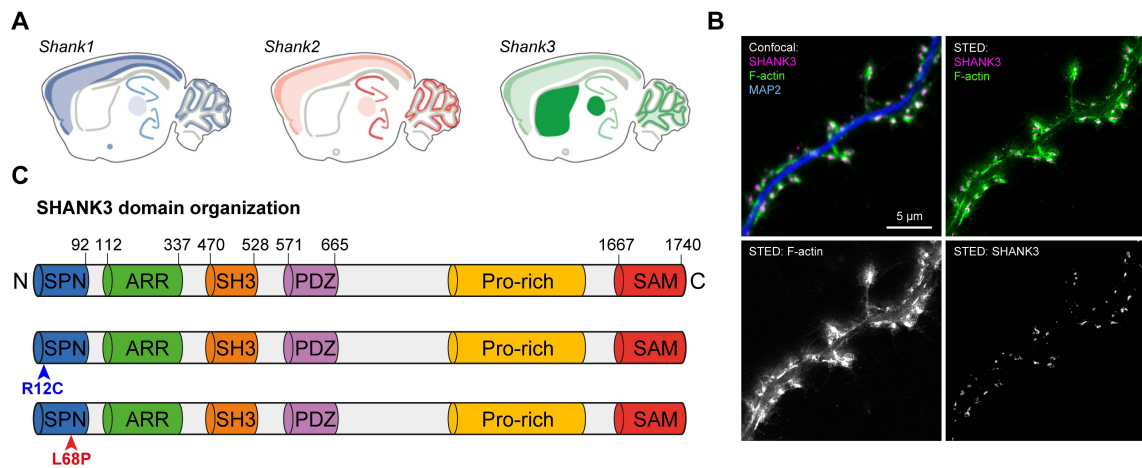
Figure 3: Expression, subcellular localization, and domain organization of SHANK3 in the brain

(A) *Shank* genes show brain-region specific expression patterns in the mouse brain. Only *Shank3* is highly enriched in corticostriatal regions, which have been shown to be involved in ASD. All three SHANKs are present in the cortex and hippocampus, which are associated with learning and memory formation; adapted from (Monteiro & Feng, 2017). (B) In primary mouse hippocampal neurons (DIV16), SHANK3 is localized both in the dendritic shaft and in spines. Within individual dendritic spines, SHANK3 forms nanoclusters of different size and number, as shown by stimulated emission depletion (STED) microscopy. *Images were generated by Marina Mikhaylova*. (C) SHANK3 is a large multidomain protein comprising five folded domains and an additional proline-rich region each indicated in different colors. It interacts with various synaptic proteins including glutamate receptors, cytoskeleton-associated proteins, CAMs or signaling proteins and thus serves as molecular organizer and "master" scaffold in the PSD. Several SHANK3 protein variants resulting from alternative splicing or promotor usage have been discussed and partially investigated and represent truncated versions of the full-length (FL) protein harboring a reduced set of domains. The exact number and domain structure of these isoforms, however, is not fully known. The ASD-associated missense mutations R12C and L68P are located in the SPN domain.

Due to the localization and function of SHANK proteins in excitatory synapses, mutations within the *Shank* gene family are expected to cause a variety of neurodevelopmental and neuropsychiatric disorders, collectively termed shankopathies (Sala et al., 2015). Thereby, molecular defects within the *Shank3* gene are best characterized and have the highest clinical relevance (Leblond et al., 2014). These molecular defects include deletions and duplications of variable size either within or in close proximity to the *Shank3* gene as well as disruptive translocations or individual sequence changes such as missense, frame shift or splice site mutations (Jiang & Ehlers, 2013). Most of these pathogenic variants were reported to result in *Shank3* haploinsufficiency, which is thought to be causative for the development of PMS (Leblond et al., 2014). The phenotypical presentation of *Shank3* variants, however, is variable and patients show a wide spectrum of mild to severe cognitive and neurological symptoms which may go beyond PMS and include the development of generalized epilepsy or schizophrenia, among others (Gauthier et al., 2010; Jiang & Ehlers, 2013; Leblond et al., 2014).

While the relevance of proper *Shank3* gene dosage for normal brain function has been extensively shown with deletions or duplications leading to neuropsychiatric disorders involving ASD and ID, the functional impact of more subtle missense mutations is less

clear (Durand et al., 2007; Han et al., 2013). Due to the fact that the pathogenicity of SHANK3 missense mutations might go beyond altering SHANK3 protein levels in excitatory synapses, structural analyses of mutant SHANK3 proteins are required to understand the origin and molecular impact of such missense mutations (Hassani Nia & Kreienkamp, 2018). Recently, the structure of an N-terminal SHANK3 fragment comprising the residues 2 - 347 (PDB: 5G4X) including the SPN and ARR domains has been solved and provided insights into the potential role of missense mutations located in this region (Lilja et al., 2017). A plethora of different missense mutations covering most regions of the SHANK3 protein have been identified in autistic patients (De Rubeis et al., 2018; Leblond et al., 2014). Among others, these include the R12C, L68P or Q321R mutation, which are located within this previously crystallized N-terminal SHANK3 fragment (Hassani Nia & Kreienkamp, 2018). The latter represents a *de novo* mutation found in a female ASD patient displaying social and language deficits with limited reciprocal conversation, social withdrawal, verbal repetitive behaviors as well as severe inattention and irritability (Moessner et al., 2007). The patient further shows narrow interests and mild self-injurious behaviors including biting and hair pulling but no motor stereotypes and exhibits abnormal EEG patterns with bilateral epileptiform discharges without seizures and suffers from severe sleep disorder (Moessner et al., 2007). On a molecular level, overexpression of Q321R mutant SHANK3 in primary hippocampal neurons has been demonstrated to result in a significant reduction of F-actin levels in dendritic spines compared to overexpressed WT SHANK3 (Durand et al., 2012). This suggests that the Q321R mutation interferes with the ability of SHANK3 to regulate F-actin levels in dendritic spines resulting in an alteration of spine structure and function (Durand et al., 2012). Furthermore, Q321R mutant SHANK3 displays enhanced interaction with the ARR domain ligand sharpin (Mameza et al., 2013). Recently, the first *Shank3* missense mutation knock-in (KI) mouse line carrying the Q321R variant has been created and characterized extensively (Yoo et al., 2019). Thereby $Shank3^{Q321R/Q321R}$ mice were shown to exhibit reduced excitability of hippocampal CA1 pyramidal neurons as well as higher resistance to pentetrazole (PTZ)-induced seizures, corroborating the role of SHANK3 in the regulation of synaptic transmission (Yoo et al., 2019).

While the Q321R mutation is located within the ARR domain of SHANK3, both the R12C and L68P mutation are found in the SPN domain, which was shown to interact intramolecularly with the ARR domain (Lilja et al., 2017). While the R12C mutation represents a charge-neutralizing substitution located in the β1-strand of the SPN domain, the L68P mutation affects the hydrophobic core of this domain (Lilja et al., 2017). The R12C mutation was originally identified in a male ASD patient and was transmitted from the mother who has social phobia traits (Durand et al., 2007). This amino acid substitution is also present in an unaffected brother and is thus not considered as sole cause of ASD. The patient displays high pain threshold and low noise threshold as well as complete absence of language and severe mental retardation (Durand et al., 2007). On the other hand, the L68P mutation was found to exhibit higher penetrance compared to the R12C mutation and was not found in any healthy control (Gauthier et al., 2009). The L68P variant was found in a female ASD patient, who inherited the mutation from an epileptic father and displays developmental delay and absent speech (Gauthier et al., 2009). On a cellular and molecular level, however, these mutations remain much less investigated. It was shown by isothermal titration calorimetry (ITC), however, that the R12C mutation reduces the binding affinity of the SPN domain to Rap1 approximately by a factor of 11 and effectively abolishes binding to H-Ras, Rap1a and Rap1b in

pulldown assays (Lilja et al., 2017). This is explained by the involvement of the R12 residue of the SPN domain in the formation of an ion pair with E37 of Ras, which can no longer be formed upon R12C substitution. While the L68P mutation showed a similarly disruptive behavior on the interaction with H-Ras, Rap1a and Rap1b, this mutation was predicted to primarily affect the structure of the SPN domain itself as well as its interaction with the ARR domain (Lilja et al., 2017). The latter was discussed as potential cause for the increased interaction of L68P mutant SHANK3 with the ARR domain ligand sharpin (Mameza et al., 2013). Notably, a very recent study demonstrated that SHANK3 can bind actin directly via the SPN domain, which is regulated by a conformational switch of the SPN and ARR domain (Salomaa et al., 2021). Thereby the interaction of the SPN domain with the ARR domain represents an autoinhibited "closed" state of SHANK3 which prevents binding to actin (Salomaa et al., 2021). On a cellular level, overexpression of R12C mutant SHANK3 in primary hippocampal neurons was demonstrated to result in a less pronounced increase in miniature excitatory post-synaptic currents (mEPSCs) compared to neurons overexpressing WT SHANK3 (Durand et al., 2012). Additionally, the R12C mutation increased F-actin levels and the spine density in hippocampal primary neurons less efficiently than WT SHANK3 upon overexpression, leading to intermediate effects on spine structure and synaptic transmission (Durand et al., 2012). Overall, individual molecular and cellular consequences of these ASD-associated missense mutations have been explored to some detail, but studies providing a link between mutation-induced structural perturbations of SHANK3 and their functional contribution to corresponding synaptic phenotypes are largely missing.

1.4 Biophysical methods for analysis of protein structure, folding and dynamics

To investigate potential mutation-induced structural perturbations, various biophysical methods may be employed. With distinct spatiotemporal resolution, methods such as small-angle X-ray scattering (SAXS), nano differential scanning fluorimetry (nanoDSF), circular dichroism (CD) spectroscopy or molecular dynamics simulations (MDS) provide information on macromolecular structure, folding and dynamics. Consequently, this allows to analyze and characterize the molecular impact of missense mutations as first step to understand disease-relevant molecular breaking points. Therefore, the scopes and limitations of these methods are briefly outlined below.

1.4.1 Small-angle X-ray scattering (SAXS)

SAXS represents a technique to obtain low resolution nanostructural information by detecting X-ray photons, which are elastically scattered by the illuminated sample, similar to crystallographic methods (Blanchet & Svergun, 2013). In contrast to macromolecular crystallography, however, molecules can be kept in solution representing an advantage for sample preparation as individual proteins or other macromolecules may be difficult to crystallize. On the other hand, high rotational and translational degrees of freedom in solution limit the accessible spatial information and therefore the structural resolution to a range of approximately 300 - 0.5 nm (Blanchet et al., 2015; Blanchet & Svergun, 2013). Despite limited resolution, SAXS can provide structural information of highly flexible and polydisperse systems, which is not achievable with other methods (Tuukkanen et al.,

2017). Since biological macromolecules exhibit a low scattering contrast, the intensity of the incident X-ray beam has to be very high using instruments optimized for the lowest possible background (Blanchet & Svergun, 2013). Therefore, SAXS data is ideally acquired at high-brilliance synchrotron beamlines providing a high photon flux and small beam size for best data quality (Blanchet et al., 2015). In practice the isotropic scattering pattern of the sample and the solvent are detected separately on a 2D X-ray detector. The 1D scattering profile (i.e. scattered intensity as function of scattering vector) is subsequently obtained by radially averaging the scattering images. After subtraction of the solvent scattering from the sample scattering profile, a background-corrected intensity I(s) is obtained, which can be used to directly determine several (structural) parameters such as the radius of gyration (R_g), maximum particle diameter (D_{max}) or molecular weight (MW) estimates but also for *ab initio* macromolecular shape determination (Blanchet & Svergun, 2013; Tuukkanen et al., 2017). In case limited high-resolution structural information is available (e.g. of individual domains from a large multi-domain protein), SAXS data may be used to reconstruct the corresponding molecular architecture by utilizing different modelling approaches (Manalastas-Cantos et al., 2021). Software packages for visualization, processing, analysis and modelling of SAXS data from biological macromolecules such as ATSAS are freely available (Manalastas-Cantos et al., 2021).

Several synaptic proteins have already been investigated previously using SAXS. This includes the synaptic arrangement of extracellular regions of the NLGN-βNRXN pair, which provides a structural basis for understanding the potential impact of ASD-associated mutations in NLGNs and NRXNs (Comoletti et al., 2007). Additionally, conformational transitions of collybistin (CB), an adaptor protein regulating receptor recruitment to inhibitory GABAergic and glycinergic synapses, have been assessed using SAXS (Soykan et al., 2014).

1.4.2 Nano differential scanning fluorimetry (nanoDSF)

Besides the analysis of protein structure, addressing changes of protein stability provides valuable additional information on the molecular impact of disease-associated missense mutations. Among others, many different spectroscopic techniques such as intrinsic tryptophan fluorescence emission spectroscopy or CD spectroscopy have been employed to address both thermodynamic and kinetic protein stability (Chattopadhyay & Varadarajan, 2019; Greenfield, 2007c, 2007a). Thereby, nanoDSF (Prometheus NT.48, NanoTemper technologies) represents an advanced method to detect changes in intrinsic tyrosine and tryptophan fluorescence emission of protein samples as a function of various conditions such as temperature, time or chemical denaturant (Chattopadhyay & Varadarajan, 2019). Compared to conventional fluorescence spectroscopy utilizing quartz cuvettes, this capillary-based method allows rapid and parallel measurement of up to 48 samples over a broad concentration range (5 µg/ml up to more than 250 mg/ml) and requires a volume of only 10 µl per capillary. Fluorescence excitation is achieved by a focused 280 nm light-emitting diode (LED) and is detected at 330 nm and 350 nm. The sample temperature is controlled by a thermal element (15 - 95 °C) onto which the individual capillaries are placed. Upon thermal ramping, protein aggregation can be simultaneously monitored by measuring the scattering-induced loss of light intensity using inbuilt back-reflection optics. Consequently, the thermodynamic stability of protein samples can be measured by monitoring the fluorescence ratio F(350/330 nm) with

increasing temperature. As tyrosine and tryptophan fluorescence are environmentally sensitive, the fluorescence ratio F(350/330 nm) primarily reports changes in the protein tertiary structure and correspondingly obtained melting temperatures (T_m) may differ from secondary structure melting.

1.4.3 Circular dichroism (CD) spectroscopy

To specifically assess the impact of missense mutations on the secondary structure of proteins, CD spectroscopy is frequently applied, which readily provides information about folding as well as thermal or chemical stability of proteins on a secondary structure level (Greenfield, 2007d, 2007c, 2007b). This has been demonstrated in a study characterizing the β-III-spectrin mutant L253P, which is associated with spinocerebellar ataxia type 5 (SCA5; Avery et al., 2017).

CD spectroscopy is based on the differential absorption of left- and right-circularly polarized light by chiral molecules such as proteins (Kelly et al., 2005). Thereby, secondary structure specific signals are obtained in the far-UV region (190 - 250 nm), where the peptide bond acts as chromophore showing several specific absorption bands with different amplitudes corresponding to individual electronic transitions (Bulheller et al., 2007). Consequently, characteristic reference spectra can be obtained for each structural element. The obtained CD spectrum of a given protein comprising more than one secondary structure element therefore represents a linear combination of characteristic reference spectra (Bulheller et al., 2007). This allows to estimate the fraction of individual secondary structure elements within a protein of interest. Furthermore, individual wavelengths (e.g. 222 nm for α-helices) may be used to study the reaction of a system to different perturbations such as temperature or chemical denaturants to obtain additional information on the stability of proteins (Kelly et al., 2005). CD spectroscopy is also suitable to study the tertiary structure of proteins by acquiring spectra in the near-UV range (260 - 320 nm), where aromatic amino acid residues exhibit characteristic absorption profiles. Despite recent progress in the theoretical treatment of near-UV CD spectra considering the vibrational structure of electronic transitions, obtaining significant structural insights from such spectra remains challenging (Kelly et al., 2005; Li & Hirst, 2017). Overall, CD spectroscopy provides insight into protein folding, stability and secondary structure content, which is complementary to other spectroscopic and scattering techniques. Collectively, however, very limited information about protein conformational dynamics can be captured from these methods.

1.4.4 Molecular dynamics (MD) simulations

To experimentally study conformational dynamics of proteins with high temporal resolution is challenging. Therefore, MDS offer a possibility to investigate the movement of a protein or other molecular system with pico- to femtosecond temporal resolution (Hollingsworth & Dror, 2018). This allows to capture various processes including conformational changes, biomolecular interactions or protein folding and unfolding and to understand the reaction of biomolecules to perturbations such as mutation, posttranslational modifications, ligand binding or changes in pH (Hollingsworth & Dror, 2018). To study the dynamic behavior of a biomolecule in solution with MDS, structural information has to be present as a prerequisite. Such information may be obtained either

experimentally from X-ray crystallography, cryo-electron microscopy (cryo-EM) or nuclear magnetic resonance (NMR) spectroscopy or theoretically by homology modelling. In general, software packages for molecular dynamics simulations such as GROMACS, NAMD, CHARMM or AMBER perform similar computations but differ slightly in their compatibility with different hardware or in individual features (Hollingsworth & Dror, 2018; Pronk et al., 2013). All of these software packages support multiple different force fields with individual strengths and weaknesses depending on the studied system. Before setting up an MDS, a force field has to be chosen and a molecular topology has to be provided, which contains specifications of the molecule and the system (e.g. protein in water) to be simulated as well as force field parameters and optional entries related to position restraints or intermolecular interactions. Subsequently, in atomistic MDS the forces acting on each atom are computed repeatedly by numerically solving Newton's equations of motion and updating the positions and velocities of each atom (Hollingsworth & Dror, 2018). As a result, a trajectory is obtained which describes how the simulated system evolves over time with high spatiotemporal resolution. However, accessible timescales with atomistic MDS are limited due to high computational demand and several processes such as protein folding and unfolding can hardly be captured with such an approach. Therefore, coarse-grained MDS are applicable, where one particle or bead represents a group of atoms thereby reducing both the computational demand and resolution and extending accessible timescales (Hollingsworth & Dror, 2018). Nonetheless, classical MDS and force fields represent approximations rather than exact calculations and processes such as formation or breakage of covalent bonds cannot be described classically. Overall, taking into account the scope and limitations, MDS may complement experimental data and provide insights into many different biomolecular processes which are inaccessible by other methods (Hollingsworth & Dror, 2018). In general, such a multidisciplinary approach was used previously to gain molecular insights into protein structure, folding and dynamics but is largely missing for synaptic proteins.

Aims of the thesis

The focus of this thesis is to decipher the molecular and cellular impact of missense mutations affecting a crucial synaptic scaffolding protein, SHANK3. Many identified missense mutations within the *Shank3* gene have been associated with numerous neuropsychiatric and neurodevelopmental conditions including ASD, schizophrenia or epilepsy. In my work I focus on the structural and functional perturbations elicited by two specific amino acid changes, R12C and L68P, which have been previously identified in autistic patients, with the goal to contribute to a better understanding of underlying molecular processes for SHANK3-mediated ASD. Specifically, I aim

1. to explain the impact of these mutations on the structure, folding and dynamics of SHANK3 as initial breaking point for further downstream processes;
2. to understand the functional relevance of these mutations for biochemical signal integration and transmission and to obtain further insight into resulting morphological and functional alterations on a cellular level.
3. to investigate the cellular and network impact of the L68P mutation in a humanized mouse model of ASD.

2 Results

2.1 Investigating the impact of the R12C and L68P mutation on the structure, folding and dynamics of SHANK3

The data presented in the following has been published in (Bucher et al., 2021). SAXS measurements at the P12 beamline were performed with the help of Dmitry Molodenskiy (EMBL Hamburg). Molecular dynamics simulations were set up with the help of Stephan Niebling (EMBL Hamburg). Rajeev Raman (LIN Magdeburg) helped with fluorescence spectroscopy measurements.

Autism spectrum disorders (ASDs) have been increasingly recognized as neurodevelopmental synaptic diseases with widespread etiology (Guang et al., 2018; Lord et al., 2020; Zoghbi & Bear, 2012). Several ASD-related phenotypes have been studied in different animal models including alterations in the excitation/inhibition balance and circuit homeostasis, neuronal morphology or synaptic dysfunction (Durand et al., 2012; Gogolla et al., 2009; Nelson & Valakh, 2015; Zoghbi & Bear, 2012). However, no clear link between ASD-associated synaptic phenotypes and fundamental changes in the structure and dynamics of affected proteins has been established yet. As missense mutations in the post-synaptic scaffolding protein SHANK3 have been strongly associated with the development of ASD (Hassani Nia & Kreienkamp, 2018; Jiang & Ehlers, 2013), the following chapter aims to provide insight into the impact of two selected mutations, R12C and L68P, on the structure and dynamics of SHANK3. These mutation-induced alterations are described as initial breaking point for higher-order molecular and cellular consequences, which will be addressed in subsequent chapters.

2.1.1 Expression and purification of recombinant SHANK3 proteins

To facilitate biophysical analyses of the molecular impact of ASD-associated SHANK3 missense mutants, a robust protein purification workflow was initially established. The SHANK3 protein of mice, rats and humans is very similar and contains a long proline-rich stretch proximal to the C-terminus exhibiting a high degree of disorder. Additionally, SHANK3 represents a large oligomerizing multidomain protein with many flexible linker regions so that a substantial aggregation tendency as well as limited solubility were expected during protein purification. For this reason, studies were focused on a truncated SHANK3 variant comprising amino acids 1 to 676 to include as many domains as possible while simultaneously reducing the content of disorder. This truncated protein contains the SPN, ARR, SH3 and PDZ domain but lacks the proline-rich region as well as the C-terminal SAM domain. Furthermore, such a truncation still allows to study potential distal structural effects as both mutations are located within the SPN domain (Fig. 4). Initial purification attempts focused on previously published procedures for a smaller SHANK3 fragment comprising only the SPN and ARR domain (Lilja et al., 2017).
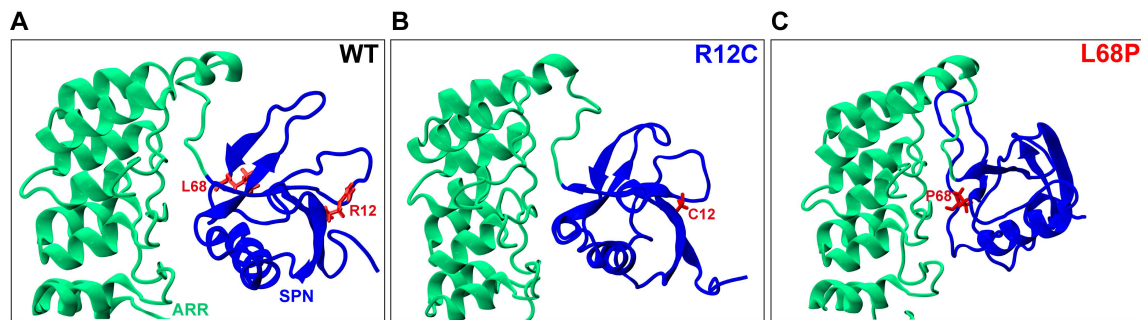
Figure 4: Localization of the ASD-associated mutated residues R12 and L68
(A) The position of the two affected amino acids R12 and L68 within the SPN domain (blue) of rat SHANK3 is highlighted in a WT situation. Side chains are represented as red sticks. (B) The R12C mutation is part of an antiparallel beta-sheet at the N-terminus of SHANK3. The residue is localized on the distal side of the SPN:ARR domain interface. (C) The L68P mutation is localized in close proximity to the SPN:ARR domain interface in a locally disordered region. The individual models represent energy minimized and equilibrated structures used as input for molecular dynamics simulations and were visualized with VMD 1.9.3.

To increase solubility, SHANK3$^{(1-676)}$ constructs were N-terminally fused to a His$_6$-SUMO-tag and were purified by immobilized metal affinity chromatography (IMAC) using a Ni^{2+} - iminodiacetic acid (IDA) resin (Profinity^{TM} IMAC resin, BioRad). However, all purified His$_6$-SUMO-SHANK3$^{(1-676)}$ variants (WT, R12C and L68P) displayed a substantial aggregation tendency and precipitated upon dialysis. Furthermore, cold denaturation was observed for all proteins and precipitation also occurred after thawing frozen protein aliquots. For this reason, a differential scanning fluorimetry (DSF) based buffer screen (RUBIC buffer screen, Molecular Dimensions) was performed to optimize buffer conditions for increased protein stability. Therefore conditions were screened for His$_6$-SUMO-SHANK3$^{(1-348)}$ WT as a shorter and easier to handle model protein containing only the SPN and ARR domain, which was purified by Ni^{2+} - IDA affinity chromatography according to a previously established protocol (Lilja et al., 2017). The purified protein is added to a reaction mix containing the screened buffer as well as the reporter substance SYPRO Orange in a 96-well plate. Upon thermal ramping the SYPRO Orange fluorescence increase is measured as a result of protein unfolding to detect the melting temperature under each condition. With this assay the effect of global parameters such as pH, salt concentration, buffer type and buffer concentration were measured and subsequently transferred to the purification of His$_6$-SUMO-SHANK3$^{(1-676)}$ variants. In line with previously reported buffer conditions for the purification of truncated SHANK3 proteins (Lilja et al., 2017) this screening procedure showed that the highest protein stability could be achieved in a sodium phosphate buffer system. In contrast, however, substantially higher concentrations of sodium phosphate (250 mM instead of 20 mM) resulted in a significant increase of protein stability. Furthermore, lowering the pH from 7.4 to 6.5 also showed to substantially stabilize the protein. Finally, the addition of sodium chloride had a moderately stabilizing effect depending on the buffer system. Based on these results a new buffer with adapted ionic strength and pH was made and used for subsequent purifications of His$_6$-SUMO-SHANK3$^{(1-676)}$ variants. Despite optimized buffer conditions as well as the addition of 50% (v/v) glycerol, freezing was not tolerated by any of the His$_6$-SUMO-SHANK3$^{(1-676)}$ variants causing protein precipitation upon thawing. For this reason, proteins needed to be prepared freshly and immediately prior to any type of downstream experiment.
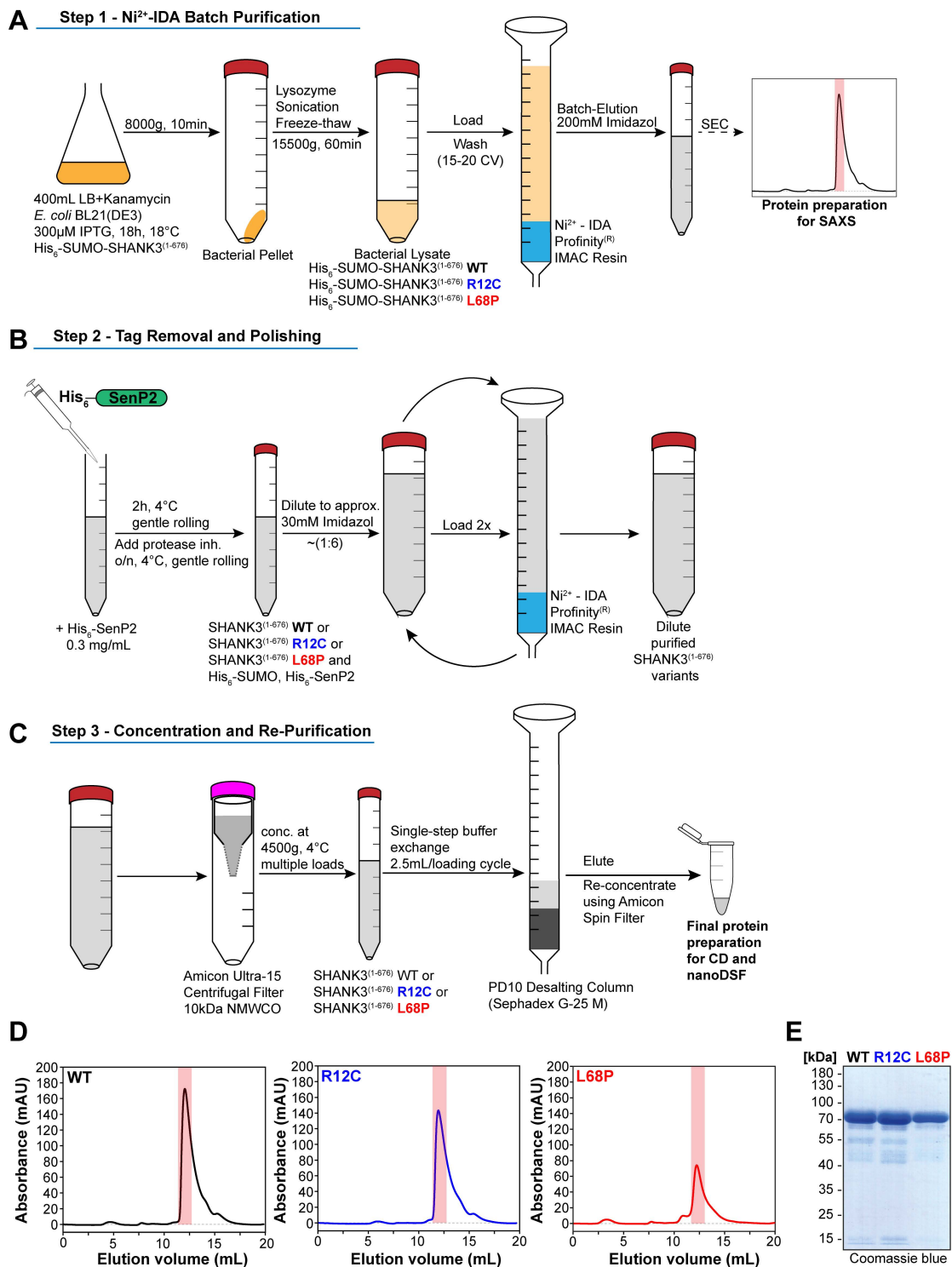
Figure 5: Protein purification workflow for the preparation of His_6-SUMO-SHANK3^(1-676) and SHANK3^(1-676) variants

(A) Recombinant His_6-SUMO-SHANK3^(1-676) variants (WT and mutant) were expressed in BL21(DE3) *E.coli* bacteria using 300 µM IPTG at 18 °C for 18 hours. Lysates were produced by lysozyme-treatment, sonication and a freeze-thaw-cycle and subsequently pre-purified over a Ni^{2+}- IDA column (bed volume ~ 2ml). Following batch-elution with 200 mM imidazole, proteins were re-purified by SEC using an analytical Superdex 75 10/300 GL column (200 µl sample volume; 0.4 ml/min; GE Healthcare) to achieve an appropriate sample quality for subsequent SAXS measurements. Selected peak fractions were pooled and concentrated. To facilitate measurements over a broader concentration range, the His_6-SUMO-tag was not removed for

SAXS studies. (B) To prepare samples for CD and nanoDSF measurements, the His_6-SUMO-tag was removed by treatment of the Ni^{2+}- IDA batch-eluted proteins with ~0.3 mg/ml His_6-SenP2. Subsequent removal of the cleaved His_6-SUMO-tag as well as His_6-SenP2 from the solution was achieved by initial dilution to reduce the imidazole concentration to ~ 30 mM followed by two passages over a freshly packed Ni^{2+}- IDA column (bed volume ~ 2 ml). (C) Dilute purified $SHANK3^{(1-676)}$ variants were sequentially concentrated by ultrafiltration to facilitate single-step buffer exchange over a PD10 desalting column (GE Healthcare). Finally, proteins were re-concentrated using Amicon spin filters (0.5 ml, 30 kDa NMWCO; Merck Millipore) to obtain preparations used in subsequent CD and nanoDSF measurements. (D) Representative size-exclusion chromatograms of WT and mutant His_6-SUMO-$SHANK3^{(1-676)}$ variants are shown (200 µl sample volume each). Individual peak regions from which fractions were pooled for SAXS sample preparation are highlighted. (E) Protein preparations of $SHANK3^{(1-676)}$ variants for CD and nanoDSF measurements are shown on an SDS-polyacrylamide gel.

Nonetheless, proteins could be stored in wet ice for up to a few days and were sufficiently stable in the new purification buffer to allow further processing after initial Ni^{2+} - IDA affinity purification (Fig. 5). To prepare protein samples for SAXS studies, His_6-SUMO-$SHANK3^{(1-676)}$ variants were pre-purified over Ni^{2+} - IDA and subsequently subjected to SEC for further purification and removal of imidazole (Fig. 5A). If the eluted proteins were stored on wet ice for more than a few hours in the presence of imidazole, precipitation was observed consistent with results from the RUBIC buffer screen showing a substantial destabilization of each variant by imidazole. Although all His_6-SUMO-$SHANK3^{(1-676)}$ variants were consistently purified in parallel using identical buffers and procedures, a reproducible reduction of the achievable protein yield for both mutants was apparent in the corresponding size-exclusion chromatograms (Fig. 5D). Thereby the yield for the R12C mutant was only mildly reduced compared to the WT while a significant decrease was present for the L68P mutant. The recombinant His_6-SUMO-tag was not removed for SAXS measurements to stabilize higher protein concentrations by increasing their solubility. Overall, His_6-SUMO-$SHANK3^{(1-676)}$ variants could be obtained in high yield and purity for low resolution structural characterization by SAXS.

On the other hand, CD and nanoDSF analyses required the removal of the tag with subsequent workup (Fig. 5B, C, E). This was achieved by the recombinant sentrin-specific protease 2 (SenP2), which was purified over Ni^{2+} - IDA with subsequent dialysis for buffer exchange. In contrast to the His_6-SUMO-$SHANK3^{(1-676)}$ variants, purified SenP2 was stable and could be stored for several months at -80 °C in the presence of 50% (v/v) glycerol. SenP2 represents a specific SUMO-protease and facilitated the efficient and quantitative deconjugation of the His_6-SUMO-tag from $SHANK3^{(1-676)}$ proteins. Apart from tag removal in solution, on-column cleavage of His_6-SUMO-$SHANK3^{(1-676)}$ variants bound to a Ni^{2+} - IDA column was tested. However, in this case most of the His_6-SUMO-$SHANK3^{(1-676)}$ proteins remained uncleaved possibly due to the binding of His_6-SenP2 to the column resulting in a sequestration from its substrate. Due to the decreased protein solubility after incubation with His_6-SenP2, the turbidity of the solution strongly increased indicating the onset of protein aggregation. After the subsequent addition of protease inhibitors and prolonged gentle agitation, however, the proteins remained soluble and could be further processed. After two passages over a freshly packed Ni^{2+} - IDA column both His_6-SenP2 as well as the His_6-SUMO-tag could be separated from $SHANK3^{(1-676)}$ in solution. Following a final concentration and single-step buffer exchange, soluble

SHANK3$^{(1-676)}$ variants (WT, R12C and L68P) could be obtained in sufficient quantity and quality for further biophysical measurements (Fig. 5E).

2.1.2 ASD-associated R12C and L68P mutant SHANK3 variants show altered protein topology and folding

SAXS represents a well suited method for the structural characterization of large, highly flexible and conformationally dynamic biological macromolecules in solution (Jeffries et al., 2021). Therefore, the low-resolution structure of purified ASD-associated SHANK3 mutants was investigated by SAXS to establish an initial structural understanding of the molecular impact of these missense mutations. To account for the potential presence of interparticle interactions, a dilution series ranging from the highest achievable protein concentration of each His$_6$-SUMO-SHANK3$^{(1-676)}$ variant to a maximum dilution of 0.5 mg/ml was made. Consequently, scattering curves of all three variants (WT, R12C and L68P) were measured separately in bulk mode for each individual concentration. Notably, all proteins were purified freshly and immediately prior to the measurement.

For a first characterization of obtained scattering data, the radius of gyration (R$_g$) was determined from plots of ln(I(s)) versus s^2 (squared scattering vector) according to Guinier's law (Fig. 6A-C). Thereby an increasing slope of the corresponding Guinier fits (i.e. higher R$_g$ values) was observed for increasing protein concentration. As R$_g$ is a measure for the compactness of a macromolecule and is related to its shape, a concentration-dependent increase of R$_g$ suggests the presence of interparticle interactions as well as higher particle anisometry at higher concentrations. By plotting the obtained R$_g$ values of each SHANK3 variant against the corresponding protein concentration, a strongly linear behavior is noticeable for the WT and R12C mutant (Fig. 6D). In contrast, the L68P mutant displays a non-linear and more pronounced increase of R$_g$ with concentration compared to the R12C mutant or the WT indicating potential structural changes related to higher interparticle interactions or altered protein conformation.

To further characterize whether His$_6$-SUMO-SHANK3$^{(1-676)}$ variants might be able to self-interact although no SAM domain is present, pair distance distribution functions (PDDFs) were calculated from SAXS profiles measured at different concentrations (Fig. 7A-C). From these functions, the maximum particle diameter (D$_{max}$) can be determined as an independent protein size indicator to analyze whether His$_6$-SUMO-SHANK3$^{(1-676)}$ variants display concentration-dependent size changes and thus undergo complex formation. Indeed, a clear concentration-dependent increase of D$_{max}$ values is visible from PDDFs of the WT and R12C mutant ranging from ~15 nm to ~30 nm between the lowest and highest concentrations, respectively. Due to the generally lower concentrations accessible for the L68P mutant, the full ~15 - 30 nm size range could not be observed. However, the same trend is present as D$_{max}$ values increase with concentration starting from ~15 nm. Collectively this data indicates that SHANK3 might be able to self-interact independent from the presence of a SAM domain. To determine the D$_{max}$ values of the WT and mutant proteins without the influence of such concentration-dependent effects, PDDFs were calculated from SAXS profiles extrapolated to zero-concentration (Fig. 7D). D$_{max}$ values obtained from these curves are in the range of ~14 - 15 nm for each variant (WT, R12C and L68P) and are thus in good agreement with PDDFs obtained at high dilution. Overall, these results suggest the presence of a dynamic concentration-

dependent monomer-dimer equilibrium in WT and mutant His$_6$-SUMO-SHANK3$^{(1\text{-}676)}$. An overview of principal parameters computed from SAXS data can be found in the appendix.
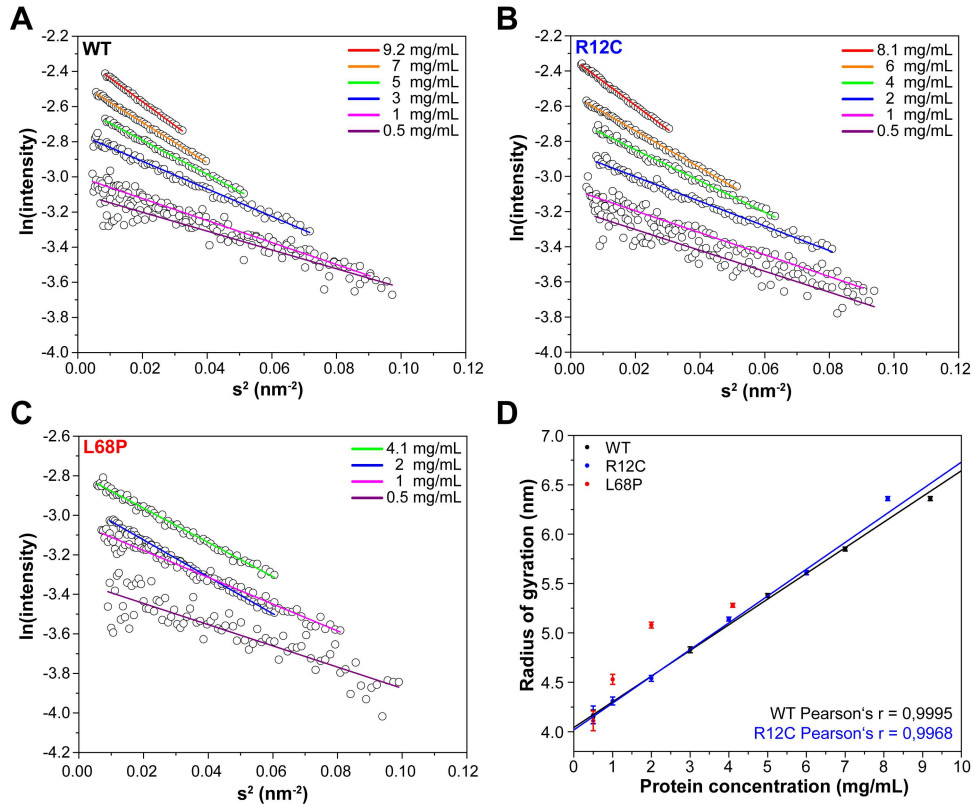
Figure 6: Concentration-dependent interparticle interactions of His$_6$-SUMO-SHANK3$^{(1\text{-}676)}$ variants

(A) Guinier fits of SAXS profiles from the WT show a protein concentration-dependent increase in their slope, corresponding to an increasing radius of gyration (R$_g$). (B) Compared to the WT, the R12C mutant exhibits a similar slope increase over the entire concentration-range. (C) The L68P mutant shows a non-linear concentration dependence of R$_g$, visible by the intersecting blue and magenta fitting lines. (D) R$_g$ values obtained from Guinier fits are plotted against the protein concentration. All Guinier regions were detected using the *AUTORG* function of the ATSAS 3.0.1 software package. The R$_g$ values of the WT and R12C mutant linearly depend on the protein concentration. For the L68P mutant, the non-linear increase of R$_g$ suggests increased interparticle interactions compared to the R12C mutant or the WT.

Since no atomic structure of such a large SHANK3 fragment is available but high-resolution structures of isolated single domains including the SPN, ARR, SH3 and PDZ domain have been published (Lilja et al., 2017; Ponna et al., 2017, 2018), structural models of both monomeric and dimeric His$_6$-SUMO-SHANK3$^{(1\text{-}676)}$ were created. Therefore, the corresponding high-resolution structure of each domain as well as solution scattering data were used as input for *CORAL* (ATSAS 3.0.1 software package) to model the individual WT and mutant His$_6$-SUMO-SHANK3$^{(1\text{-}676)}$ protein structures. Thereby, missing linker regions between the domains were filled with dummy residues (DRs) and domain positions were altered until they fitted the solution scattering data optimally. To obtain monomeric models, no symmetry restrictions were used (P1 symmetry) while

dimeric models were generated using P2 symmetry constraints. Monomeric *CORAL* models fitted the solution scattering data well and revealed that the SH3 and PDZ domain tend to be closely associated, consistent with previously reported data of a SHANK3 tandem SH3-PDZ domain construct (Fig. 8A and B; Ponna et al., 2018). Additionally, both ASD-associated SHANK3 mutants showed a variable degree of association of the SH3 and PDZ domain with the ARR domain suggesting the presence of distal structural effects (Fig. 8B). These models, however, do not allow to estimate the impact of both mutations on the SPN/ARR domain interface since the static high-resolution structure of the SPN-ARR domain tandem (PDB: 5G4X) has been used as input for the fitting procedure. Therefore, both domains were split *in silico* and subsequently used separately as input for *CORAL* modeling as done before. Here, the SPN-ARR linker region was replaced by DRs to allow free movement of the SPN domain.
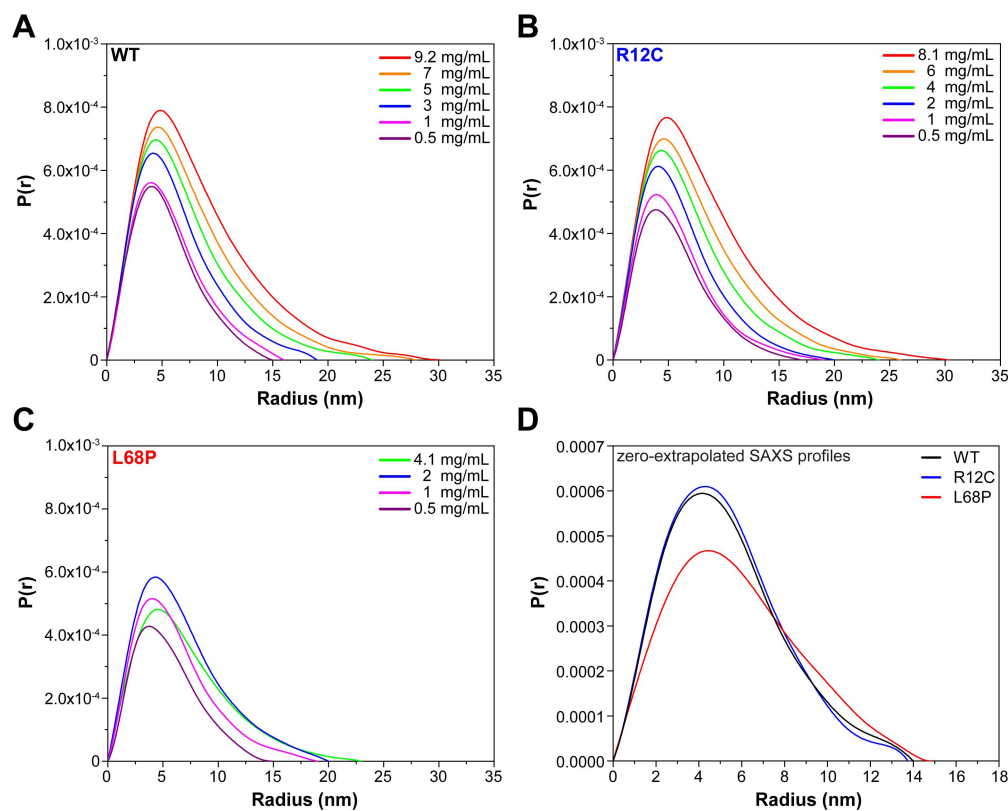
Figure 7: Concentration-dependent variation of His$_6$-SUMO-SHANK3$^{(1-676)}$ particle diameters

(A) Pair distance distribution functions (PDDFs) of His$_6$-SUMO-SHANK3$^{(1-676)}$ WT at indicated concentrations were obtained by the inverse Fourier transform method using the program *GNOM* from the ATSAS 3.0.1 software package. The maximum particle diameter (D$_{max}$) varies between ~15 - 30 nm over the measured concentration range indicating a monomer-dimer equilibrium. (B) PDDFs computed for the R12C mutant show a similar behavior compared to the WT with D$_{max}$ ranging from 17 - 30 nm. (C) For the L68P mutant, the experimentally accessible concentration-range is smaller compared to the R12C mutant or WT but PDDFs show the same trend with a steadily increasing D$_{max}$ starting at ~15 nm for the lowest concentration. (D) To remove oligomeric scattering contributions of WT or mutant proteins to the P(r) functions, the corresponding SAXS profiles were zero-extrapolated. Consistently, PDDFs computed from zero-extrapolated SAXS profiles reproduce monomeric D$_{max}$ values of ~14 - 15 nm for all variants.

Generally, this re-introduced additional flexibility slightly improved the corresponding χ^2 values (Fig. 8C). While the SPN domain remained associated with the ARR domain in the WT, both mutants displayed a decoupling of the SPN domain being more pronounced for the L68P mutant (Fig. 8D). Taken together, monomeric *CORAL* models of His$_6$-SUMO-SHANK3$^{(1-676)}$ variants demonstrate distal structural alterations, affecting the orientation of domains far away from the mutated site as well as a dominant perturbation of the SPN/ARR domain interface in the L68P mutant.
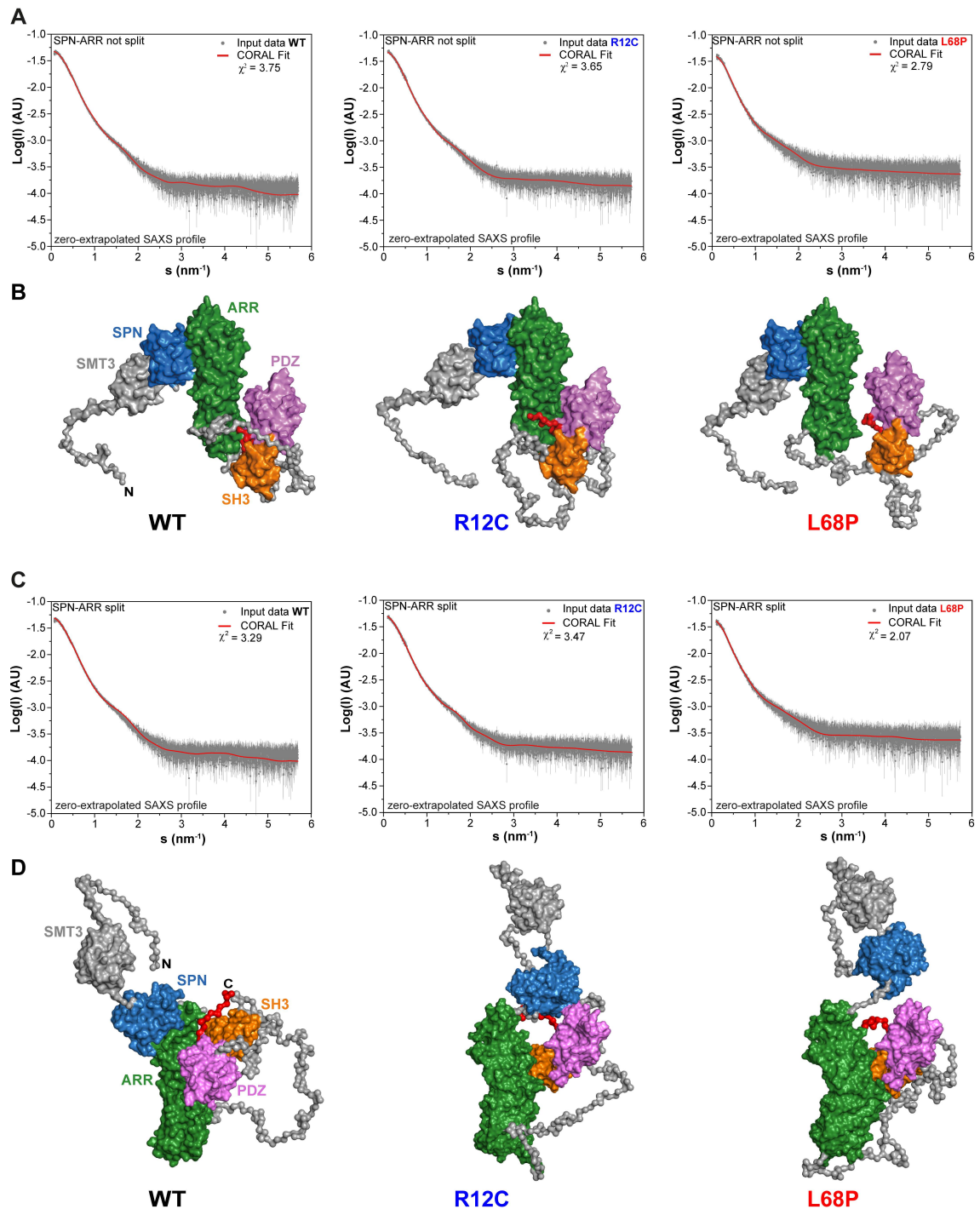
Figure 8: Rigid-body CORAL-derived structural models of monomeric His$_6$-SUMO-SHANK3$^{(1-676)}$ variants in solution

(A) To model the monomeric structure of His$_6$-SUMO-SHANK3$^{(1-676)}$ variants from solution scattering data, the corresponding zero-extrapolated SAXS profiles as well as high-resolution structures of individual domains (SMT3(aa 13–98): chain C from PDB 2EKE, SPN-ARR: PDB 5G4X, SH3: PDB 5O99, PDZ: PDB 5OVA) were used as input for the program *CORAL* of the ATSAS 3.0.1 software package. Thereby, the SPN and ARR domains were treated as a single rigid body. During the fitting procedure, input structures as well as linkers are oriented to optimally fit the scattering data (red lines). (B) The resulting structural models representing the final *CORAL* fits are shown. Linker regions were fitted as dummy residues. The models indicate that both mutations might alter the positions of the SH3 domain (orange) and PDZ domain (magenta) relative to the ARR domain (green) as well as the orientation of linker regions possibly suggesting distal structural effects of both mutations. (C) To account for possible mutation-induced perturbations of the SPN/ARR domain interface, zero-extrapolated SAXS profiles were fitted with *CORAL* using split SPN and ARR domains, where the corresponding linker region (treated as rigid body before) has been replaced by flexible dummy residues. The fitted scattering curve is shown as red line. (D) Corresponding structural models of monomeric His$_6$-SUMO-SHANK3$^{(1-676)}$ variants with split SPN and ARR domains show that the L68P mutation strongly decouples the SPN domain from the ARR domain while the WT model still indicates an interaction of both domains. For the R12C mutation, an intermediate situation is found, where the misplacement of the SPN domain is less pronounced compared to the L68P mutation. All acquired SAXS data including fits and models were deposited to SASBDB (WT: SASDLJ3, R12C: SASDLL3 and L68P: SASDLK3).

To eliminate concentration-dependent scattering contributions of dimeric His$_6$-SUMO-SHANK3$^{(1-676)}$, zero-extrapolated SAXS profiles were used to obtain monomeric *CORAL* models. On the other hand, *CORAL* models of dimeric His$_6$-SUMO-SHANK3$^{(1-676)}$ were constructed using SAXS profiles, which were merged between the highest and lowest concentration to account for the presence of dimeric species. As expected from Guinier and PDDF analyses, dimeric structural models fitted the solution scattering data equally well compared to monomers. Consistently, all variants indeed seem to be able to dimerize where the SH3 and PDZ domain represent the central complex forming units (Fig. 9A-C). Thereby the SH3 and PDZ domains of both His$_6$-SUMO-SHANK3$^{(1-676)}$ molecules associate to form a [(SH3)-(PDZ)]$_2$ cluster. While the dimeric complex topology of the WT and R12C mutant appears to be very similar, differences can be observed for the L68P mutant, where the orientation of the ARR domain is altered (Fig. 9C). However, a deviation of the fitted scattering curves (shown in red) from experimental data, which is present in the low angular range, indicates that the experimental scattering profiles do not exclusively represent dimeric His$_6$-SUMO-SHANK3$^{(1-676)}$ but rather suggest the presence of a dynamic monomer-dimer equilibrium.
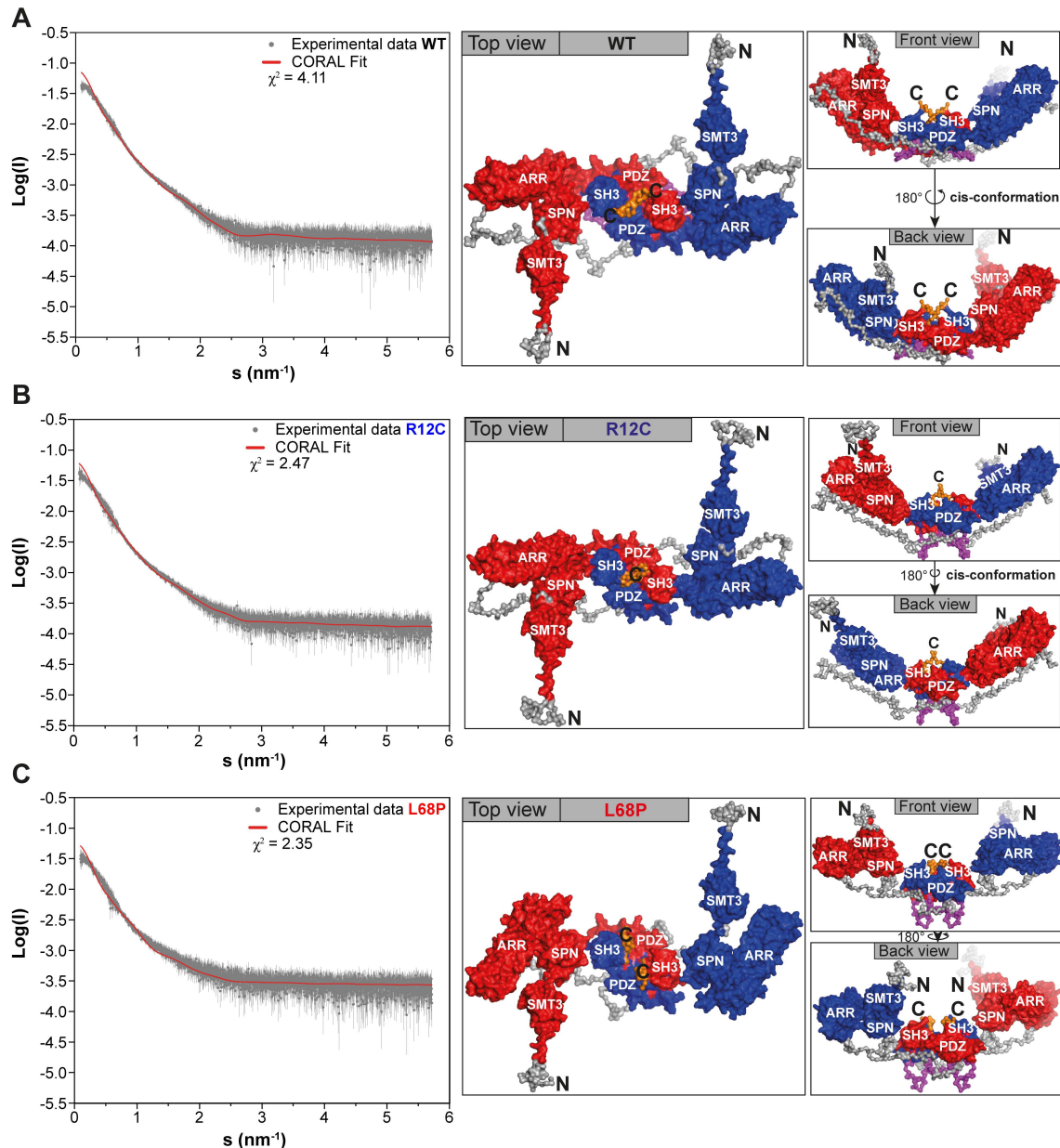
Figure 9: Rigid-body *CORAL*-derived dimeric His$_6$-SUMO-SHANK3$^{(1-676)}$ complex topology in solution

(A) The dimeric structural model of His$_6$-SUMO-SHANK3$^{(1-676)}$ WT was created using a merged SAXS profile (low angular range from lowest concentration data and higher angular range from highest concentration data) as input for *CORAL*. Fitting parameters were identical to those used for the monomeric models except that P2 (i.e. dimeric) symmetry restrictions were used. As the *CORAL* fit of the dimer is only slightly worse compared to the monomer fit (dimer χ^2 = 4.11 vs. monomer χ^2 = 3.75), the model suggests that SHANK3 might be able to dimerize also via its SH3 and PDZ domains. In the dimer, the ARR domains are oriented in a cis-conformation, which is visible in the front and back view. (B) No significant changes in the dimeric His$_6$-SUMO-SHANK3$^{(1-676)}$ complex topology are observed due to the R12C mutation. Generally, the fit is in good agreement with the experimental data (dimer χ^2 = 2.47 vs. monomer χ^2 = 3.65) but shows a slight deviation in the low angular range below 0.5 nm^{-1}. (C) The dimeric complex of His$_6$-SUMO-SHANK3$^{(1-676)}$ L68P shows an altered orientation of the ARR domains compared to the WT or R12C mutant. The dimer fit is in good agreement with the experimental data (dimer χ^2 = 2.35 vs. monomer χ^2 = 2.79) but shows a slight deviation below 0.5 nm^{-1}.

Using these previously created structural models as well as concentration-dependent SAXS profiles, the relative contribution of monomeric and dimeric His$_6$-SUMO-SHANK3$^{(1-676)}$ species to the total scattering can be determined for any given concentration. Consistent with other analyses, this approach directly showed a linear concentration dependence of the monomeric and dimeric His$_6$-SUMO-SHANK3$^{(1-676)}$ content in solution (Fig. 10). While at low concentrations monomers strongly dominate, dimers represent the more prominent species at higher concentrations. An equal distribution of monomers and dimers is reached at a concentration of approximately 5 mg/ml. Collectively, this data suggests that the SH3 and PDZ domain might not only facilitate selective ligand binding in dendritic spines but also be involved in the concentration-dependent regulation of SHANK3 self-interaction.
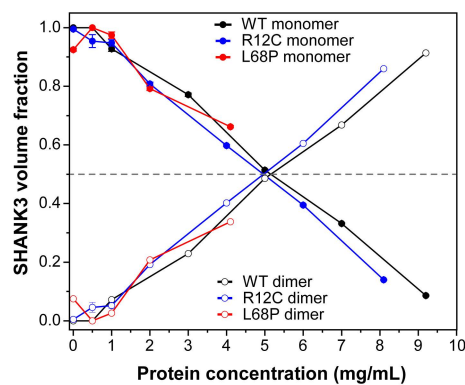
Figure 10: Concentration-dependent monomer-dimer equilibrium of His$_6$-SUMO-SHANK3$^{(1-676)}$ variants

Monomeric and dimeric volume fractions of His$_6$-SUMO-SHANK3$^{(1-676)}$ variants at individual concentrations were estimated using *OLIGOMER* from the ATSAS 3.0.1 software package. Therefore, monomeric and dimeric structural models obtained from *CORAL* analyses were fitted against SAXS profiles measured at different concentrations including zero-extrapolated SAXS data. The scattering contribution of monomers gradually decreases with increasing protein concentration suggesting a concentration-dependent monomer-dimer equilibrium. Consequently, dimeric volume fractions gradually increase with protein concentration. Higher order oligomers were not considered for this analysis.

The structural models generated from SAXS data not only facilitated the analysis of the monomer-dimer equilibrium but also suggested a perturbation of the SPN/ARR domain interface, indicative of mutation-induced (partial) unfolding. *CORAL*-based rigid body modeling, however, does not capture such unfolding events. Therefore, Kratky analysis of zero-extrapolated SAXS profiles was performed as the shape of resulting Kratky curves provides a qualitative estimate of protein folding (Blanchet & Svergun, 2013). Interestingly, the shape of Kratky curves for the WT and R12C mutant resembled a folded multidomain protein with a flexible linker while the L68P mutant exhibited a Kratky curve of a partially unfolded protein (Fig. 11). This is consistent with the significant perturbation of the SPN/ARR domain interface observed for the L68P mutant and might also explain the altered interparticle interactions seen from Guinier analysis. Furthermore, these Kratky analysis results imply that additional structural perturbations might exist on different levels such as secondary or tertiary structure.
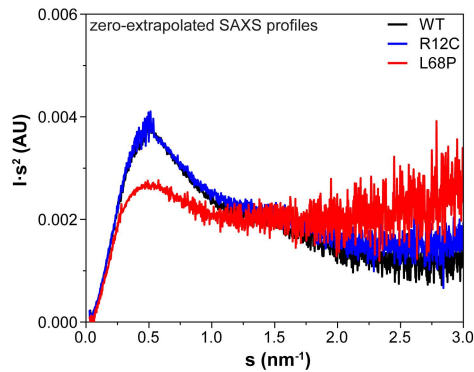
Figure 11: Kratky analysis shows partial unfolding of the L68P mutant
The shape of Kratky curves obtained for WT as well as R12C mutant His$_6$-SUMO-SHANK3$^{(1-676)}$ indicate the presence of a folded multidomain protein with flexible linkers. In contrast, Kratky analysis of the L68P mutant reveals a curve shape resembling a partially unfolded protein. To eliminate concentration-dependent effects on protein folding, all Kratky analyses were performed using zero-extrapolated SAXS profiles.

Overall, the structural characterization of ASD-associated His$_6$-SUMO-SHANK3$^{(1-676)}$ variants in solution by SAXS demonstrated that SHANK3 might generally exhibit a more complex mechanism of regulated self-interaction involving the SH3 and PDZ domain, which might facilitate N-terminal oligomerization of SHANK3. Additionally, local and distal mutation-induced structural perturbations affecting the SPN/ARR domain interface as well as the SH3 and PDZ domain orientation have been detected. This is further corroborated by the finding that the L68P mutant induces partial unfolding, which needs to be characterized in more detail using alternative methods.

2.1.3 The L68P mutant disrupts the tertiary structure of SHANK3 and induces an increased surface hydrophobicity

Due to the dependence of fluorescence signals on the immediate environment and emission timescales in the nanosecond range, fluorescence spectroscopy represents a well suited technique to study protein folding and unfolding as well as the reaction of proteins to external perturbations such as thermal ramping (Royer, 2006). This allows to analyze ASD-associated mutation-induced structural perturbations in more detail and provides information on the thermal stability of the SHANK3 tertiary structure.

SAXS data suggested structural alterations in both mutants but only for the L68P mutant partial unfolding was detected. To independently analyze potential folding differences in His$_6$-SUMO-SHANK3$^{(1-676)}$ variants, intrinsic tryptophan fluorescence emission spectroscopy was performed (Fig. 12A). Consistently, the L68P mutant showed a significantly reduced fluorescence intensity compared to the WT or R12C mutant, which might be caused by an increased fraction of exposed tryptophan residues leading to increased solvent quenching. An increased surface exposure of tryptophan residues in turn suggests a disruption of the tertiary structure in the L68P mutant. This is further corroborated by extrinsic fluorescence emission spectroscopy using 1-anilinonaphthalene-8-sulphonate (ANS) as reporter dye to titrate hydrophobic surface patches of His$_6$-SUMO-SHANK3$^{(1-676)}$ WT, R12C or L68P. Thereby the R12C mutant did not show significant changes in the ANS fluorescence intensities resulting from binding

to hydrophobic surface spots compared to the WT (Fig. 12B and C). In contrast, the L68P mutant exhibited a strong increase of ANS fluorescence intensities corresponding to an increased surface hydrophobicity, indicative of mutation-induced partial unfolding (Fig. 12D). Collectively, these results validate the initial SAXS data and illustrate that the L68P but not the R12C mutant display an impaired tertiary structure as well as increased surface hydrophobicity.
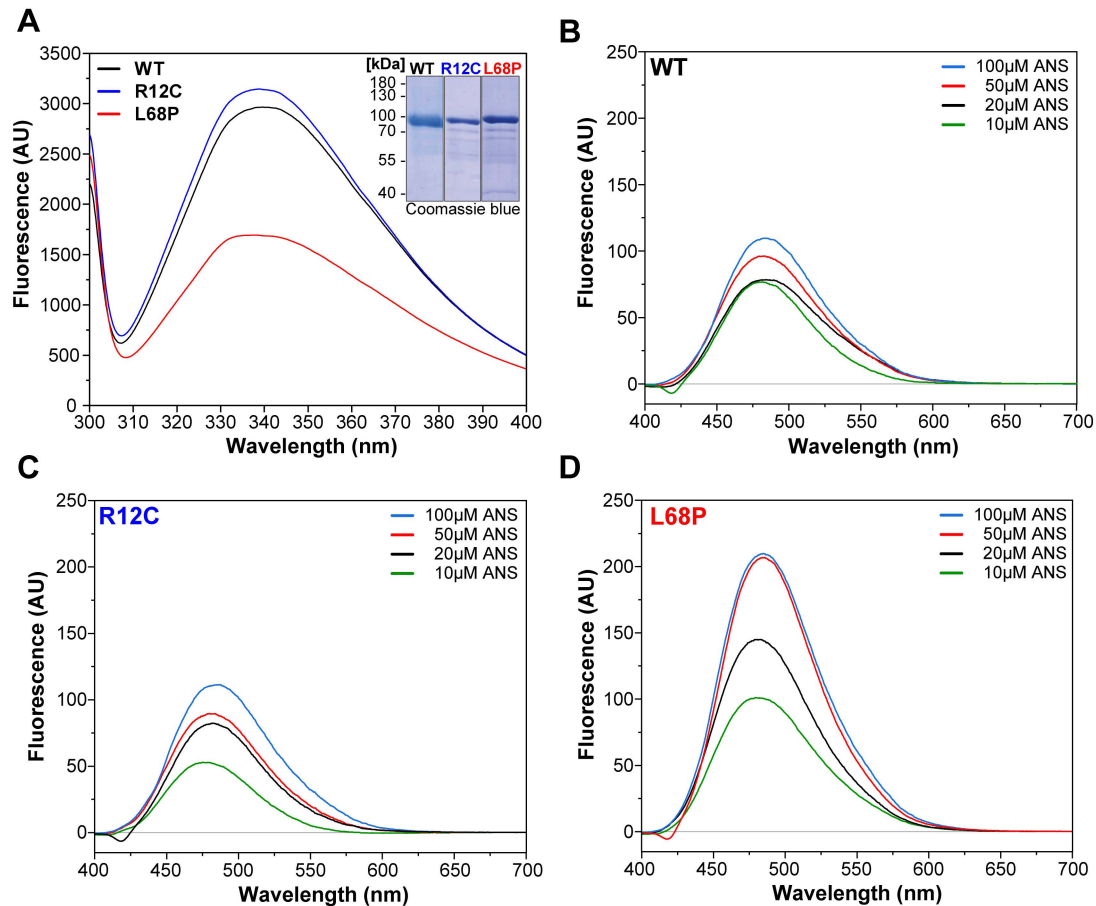
Figure 12: Mutation-induced structural changes monitored by intrinsic and extrinsic fluorescence spectroscopy

(A) Intrinsic tryptophan fluorescence emission spectra were recorded from 2 µM His$_6$-SUMO-SHANK3$^{(1-676)}$ variants at room temperature in a 10 mm rectangular quartz cell (excitation wavelength = 295 nm, scan speed = 240 nm/min). The L68P mutant shows a strongly reduced fluorescence intensity compared to the R12C mutant or WT protein. The inset shows representative His$_6$-SUMO-SHANK3$^{(1-676)}$ protein preparations on an SDS-polyacrylamide gel. (B) The surface hydrophobicity of His$_6$-SUMO-SHANK3$^{(1-676)}$ WT (2 µM) was measured by extrinsic fluorescence spectroscopy in the presence of 10 - 100 µM ANS at room temperature in a 10 mm rectangular quartz cell (excitation wavelength = 365 nm, scan speed = 240 nm/min). As expected, the ANS fluorescence intensity (emission maximum at 480 nm) increased by titrating the protein with up to 100 µM ANS showing increased binding to hydrophobic surface spots. (C) Besides a slight reduction of the fluorescence intensity at 10 µM ANS, no significant changes in the surface hydrophobicity of the R12C mutant is observed compared to the WT. (D) For the L68P mutant the fluorescence intensity is generally increased significantly for each ANS concentration, indicating an increased protein surface hydrophobicity.

To probe whether the observed alterations in the tertiary structure of L68P mutant SHANK3 result in changes of the thermal stability, intrinsic fluorescence emission was recorded at 350 nm and 330 nm as a function of temperature using nano differential scanning fluorimetry (nanoDSF). Compared to conventional fluorescence spectroscopy, this capillary-based technique allows the parallel measurement of up to 48 samples, requires substantially less amounts of protein and thus facilitates the analysis of multiple different conditions at the same time (Alexander et al., 2014). To avoid the measurement of artificial melting temperatures due to a potential contribution of the recombinant His_6-SUMO tag to thermal transitions, the tag was removed during protein purification (Fig. 13A). This, however, also decreases the solubility of the purified proteins and increases the risk for aggregation of the unfolded state. Therefore, different concentrations of urea in the range of 0.25 M - 2.0 M were added to the individual samples to suppress aggregation without unfolding the proteins. Nonetheless, protein precipitates were still visible after thermal denaturation runs even in the presence of 2.0M urea, although aggregation was strongly reduced. This highlights the irreversibility of thermally induced unfolding of SHANK3$^{(1-676)}$ variants, a principle which has been generally described for many larger multi-domain proteins (Strucksberg et al., 2007). All SHANK3$^{(1-676)}$ variants presented a complex multistep melting behavior which might partially arise from the presence of a tryptophan reporter residue in every individual domain (Fig. 13A). Depending on the dynamics and interactions of these domains during thermal ramping, emission maxima of individual tryptophan residues might shift in both directions (Vivian & Callis, 2001).

A

● Trp reporter residues within SHANK3$^{(1-676)}$

B

	T_m 1 (°C)	T_m 2 (°C)	T_m 3 (°C)
WT Ctrl	-	51.2	57.4
WT +0.25M Urea	44.9	49.9	57.0
WT +0.5M Urea	43.6	49.7	55.4
WT +1.0M Urea	39.4	47.4	54.3
WT +2.0M Urea	32.8	42.8	50.4
R12C Ctrl	-	-	53.3
R12C +0.25M Urea	41.6	-	55.4
R12C +0.5M Urea	42.6	48.7	54.6
R12C +1.0M Urea	37.9	47.0	54.3
R12C +2.0M Urea	34.5	43.6	51.3
L68P Ctrl	-	38.6	51.8 (46.1)*
L68P +0.25M Urea	-	39.1	51.5
L68P +0.5M Urea	-	39.2	50.7
L68P +1.0M Urea	-	40.1	50.2
L68P +2.0M Urea	28.6	35.3	50.7

* This transition point corresponds to the detected shoulder in the L68P Ctrl curve (first derivative)

C

D

Figure 13: The R12C and L68P mutation differentially affect the tertiary structure of SHANK3

(A) On the top, a schematic overview of the SHANK3$^{(1-676)}$ fragment including the SPN, ARR, SH3 and PDZ domain is shown. Below, the corresponding structural model of the WT protein is depicted, which was derived from SAXS measurements. Intrinsic tryptophan (Trp) reporter residues are highlighted in red. (B) The table shows an overview of detected melting points corresponding to the thermal stability of the tertiary structure of the WT and mutant proteins. The effect of non-denaturing urea concentrations up to 2.0 M on the melting temperatures of WT and mutant proteins are depicted. Due to the complex melting behavior, melting was classified in three partially overlapping thermal transition zones (T_m1 - T_m3). (C) Label-free intrinsic fluorescence emission was recorded at 350 nm and 330 nm over a temperature range of 15 - 90 °C (heating rate 1 °C/min) in the presence of different urea concentrations. The fluorescence ratio (350/330 nm) is depicted as a function of temperature. Melting curves were acquired in parallel using standard nanoDSF grade capillaries each filled with 10 µl of ~0.5 mg/ml SHANK3$^{(1-676)}$ (WT or mutant) at 50% excitation power. (D) First derivatives were made from the corresponding melting curves to facilitate the detection of thermal transition points. Resulting peaks indicate individual melting points and are highlighted with colored arrowheads (color-coded according to the transition zones). As expected, melting points shift towards lower temperatures with increasing urea concentrations. The L68P mutant generally shows markedly reduced melting temperatures compared to the WT or R12C mutant, indicating an impaired thermal stability of the tertiary structure.

Consequently, the detected melting temperatures had to be classified into three thermal transition zones (T_m1 - T_m3) to account for this melting behavior (Fig. 13B). The detection of thermal transition points was accomplished by peak analysis of corresponding first derivative curves, which were generated from fluorescence ratio plots (F 350/330 nm vs. temperature; Fig. 13C and D). While both the WT and L68P mutant showed two distinct thermally separatable transitions in the absence of urea related to the presence of unfolding intermediates visible as a double peak in the first derivative curve, the R12C mutant exhibited only a single transition (i.e. a single peak). This might reflect a mutation-induced change in the coupling of interaction networks within SHANK3$^{(1-676)}$ R12C. Additionally, the L68P mutant generally displayed lower melting temperatures compared to the R12C mutant or WT demonstrating a mutation-induced impairment of the tertiary structure stability. Furthermore, the L68P mutant exhibited a more pronounced shift towards lower melting temperatures upon addition of urea suggesting a higher structural susceptibility. Overall, these results demonstrate mutation-induced changes in the coupling of interaction networks within the protein as well as impaired thermal stability of the L68P mutant tertiary structure.

2.1.4 The autism-associated R12C and L68P mutations alter secondary structure stability and unfolding cooperativity of SHANK3

To understand whether the observed impact of both mutations on the tertiary structure of SHANK3 correlates with mutation-induced alterations of the secondary structure, far-ultraviolet circular dichroism (far-UV CD) spectroscopy was performed on the identical samples, which were used for nanoDSF measurements to ensure comparability. Since the peptide bond of the protein backbone acts as chromophore in the far-UV below 240 nm, this technique readily provides substantial information on secondary structure stability and folding properties (Kelly et al., 2005). However, it has been reported

previously that conformational distributions populated by chemically and thermally denatured proteins may differ substantially (Narayan et al., 2019). For this reason, not only thermal but also equilibrium chemical denaturation experiments were conducted to optimally complement nanoDSF experiments. Therefore, purified SHANK3$^{(1-676)}$ variants were first incubated with increasing concentrations of urea and secondary structure unfolding was monitored by measuring ellipticities at 222 nm. As the CD signal at 222 nm reports on the α-helical content of a protein, the contribution of other secondary structure elements is not directly measured. However, crystallographic structures of the individual domains within SHANK3$^{(1-676)}$ confirm the presence of a substantial α-helical content such that ellipticities at 222 nm serve as appropriate readout for secondary structure unfolding. While nanoDSF measurements clearly demonstrated mutation-induced alterations in the tertiary structure stability, isothermal equilibrium chemical unfolding does not show major differences in the transition midpoint concentration of both mutants compared to the WT (c_m = 3.3 mol/L [WT], 3.4 mol/L [R12C], and 3.1 mol/L [L68P]) on a secondary structure level (Fig. 14A). Nonetheless, chemical unfolding curves fitted with a two-state unfolding transition model, showed differences in the corresponding slopes of the folded and unfolded states, which were obtained using the linear extrapolation method (LEM) indicating that stability differences might still be present.
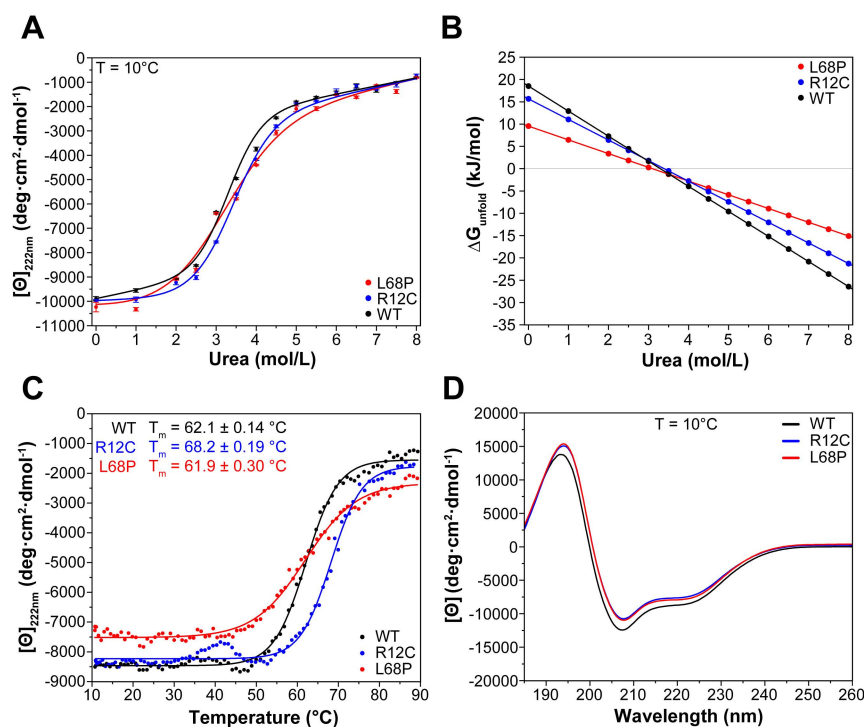
Figure 14: Secondary structure stability and folding assessment of ASD-associated SHANK3 mutants by CD spectroscopy

(A) To address the impact of both mutations on the secondary structure of SHANK3, isothermal chemical unfolding using urea as denaturant was performed. Therefore, ellipticities of SHANK3$^{(1-676)}$ WT, R12C or L68P were measured in the presence of 0 - 8 M urea at 222 nm (3 s/point, 25 µs sample period, T = 10.0 ± 0.2 °C, protein concentration ~0.15 mg/ml). Individual data points are averages from three repeated measurements and have been buffer subtracted. Fitting was performed using a two-state unfolding transition model. Therefore, slopes of the folded and unfolded baselines were obtained by linear extrapolation. No significant difference of the transition midpoints was found. (B) To calculate the free energy of unfolding (ΔG_{unfold}) based on a linear free

energy model, parameters obtained from the two-state unfolding transition fit were used. Both mutants show reduced ΔG_{unfold} values in the absence of any denaturant, indicating a reduced thermodynamic stability. Additionally, the slope of both mutants is reduced compared to the WT demonstrating a reduced unfolding cooperativity. (C) Thermal unfolding has been measured with protein samples used in (A) containing 2.0 M urea to prevent protein aggregation upon thermal ramping (222 nm, 3 s/point, 25 µs sample period, 10–90 °C, 1.0 °C step size, 1.0 °C/min stepped ramping with 30 s settling time and 0.5 °C tolerance). An increased secondary structure stability of the R12C mutant is visible only by thermal denaturation but not by chemical denaturation, suggesting differences in thermally and chemically denatured protein states (dynode voltage = 370–400 V between 10 and 90 °C). (D) Far-UV CD spectra of SHANK3[(1-676)] variants suggest no major folding impairments in the secondary structure of both mutants (260 - 185 nm, 0.5 nm step size, 3 s/point, 25 µs sample period, three repeats, T = 10.0 ± 0.2 °C. Immediately before measurement, proteins were buffer exchanged to 10 mM KH_2PO_4, 100 mM KF, 0.5 mM DTT, pH = 6.50. All measurements were performed in a 1 mm quartz cell (Hellma Analytics).

Consequently, the free energy of unfolding (ΔG_{unfold}) was determined from these fits as a function of denaturant concentration. Thereby, the cooperativity parameter m_G relates ΔG_{unfold} with the denaturant concentration [D] and represents the slope in the corresponding plots (Fig. 14B). Both mutants exhibited a reduced cooperativity parameter and reduced ΔG^0 values (ΔG^0 = 18.5 kJ/mol [WT], 15.6 kJ/mol [R12C], 9.5 kJ/mol [L68P]) demonstrating a general mutation-induced destabilization of the secondary structure, which is significantly more pronounced for the L68P mutant. Additionally, this secondary structure destabilization appears to be different from the observed destabilizing effects on the tertiary structure. While the presence of 2.0M urea significantly reduced the observed transition temperatures of the L68P mutant in nanoDSF experiments (Fig. 13B), no significant secondary structure unfolding could be observed under this condition by CD spectroscopy (Fig. 14A). Consequently, thermal unfolding of SHANK3[(1-676)] variants was monitored at 222 nm using the corresponding chemical unfolding samples containing 2.0 M urea to prevent that protein aggregation might precede secondary structure melting. Notably, melting temperatures acquired in this way proved to be substantially higher compared to those obtained from nanoDSF experiments under the same condition (Fig. 14C; CD: ~62 - 68 °C vs. nanoDSF: ~29 - 51 °C). Surprisingly, no reduction of the thermal stability was evident for the L68P mutant while the R12C mutant showed an increased melting temperature by ~6 °C compared to the WT (Fig. 14C). Furthermore, these stability differences do not seem to arise from an altered secondary structure content of both mutants since no significant discrepancies are found in the corresponding far-UV CD spectra (Fig. 14D). This is in line with results from limited proteolysis experiments suggesting a mildly reduced proteolytic cleavage susceptibility for the R12C mutant (Figure 15). Overall, these results demonstrate that both ASD-associated missense variants have a clearly distinguishable molecular impact on the secondary and tertiary structure, which is evident in their differential susceptibility to either chemical or thermal perturbations as well as in significantly different melting temperatures detected for either secondary or tertiary structure unfolding. Ultimately, both mutants display a reduced chemical unfolding cooperativity as well as changes in their stability.
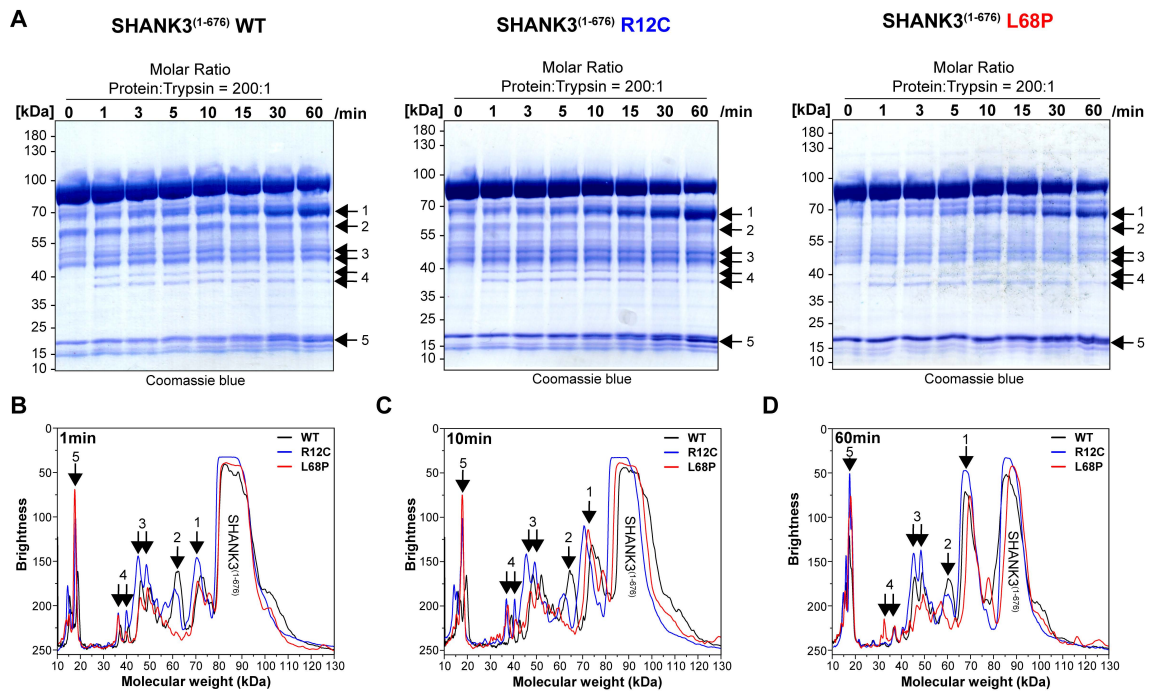
Figure 15: Altered cleavability of SHANK3$^{(1-676)}$ mutants by trypsin

(A) Limited trypsin proteolysis of SHANK3$^{(1-676)}$ variants over a total of 60 min is shown on an SDS-polyacrylamide gel. To achieve a molar protein:trypsin ratio of 200:1, 13.5 µM (1 mg/ml) SHANK3$^{(1-676)}$ (WT, R12C or L68P) was incubated with 67 nM trypsin-EDTA (Gibco, Thermo Fisher) in an 8x reaction mix (120 µl) at room temperature. From this reaction mix, an aliquot of 15 µl was removed at each timepoint and immediately added to 15 µl of preheated 2x SDS-Loading Buffer at 95 °C. All samples were heated to 95 °C for 5 min and subsequently analyzed by SDS-PAGE. Additional fragments start to appear already after 1 min of incubation. (B) Line profiles of SDS-PAGE lanes after 1 min were measured in Fiji (line width = 15 px) and are overlaid from all protein variants. The molecular weight was estimated based on corresponding SDS-PAGE marker bands (PageRuler, 10 - 180 kDa, Thermo Fisher). Individual fragments of the R12C mutant related to the regions 1 and 3 show a higher abundance (i.e. lower brightness) compared to the WT or L68P mutant. The fragment in region 2 is present in the WT and R12C mutant but absent in the L68P mutant. (C) After 10 min, no major differences are evident compared to 1 min of limited proteolysis. Notably, the fragment in region 1 is more abundant in both mutants compared to the WT. (D) After 60 min, the fragment profile is consistent with the one observed after 1 min of limited proteolysis. In the regions 1 and 3 the R12C mutant shows more abundant fragments compared to the WT and L68P mutant. Overall, however, both mutants tend to exhibit higher amounts of residual uncleaved protein compared to the WT.

2.1.5 The R12C and L68P mutations affect molecular dynamics of the peptide backbone on a nanosecond timescale

The results outlined above indicated several mutation-induced changes related to structural stability, folding, interparticle interactions or cooperativity but do not provide information on how SHANK3 responds dynamically to the perturbation of introducing autism-associated missense mutations. Consequently, using the existing high-resolution X-ray structure of an N-terminal SHANK3 fragment (PDB: 5G4X; Lilja et al., 2017), molecular dynamics simulations (MDS) allow to capture this behavior in atomic detail and with high temporal resolution providing a link between protein structure and dynamics (Hollingsworth & Dror, 2018). Therefore, the amino acid substitutions R12C or L68P were inserted into the corresponding X-ray structure of SHANK3$^{(1-346)}$ (PDB:5G4X) by manual rotamer selection using UCSF Chimera (Pettersen et al., 2004). Previous work showed that long MD trajectories are necessary to effectively sample the conformational space of SHANK3$^{(1-346)}$ (data not shown) such that 1 µs trajectories were calculated for each variant. Of note, this timescale is not sufficient to capture potential mutation-induced protein unfolding in a standard atomistic MDS as folding and unfolding events are typically much slower (Klepeis et al., 2009). Therefore, MDS of SHANK3$^{(1-346)}$ variants are restricted to the observation of structural rearrangements in the folded state as well as the analysis of conformational dynamics on a nanosecond timescale.

To address the question whether the studied ASD-associated missense variants modify the conformational flexibility of SHANK3$^{(1-346)}$, root mean square fluctuation (RMSF) analyses of C_α atoms were performed (Fig. 16A). Thereby, the highest fluctuations were generally observed within the first 100 residues, corresponding to the SPN domain. Both mutants resulted in an increase of conformational flexibility, which was most prominent within the SPN domain harboring the corresponding mutated sites (Fig. 16A). Importantly, however, root mean square deviation (RMSD) analyses of C_α atoms revealed that increased dynamics of both mutants exist only in the early phase of the MDS and diminish with longer simulation time (Fig. 16B). For the WT protein, a conformational change is visible as steep RMSD increase after ~500 ns, which is absent in both mutants. Additionally, the WT protein consistently shows higher RMSD values compared to the mutants following this conformational change (Fig. 16B). Considering the RMSF analysis, which suggested the SPN domain as local flexibility hotspot, separate RMSD analyses were performed for the SPN and ARR domain to resolve individual contributions of both domains to the observed overall dynamics (Fig. 16C-D). As expected, the obtained RMSD plot for the SPN domain alone displayed the same characteristics as the full protein with significantly higher absolute values, corroborating the relatively higher contribution of the SPN domain to the overall dynamics (Fig. 16C). On the other hand, RMSD analysis of the ARR domain revealed a stepwise RMSD increase over the course of the whole trajectory for the WT protein, while only little dynamics without any significant events was observed for both mutants (Fig. 16D). This mutation-induced discrepancy in the dynamics of the ARR domain, however, points to a distal impact of both mutations, which are localized within the SPN domain. Consequently, both mutations seem to be able to alter the protein structure and dynamics several hundred amino acids away from the mutated site, likely via changes in the coupling of intramolecular interaction networks. Finally, structural alignments of every hundredth frame of each trajectory visualized the high dynamics of the SPN domain as suggested by the RMSF and RMSD analyses (Fig. 16E).
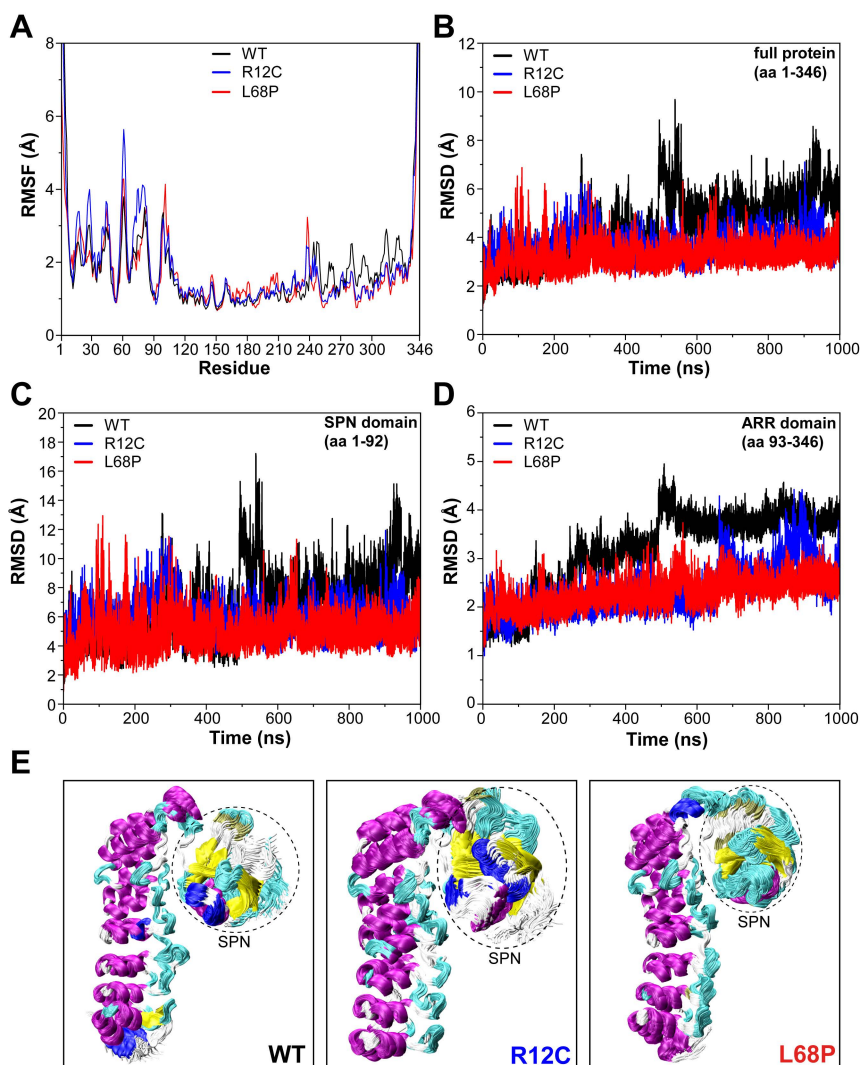
Figure 16: Conformational dynamics of SHANK3 mutants studied by molecular dynamics simulations

(A) From atomistic molecular dynamics simulations calculated for the SHANK3$^{(1-346)}$ fragment (PDB: 5G4X) either as WT or carrying one of the mutations R12C or L68P, C$_\alpha$ backbone RMSF was determined using VMD 1.9.3. Backbone movements were generally found to be largest within the first 100 amino acids (aa) corresponding to the SPN domain (aa 1 - 92), which exhibits significantly more flexibility than the ARR domain (aa 112 - 337). These structural movements were further enhanced by the R12C and L68P mutation. (B) The C$_\alpha$ backbone RMSD was determined for the full protein (aa 1-346) each and shows changes in protein conformation occurring over time. After ~500 ns a prominent conformational switch was observed in the WT protein, which is absent in both mutants. While both mutants tend to exhibit mildly increased RMSD values within the first 100 ns, on average their conformational dynamics is lower compared to the WT. (C) C$_\alpha$ backbone RMSD analysis restricted to the SPN domain (aa 1 - 92) reveals a pattern identical to the full protein but with significantly larger absolute values. (D) Upon restriction of the C$_\alpha$ backbone RMSD to the ARR domain a different pattern is observed compared to the full protein or SPN domain. The WT ARR domain shows a continuous RMSD increase until ~500 ns, where a conformational switch is seen as a pronounced step of RMSD increase. This behavior is absent for the ARR domain of both mutants, which show less RMSD variation and dynamics. (E) Overlays of individual frames of each trajectory (every fifth frame loaded, overlay [beginning:step:end] = 0:20:20002 resulting in 1000 images) highlight the SPN domain as hotspot of localized flexibility and conformational dynamics.

Collectively, MDS of WT and mutant SHANK3[(1-346)] revealed a profound influence of both mutations on the conformational flexibility and dynamics locally within the SPN domain as well as distally in the ARR domain, which does not harbor the mutated sites themselves. Overall, molecular dynamics of the peptide backbone was reduced in both mutants as measured by RMSD, while increased fluctuations were evident in mutant SPN domains. Ultimately, the mutants lack conformational transitions observed for the WT protein. Since limitations in the accessible simulation time prevent the detection of mutation-induced (partial) unfolding, which has been suggested by previous experiments, the expected increase in conformational dynamics of mutant proteins is not observed.

Mutation-induced changes in the dynamics of the distal ARR domain are consistent with previous SAXS data and raise the question how such effects might be transmitted from the mutant locus. Therefore, the linker region connecting the SPN and ARR domain was split *in silico* followed by capping of the newly generated termini leaving only the domain interface as remaining interaction site. Subsequently, MDS as described above were repeated for each variant. Interestingly, the domains remained bound to each other throughout the WT and mutant trajectories. Consistent with previous MDS, RMSF analysis revealed an increased conformational flexibility of both mutants, which was more pronounced after splitting the linker region (Fig. 17A). Surprisingly, however, RMSD analysis showed reduced dynamics of the WT protein while both mutants displayed significantly increased RMSD values compared to previous simulations (Fig. 17B). This unexpected reduction in the WT protein after linker disconnection might be explained if the linker region is involved in the transmission of conformational dynamics from the SPN domain to the ARR domain. Nonetheless, the RMSD values of the R12C mutant continuously increased during the trajectory while the L68P mutant showed a pronounced RMSD jump after ~80 - 90 ns, which subsequently remained stable for several hundred nanoseconds (Fig. 17B). This behavior was present not only in the SPN domain itself but also in the decoupled ARR domain, suggesting an additional contribution of other processes to the transmission of conformational dynamics such as non-covalent interactions at the domain interface or with the environment (Fig. 17C and D). Finally, the orientation of the SPN and ARR domains as well as their dynamics were visualized by overlays of every hundredth frame of each trajectory (Fig. 17E). Taken together, MDS of the artificially split system of SHANK3[(1-346)] provided additional insight into potential mechanisms of coupled conformational dynamics within SHANK3 and demonstrated that both ASD-associated mutations might be capable of altering such conformational crosstalk.
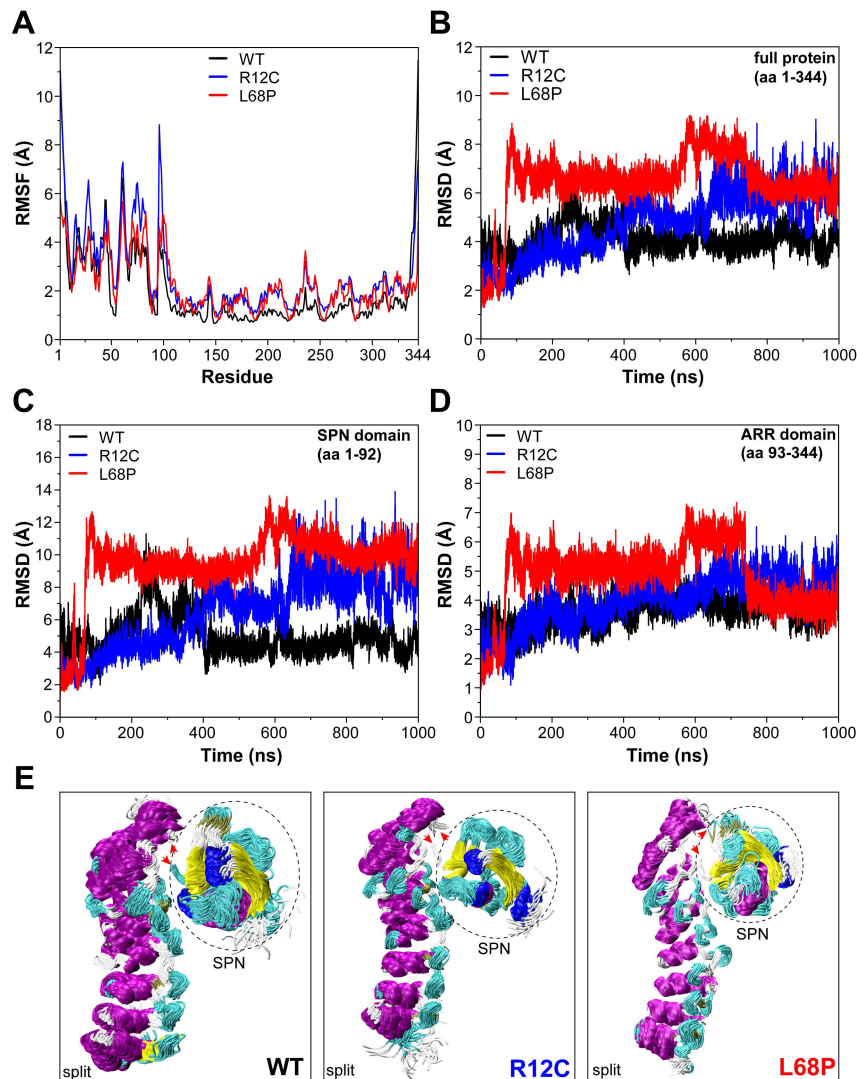
Figure 17: Conformational dynamics of SHANK3 mutants exhibiting split SPN- and ARR-domains

(A) Atomistic molecular dynamics simulations were calculated for the SHANK3[(1-346)] fragment (PDB: 5G4X; either as WT or carrying the R12C or L68P mutation), where the SPN and ARR domain were split *in silico* in the linker region to specifically probe the dynamics of the SPN:ARR domain interface. Termini produced by splitting of the domains needed to be capped such that the finally prepared input structure was truncated by 2 aa. C_α backbone RMSF was determined using VMD 1.9.3. Both mutants show increased structural movements within the first 100 aa. (B) C_α backbone RMSD analysis of the full protein revealed significantly enhanced dynamics of both mutants compared to the WT. Notably, the L68P mutant shows a prominent RMSD increase after ~100 ns potentially reflecting a perturbation of the SPN:ARR domain interface. (C) C_α backbone RMSD analysis restricted to the SPN domain resulted in the same pattern as for the full protein. RMSD values are generally higher compared to the full protein with both mutant SPN domains exhibiting markedly increased conformational dynamics. (D) Restriction of C_α backbone RMSD analysis to the ARR domain shows a similar yet less pronounced increase of conformational dynamics in both mutants compared to the WT. As both mutation sites are localized distally in the SPN domain and both domains were split, this increase might reflect mutation-induced alterations of the SPN:ARR domain interface. (E) Frame overlays of each trajectory (every fifth frame loaded, overlay [beginning:step:end] = 0:20:20002 resulting in 1000 images) are shown to visualize the dynamics of both domains.

2.2 Cellular impact of the R12C and L68P mutation

The following presented data has been partially published in (Bucher et al., 2021). Immunostainings, image acquisition and analysis of fixed samples was done with the help of Yuhao Han (ZMNH, UKE Hamburg). Mass spectrometry data analysis was done with the help of Jasper Grendel (ZMNH, UKE Hamburg).

Different mechanisms of how individual missense mutations might be linked to pathological conditions have already been discussed in the literature including changes in protein stability, perturbed protein interactions or altered (sub)cellular localization (Stefl et al., 2013). Usually, however, such mechanisms are investigated independently resulting in a paucity of data linking these processes with each other. The previous section provided detailed insight into several molecular defects related to the structure, folding and dynamics of SHANK3 elicited by the presence of the autism-associated missense mutations R12C and L68P. Among others, mutation-induced structural destabilizations, partial unfolding or altered molecular dynamics represent an initial breaking point for further downstream processes. Consequently, in this section, the morphological and functional relevance of these mutations as well as their impact on biochemical signal integration and transmission will be highlighted.

2.2.1 Localization of WT and mutant SHANK3 in neurons

To investigate the pathogenic role of the R12C and L68P mutation in a cellular context, initial immunocytochemical labeling of the synaptic proteins homer, bassoon and SHANK3 was conducted to establish their basal colocalization (Fig 18A-B). Thereby, homer serves as general excitatory postsynaptic and bassoon as presynaptic marker. As expected, SHANK3 nearly quantitatively colocalized with homer (~93%) whereas only ~72% of homer-positive spines colocalized with SHANK3 (Fig. 18C). Approximately 80% of all detected SHANK3 puncta were also positive for bassoon and are thus considered to have a presynaptic contact (Fig. 18C). To subsequently characterize whether SHANK3 mutants alter the spine density or cause an intracellular redistribution, GFP-tagged WT or mutant full-length (FL) SHANK3 was overexpressed in primary hippocampal rat neurons. Notably, SHANK3 has been established as important general regulator of dendritic spine morphology, number and maintenance since overexpression of SHANK3 was previously shown to alter the number and function of spines in hippocampal neurons (Durand et al., 2012; Han et al., 2013). Furthermore, expression of SHANK3 was demonstrated to be sufficient to induce functional dendritic spines in aspiny neurons corroborating the central role of SHANK3 in spinogenesis (Roussignol et al., 2005). Consequently, the overexpression of GFP-SHANK3[FL] variants in primary hippocampal rat neurons was limited to 16-18 hours to avoid dosage-dependent artefacts. Under these conditions, however, the mutations did not alter the dendritic spine density compared to overexpressed WT SHANK3 or a corresponding GFP control (Fig. 19A). In contrast, neurons overexpressing the L68P mutant showed a significantly increased cluster formation tendency in the dendritic shaft compared to the WT or a GFP control (Fig. 19B). Although the R12C mutant followed the same trend, no significant increase was observed in this case.
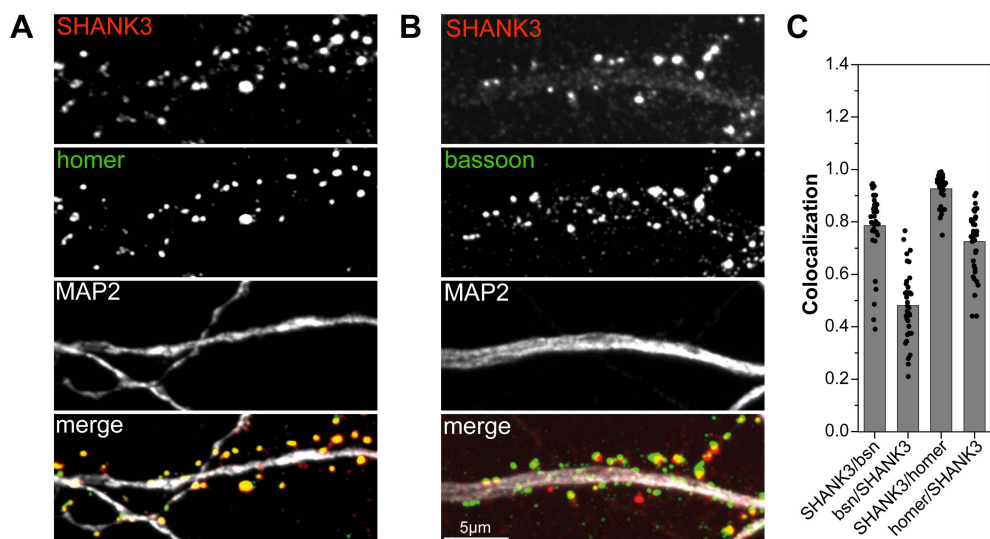
Figure 18: Colocalization of endogenous SHANK3 with homer and bassoon in dendritic spines

(A) Representative images of immunostained endogenous SHANK3 (red), homer (green) and MAP2 (gray) in primary hippocampal rat neurons (DIV14 - 16) are shown. (B) Representative images of immunostained endogenous SHANK3 (red), bassoon (bsn; green) and MAP2 (gray) are shown. (C) The colocalization of SHANK3/homer and homer/SHANK3 as well as SHANK3/bsn and bsn/SHANK3 was quantified from a total of 36 cells from two independent cultures. Individual data points (one data point per cell) as well as bars representing the mean are shown. While ~72% of homer puncta colocalize with SHANK3, ~93% of SHANK3 puncta co-localize with homer. Furthermore, ~79% of SHANK3-positive spines exhibit a pre-synaptic contact measured by the colocalization with bsn.

These results raise the question, whether the mutants may lead to alterations in the amount of SHANK3 present in dendritic spines and shaft. Interestingly, line profile analyses of the GFP-SHANK3^{FL} fluorescence intensity distribution between spines and the dendritic shaft revealed no difference between neurons overexpressing mutant or WT SHANK3 variants (Fig. 19C). Under each condition, spines exhibited approximately a three-fold higher mean fluorescence intensity than the corresponding dendritic shaft, irrespective of the presence of either mutation (Fig. 19C). Collectively, an increased number of dendritic SHANK3 clusters and thus a higher dendritic cluster formation tendency can be observed for the L68P mutant without altering the overall distribution of SHANK3 between spines and the dendritic shaft (Fig. 19D). The same trend is observed for the R12C mutant, yet without statistical significance.

To estimate the functional role of dendritic SHANK3 clusters as well as the corresponding impact of both mutants, the colocalization of overexpressed GFP-tagged WT or mutant SHANK3^{FL} with homer and bassoon was analyzed in the dendritic shaft (Fig. 20A-B). In fact, 48 - 54% of dendritic SHANK3 clusters (WT or mutant) colocalized with the pre-synaptic marker bassoon, implicating that these clusters could partially represent excitatory shaft synapses (Fig. 20C). This is further corroborated by the finding that 32 - 34% of dendritic WT or mutant SHANK3 clusters colocalize with the excitatory post-synaptic marker homer (Fig. 20D). Overall, ASD-associated SHANK3 mutants form higher numbers of dendritic clusters which partially constitute excitatory shaft synapses.
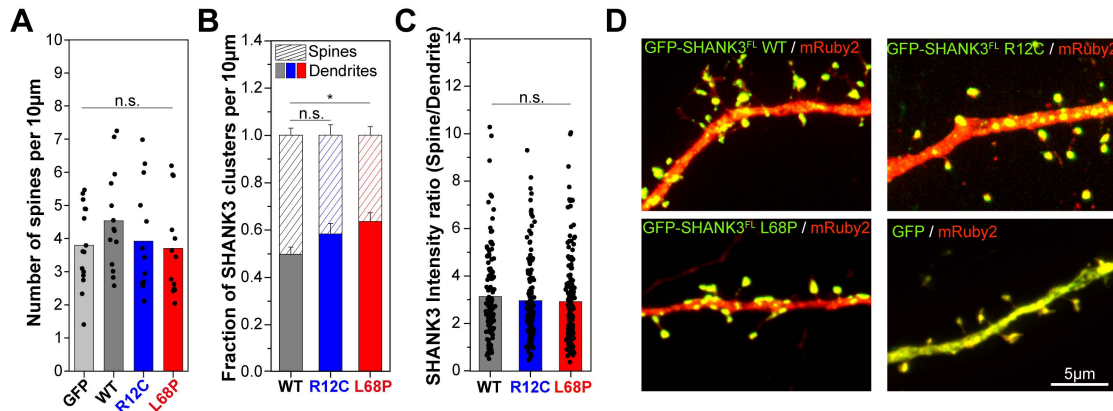
Figure 19: Increased cluster formation tendency of L68P mutant SHANK3 in the dendritic shaft

(A) To analyze the effect of ASD-associated SHANK3 mutants on the spine density, primary rat hippocampal neurons were transiently co-transfected with GFP-SHANK3^{FL} variants (WT, R12C or L68P) and mRuby2 for 16 - 18 hours. The number of spines was counted based on the mRuby2 signal and was normalized to a dendritic length of 10 μm (GFP: 15 cells from four independent cultures, WT: 14 cells from three independent cultures, R12C: 13 cells from four independent cultures, L68P: 13 cells from four independent cultures). Individual data points as well as bars representing the mean are shown. Short-time overexpression of all tested SHANK3 variants had no significant impact on the average spine density (Kruskal-Wallis ANOVA with Dunn's post hoc test: p = 0.59 – 1). (B) The same neurons used in (A) were analyzed for changes in the distribution of mutant SHANK3 clusters in spines and dendrites. While the R12C mutant did not elicit a significant change of the cluster distribution, overexpression of the L68P mutant resulted in a significant increase of dendritic SHANK3 clusters (Kruskal-Wallis ANOVA with Dunn's post hoc test: p(WT/R12C) = 0.42; p(WT/L68P) = 0.04 and p(R12C/L68P) = 0.93 at P = 95%). Bars represent the mean ± SEM. (C) To quantify the fluorescence intensity distribution of SHANK3 variants in spines and dendrites, line profile analyses were performed on primary rat hippocampal neurons transiently co-transfected with GFP-SHANK3^{FL} (WT, R12C or L68P) and mRuby2 for 16 - 18 hours. Peaks of mean gray values corresponding to SHANK3 clusters in the spine head or dendritic shaft were obtained from line profiles covering the entire spine width. From these peak values the SHANK3 intensity ratio was determined (WT: 12 cells from four independent cultures, R12C: 11 cells from four independent cultures, L68P: 12 cells from five independent cultures). Individual data points (one data point per spine) as well as bars representing the mean are depicted. Despite the observed L68P mutant-induced redistribution of SHANK3 clusters between spines and dendrites, no significant change in the mean SHANK3 intensity distribution was found (one-way ANOVA with Bonferroni multiple comparisons test: p(WT/R12C) = 1 and p(WT/L68P) = 0.83 at P = 95%). (D) Representative images of primary rat hippocampal neurons transiently co-transfected with GFP-SHANK3^{FL} variants (WT, R12C or L68P) and mRuby2 for 16 - 18 hours are shown.

Figure 20: Colocalization of overexpressed SHANK3 variants with homer and bassoon in the dendritic shaft

(A) Representative images of primary hippocampal rat neurons (DIV14 - 16) overexpressing GFP-SHANK3^{FL} (WT, R12C or L68P; green) and immunostained for bassoon (bsn; red) and MAP2 (gray) are shown. The shape of analyzed dendrites is shown as white dashed lines and was drawn based on the MAP2 signal. (B) Representative images of GFP-SHANK3^{FL} (WT or mutant; green) overexpressing neurons immunostained for homer (red) and MAP2 (gray) are shown. The MAP2 mask of analyzed dendrites is drawn as white dashed lines. (C) The quantification of the colocalization of SHANK3/bsn and bsn/SHANK3 in the dendritic shaft of transfected and immunostained neurons is shown (WT: n = 11 cells from three independent cultures; R12C: n = 8 cells from three independent cultures; L68P: n = 10 cells from three independent cultures). Individual data points (one data point per cell) as well as bars representing the mean are depicted. Mutants show no significant impact on the colocalization of SHANK3/bsn and bsn/SHANK3 in the dendritic shaft (Kruskal-Wallis ANOVA with Dunn's post hoc test: SHANK3/bsn: p(WT/R12C) = 1; p(WT/L68P) = 1; and p(R12C/L68P) = 1 at P = 95%; bsn/SHANK3: p(WT/R12C) = 1; p(WT/L68P) = 1; and p(R12C/L68P) = 1 at P = 95%). (D) The colocalization of SHANK3/homer and homer/SHANK3 in the dendritic shaft of transfected and immunostained neurons was quantified (WT: n = 7 cells from two independent cultures; R12C: n = 12 cells from two independent cultures; L68P: n = 11 cells from two independent cultures). Individual data points (one data point per cell) as well as bars representing the mean are depicted. No significant impact of the mutants on the colocalization of SHANK3/homer and homer/SHANK3 in the dendritic shaft are found (Kruskal-Wallis ANOVA with Dunn's post hoc test: SHANK3/homer: p(WT/R12C) = 1; p(WT/L68P) = 1; and p(R12C/L68P) = 1 at P = 95%; homer/SHANK3: p(WT/R12C) = 1; p(WT/L68P) = 1; and p(R12C/L68P) = 1 at P = 95%).

2.2.2 The protein turnover of ASD-associated SHANK3 mutants and cortactin is altered in dendritic spines

To address not only steady-state differences between WT and mutant SHANK3 in a cellular context, but also the influence of these mutations on cellular protein dynamics, fluorescence recovery after photobleaching (FRAP) was utilized as a readout together with pharmacological stimulation of neuronal activity in primary hippocampal rat neurons. Additionally, the diffusion of the established SHANK3 interaction partners cortactin and homer1 (Macgillavry et al., 2016; Naisbitt et al., 1999; Tu et al., 1999) was investigated by FRAP to answer the question whether ASD-associated SHANK3 mutations could further alter the dynamics of interacting proteins in a cellular context.

To initially probe the dynamics of SHANK3 itself, GFP-SHANK3^{FL} variants (WT or mutant) were overexpressed for less than 24 hours and subsequently photobleached in individual dendritic spines (Fig. 21A). Thereby, the activity-dependence of GFP-SHANK3^{FL} diffusion in dendritic spines was studied by stimulation of corresponding primary hippocampal rat neuron cultures with (+)-Bicuculline, acting as inhibitor of GABA$_A$ receptors resulting in a disinhibition of excitatory neurotransmission (Nowak et al., 1982). Surprisingly, both mutations had clearly distinct effects not only on a structural but also on a cellular level since the protein dynamics of L68P mutant SHANK3 in dendritic spines was indistinguishable from the WT while the R12C mutation resulted in a significant increase in the mobile protein fraction (Fig. 21A and D). This increased mobility or reduced residing time of the R12C mutant in dendritic spines suggests that structural perturbations cannot directly be translated to the level of cellular protein dynamics since this mutation was generally observed to result in less severe structural perturbations compared to the L68P mutant. On the other hand, WT and mutant SHANK3 variants responded identically to a (+)-Bicuculline mediated increase of neuronal activity, which caused a general reduction of the mobile fraction corresponding to activity-induced immobilization of SHANK3 in the PSD (Grabrucker, 2014; Fig. 21D).

FRAP experiments in neurons expressing not only GFP-SHANK3^{FL} variants but also distinct known interaction partners further demonstrated that the complexity and individuality of mutation-induced perturbations extends to the level of SHANK3 interaction partners. Notably, the cortactin and homer1 binding sites on SHANK3 are both located within the proline-rich domain and are therefore expected to be similarly affected by the mutations. Strikingly, only the mobility of cortactin, but not of homer1, was significantly altered by the L68P mutation, while the R12C mutation had no significant impact on the dynamics of both proteins (Fig. 21E-F). This differential effect might partially arise from the influence of different synaptic homer1 and cortactin interaction partners on their respective dynamics. While homer1 might be stronger anchored to the PSD by interaction with other scaffolding proteins, cortactin has been shown to depend on the interaction with SHANK3 to control F-actin turnover in dendritic spines (Macgillavry et al., 2016). Additionally, the mutated residues within the SPN domain are separated by more than thousand amino acids from the homer1 and cortactin binding sites demonstrating not only a differential but also considerably long-ranged effect on the dynamics of cortactin.
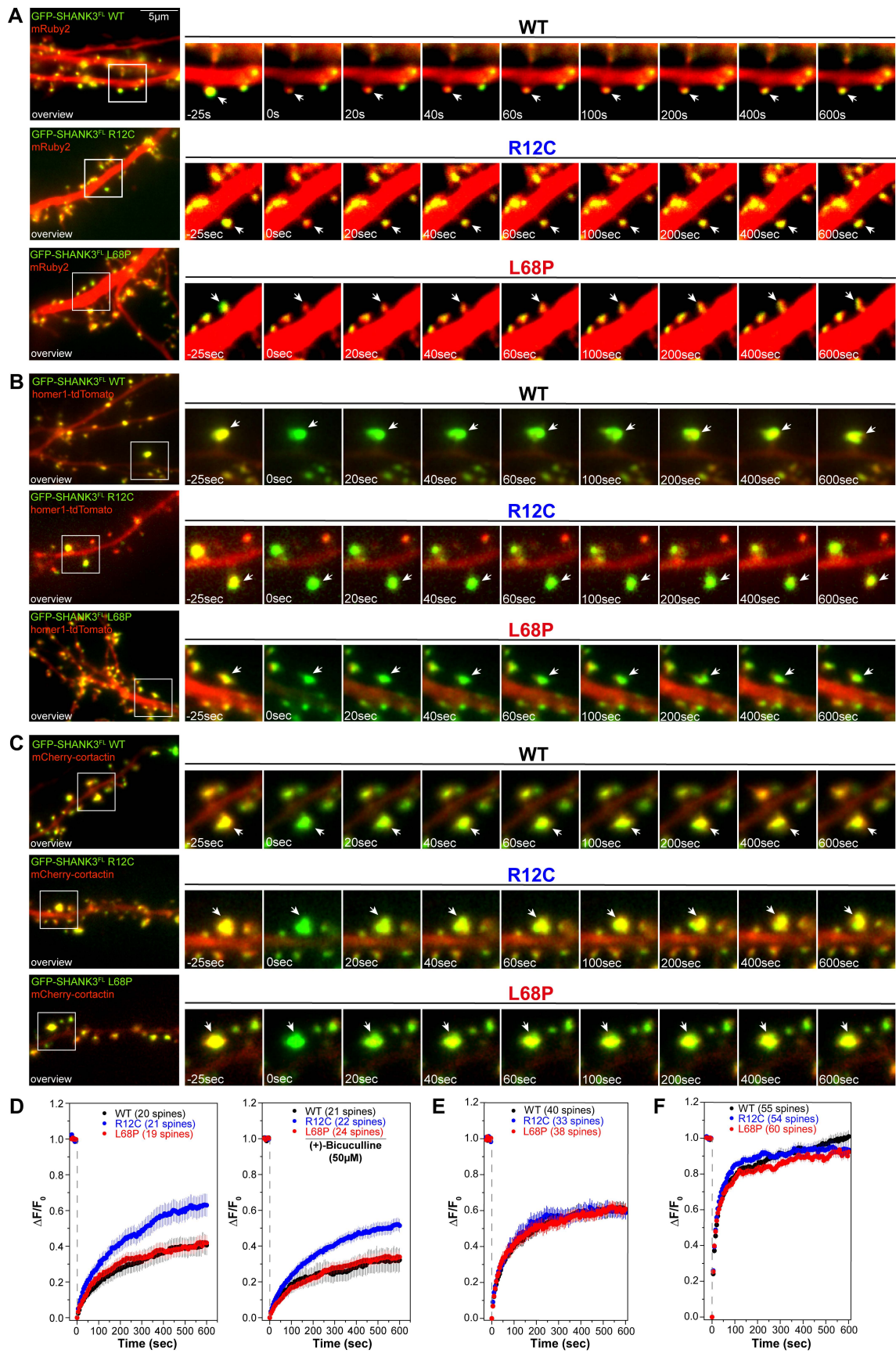
Figure 21: Impact of ASD-associated SHANK3 mutations on the protein residing time in spines and dynamics of interaction partners

(A) Representative overview images of primary rat hippocampal neurons (DIV14 -16) which were transiently co-transfected with GFP-SHANK3[FL] (WT, R12C or L68P) and mRuby2 are shown (left). Photobleaching of GFP-SHANK3[FL] in selected spines was achieved with a 488 nm laser and is demonstrated in corresponding zoomed images at individual timepoints during FRAP. (B) Representative overview images (left) of neurons transiently co-transfected with GFP-SHANK3[FL] variants and homer1-tdTomato as well as detailed images from selected photobleached spines at individual timepoints are shown. The effect of SHANK3 mutants on the dynamics of homer1 in spines was measured by photobleaching of homer1-tdTomato with a 561 nm laser. (C) Representative overview images of neurons, which were transiently co-transfected with GFP-SHANK3[FL] variants and mCherry-cortactin are shown (left). The effect of SHANK3 mutants on the dynamics of cortactin in spines was measured by photobleaching of mCherry-cortactin with a 561 nm laser. Zoomed images of selected photobleached spines at individual timepoints are shown. (D) FRAP curves of WT and mutant GFP-SHANK3[FL] show that the R12C but not the L68P mutant exhibits an increased recovery and therefore a reduced residing time in spines (Kruskal-Wallis ANOVA with Dunn's post hoc test; untreated: $p(WT/R12C) < 0.0001$, $p(R12C/L68P) < 0.0001$, and $p(WT/L68P) = 1$). To analyze the activity dependence of GFP-SHANK3[FL] diffusion in spines, neurons were treated with 50 µM (+)-Bicucullin for 5 min at 37 °C and 5% CO_2 prior to photobleaching. All tested variants show a slightly and equally reduced recovery after pharmacological treatment (Kruskal-Wallis ANOVA with Dunn's post hoc test; bic: $p(WT/R12C) < 0.0001$, $p(R12C/L68P) < 0.0001$, and $p(WT/L68P) = 1$). Data was obtained from three independent cultures for the untreated group and from two independent cultures for the (+)-Bicucullin stimulated group. (E) FRAP curves of homer1-tdTomato show that the presence of different GFP-SHANK3[FL] variants has no effect on the recovery of homer1 (Kruskal-Wallis ANOVA with Dunn's post hoc test; $p(WT/R12C) = 1$, $p(R12C/L68P) = 1$, and $p(WT/L68P) = 1$). (F) FRAP curves of cortactin-mCherry reveal that the presence of mutant GFP-SHANK3[FL] variants alters the recovery of their interaction partner cortactin. The presence of L68P mutant SHANK3 results in a significant reduction of the mobile fraction of cortactin in spines (Kruskal-Wallis ANOVA with Dunn's post hoc test; $p(WT/R12C) = 1$, $p(R12C/L68P) = 0.0002$, and $p(WT/L68P) = 0.0007$).

These mutation-induced differences in cellular protein dynamics raise the question if neuronal protein turnover might be impacted on a wider range related to *de novo* protein synthesis and degradation. Pulldown experiments from HEK293 cells overexpressing AviTag-GFP-SHANK3[(1-676)] variants (WT, R12C or L68P) as well as HA-Ubiquitin showed a strongly enhanced ubiquitination of mutant SHANK3-associated protein complexes suggesting an increased targeting for proteasomal degradation (Fig. 22A). However, no differences in *de novo* protein synthesis were evident in dendritic spines, measured by fluorescence non-canonical amino acid tagging (FUNCAT) of the newly synthesized protein pool (Fig. 22B-C). As an internal control for this experiment, neurons were silenced with tetrodotoxin (TTX) and D-(-)-2-amino-5-phosphonopentanoic acid (D-APV) before the incorporation of unnatural amino acids for FUNCAT since the activity-dependence of neuronal protein translation is well established (Ebert & Greenberg, 2013). As expected, neuronal silencing significantly reduced *de novo* protein synthesis in all groups indicating that the tested SHANK3 mutations indeed have no effect on this process (Fig. 22B-C). Overall, ASD-associated SHANK3 missense mutations were shown to impact the protein residing time of SHANK3 and cortactin in dendritic spines and are likely to induce increased proteasomal degradation of SHANK3-associated complexes via enhanced ubiquitination.
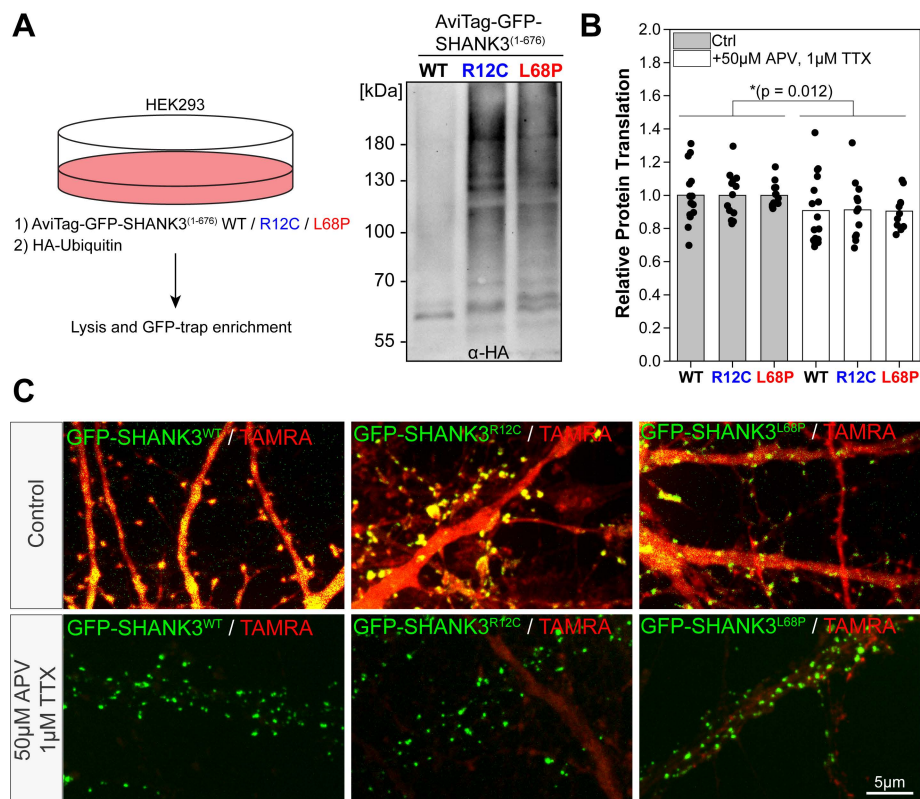
Figure 22: Influence of SHANK3 mutants on protein synthesis and degradation
(A) The ubiquitination of SHANK3-associated protein complexes was analyzed by GFP-trap (Chromotek) pulldown from HEK293 cells, which were transiently co-transfected with AviTag-GFP-SHANK3$^{(1-676)}$ (WT, R12C or L68P) and HA-ubiquitin. Enriched protein complexes were analyzed by western blotting. Complexes enriched with mutant SHANK3 variants show strongly increased ubiquitination compared to the WT. (B) *De novo* protein synthesis in dendritic spines was quantified by FUNCAT in primary rat hippocampal neurons. Neurons (DIV14-16) were transiently transfected with GFP-SHANK3^{FL} (WT, R12C or L68P) for 16-18 hours and subsequently cultured in the presence of L-azidohomoalanine (AHA). Labeling of *de novo* synthesized proteins, which incorporated AHA was performed by Cu(I)-catalyzed azide-alkyne click reaction (CuAAC) with tetramethylrhodamine (TAMRA) alkyne. Neurons were immunostained for homer to facilitate spine detection (data not shown). In spines with detected colocalization of homer and GFP-SHANK3^{FL}, the TAMRA intensity was measured and normalized to the TAMRA-signal in spines without GFP-SHANK3^{FL} to determine the effect of the presence of GFP-SHANK3^{FL} variants on *de novo* protein synthesis (i.e. relative protein translation). The activity dependence of *de novo* protein synthesis was measured by silencing neurons with 1 μM tetrodotoxin (TTX) and 50 μM D-(-)-2-amino-5-phosphonopentanoic acid (D-APV) prior to CuAAC. Individual data points (one data point per cell) as well as bars representing the mean are shown (Ctrl: WT = 14 cells, R12C = 13 cells, L68P = 13 cells; treatment: WT = 16 cells, R12C = 12 cells, L68P = 11 cells; three independent cultures). As expected, neuronal silencing resulted in a significant reduction in relative protein translation, but the presence of mutant GFP-SHANK3^{FL} variants had no effect (two-way ANOVA with Tukey post hoc test, p = 0.012 for treatment, p = 0.529 for genotype, P=95%). (C) Representative images of transfected and labeled neurons of the control group as well as the TTX- and D-APV - treated group are shown.

2.2.3 Investigation of mutation-induced gain- and loss-of-function for SHANK3 binding partners

Previous experiments have demonstrated that ASD-associated SHANK3 missense mutations are able to selectively and distinctively alter the dynamics of individual interaction partners in living primary hippocampal rat neurons. It is unclear, however, whether this effect is a direct result of mutation-induced altered PPIs or originates from other structures and processes such as F-actin based physical diffusion barriers in dendritic spines. Notably, the interplay between molecular interactions and physical diffusion barriers to regulate diffusional mobility in dendritic spines is currently not fully understood yet but is generally thought to have important implications for synaptic function (Obashi et al., 2021). Consequently, the R12C and L68P mutant were tested for potential differences in binding to the known interaction partners homer1, cortactin and SAPAP1 using co-immunoprecipitation (co-IP) assays from HEK293 cells (Boeckers et al., 1999; Naisbitt et al., 1999; Tu et al., 1999). Surprisingly, none of the tested proteins showed a differential interaction with one of the mutants (Bucher et al., 2021). Nonetheless, changes in the interactome of mutant SHANK3 variants cannot be excluded by this analysis. These results, however, suggest that other processes or mechanisms are likely to alter the mobility of cortactin in dendritic spines in the presence of L68P mutant SHANK3. Furthermore, a direct dependence of protein mobility on the molecular interaction with mutant SHANK3 may still exist for other proteins, which were not tested here.

Despite the finding that the tested ASD-associated SHANK3 mutations do not seem to result in a loss of binding to the known interaction partners cortactin, homer1 and SAPAP1, previous studies already identified changes in the composition of isolated PSDs from *Shank3* knock-out mice by proteomic analysis (Reim et al., 2017). This suggests that disturbances in the interactomes of mutant SHANK3 variants are indeed likely to exist and might have been missed by preceding experiments due to the limited coverage of protein targets. Consequently, mass spectrometry-based screening was performed to identify R12C and L68P mutation-induced gain- or loss-of-function of SHANK3 protein interactions. Therefore, AviTag-GFP-SHANK3$^{(1-676)}$ variants (WT and mutant) were pre-purified from transiently transfected HEK293 cells and used as bait for subsequent enrichment of WT and mutant SHANK3-associated protein complexes from rat brain lysates. Enriched complexes were separated by SDS-PAGE and subjected to shotgun mass spectrometry analysis to identify and characterize differences between the corresponding interactomes (Fig. 23A). Thereby, functional gene ontology (GO)-term enrichment analysis identified several altered biological processes related to kinase- and phosphatase-activity, cytoskeletal protein binding or protein-containing complex binding, demonstrating wide-ranging effects of both mutations on diverse intracellular processes (Fig. 23B). Changes in the enrichment of GO-terms related to ion binding might further be a consequence of mutation-induced structural perturbations. To specifically visualize mutation-induced changes in known protein complexes, proteins which were identified by mass spectrometry were initially clustered using the database for annotation, visualization and integrated discovery (DAVID). Mutation-induced changes in the interactomes of mutant AviTag-GFP-SHANK3$^{(1-676)}$ affect kinase- and microtubule-associated protein complexes among others (Fig. 23C). Furthermore, an increased abundance of a pre-synaptic active zone-associated protein complex might indicate trans-synaptic effects of both mutations (Fig. 23C). A more detailed analysis highlighted that identified proteins showed both increased and decreased abundancies in mutant

AviTag-GFP-SHANK3$^{(1-676)}$ associated complexes without a clear tendency in either direction, suggesting the presence of gain- and loss-of-function mechanisms depending on the individual interaction partner (Fig. 23D).
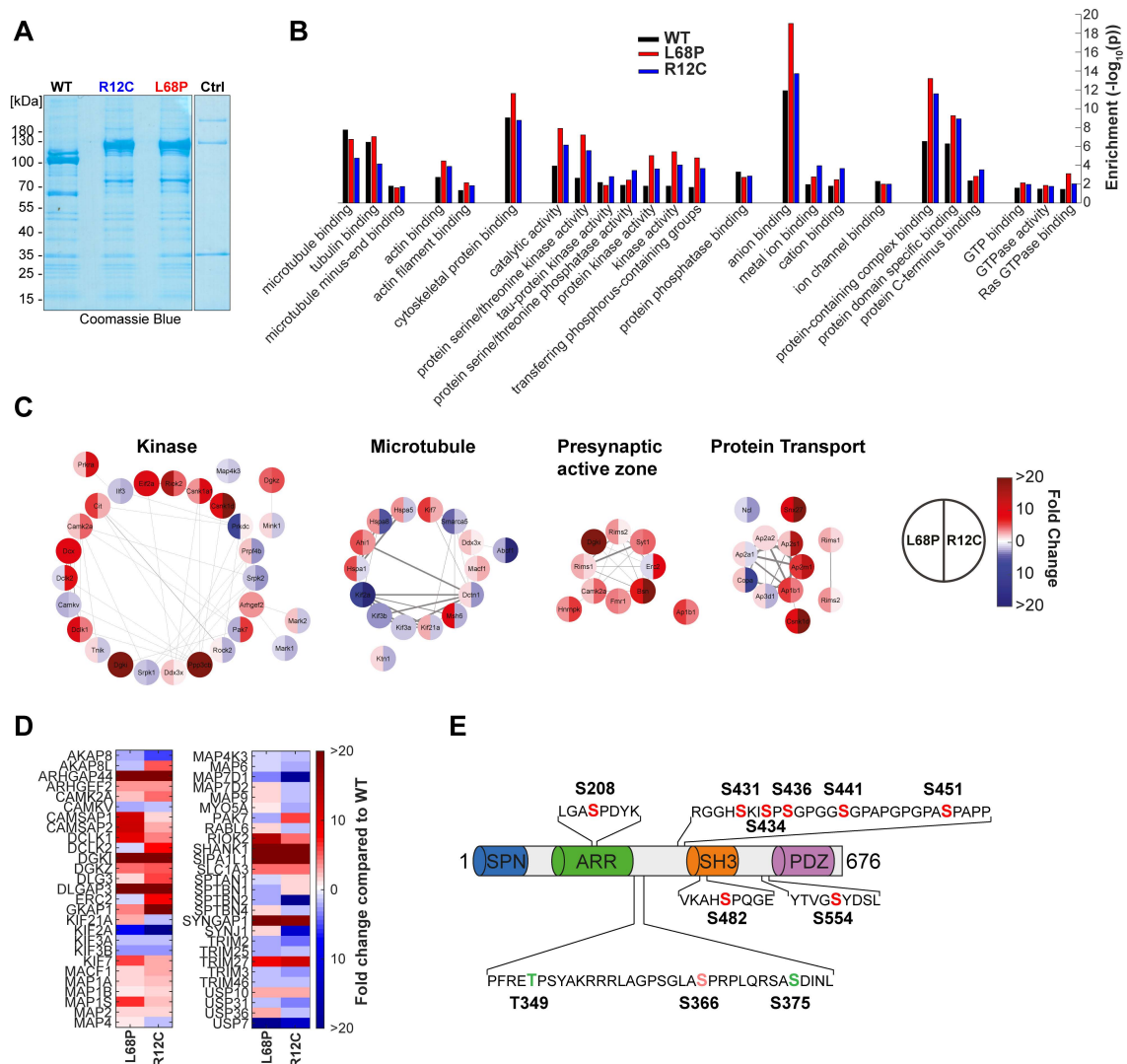
Figure 23: Gain- and loss-of-function in the synaptic interactome of SHANK3 mutants

(A) AviTag-GFP-SHANK3$^{(1-676)}$ variants (WT, R12C and L68P) as well as an AviTag-GFP control protein were overexpressed and purified from HEK293 cells and used as bait for subsequent pulldowns from rat brain lysates. Individual pulldown samples were separated by SDS-PAGE and stained with Coomassie brilliant blue. For mass spectrometric analyses, peptide mixtures were obtained by in-gel digestion of proteins with trypsin and subsequent extraction from the gel. (B) Functional GO-term enrichment analysis of identified proteins from the corresponding WT, R12C and L68P pulldowns using the database STRING. A selection of individual GO-terms is shown. (C) Individual DAVID-clusters of identified proteins were selected and known protein:protein interactions were visualized with Cytoscape. Proteins are shown as filled circles, color-coded for the mutation-induced change in protein abundance relative to the WT based on summed peptide intensities. (D) A selection of identified up- and downregulated proteins is shown for the R12C and L68P mutation. Color coding is based on summed peptide intensities, normalized to WT protein levels. (E) Analysis of post-translational protein modifications revealed that R12C and L68P mutant AviTag-GFP-SHANK3$^{(1-676)}$ proteins are hyperphosphorylated. Phosphosites identified only in the mutants but not in the WT are highlighted in red within corresponding sequence stretches. Residues phosphorylated exclusively in the WT protein are marked in green. Additionally, pS366 has been identified both in the WT and mutant proteins.

Among others, several SHANK3 interaction partners and proteins which have previously been associated with the development of ASD such as SynGAP or CaMKII were identified and affected by the mutations (Fig. 23D; Gamache et al., 2020; Sakai et al., 2011; Stephenson et al., 2017). Finally, analysis of post-translational modifications of SHANK3 showed that both ASD-associated mutations induced a massive increase in phosphorylation (Fig. 23E). While only 3 phosphosites could be identified in the WT protein, 9 phosphorylated residues were found in mutant SHANK3 variants from which one represents a shared site (pS366; Fig. 23E). Taken together, the R12C and L68P mutation were shown to elicit a profound restructuring of the corresponding interactomes affecting a multitude of different biological processes.

Individual proteins, which were shown to be affected by the SHANK3 mutations, such as SynGAP or CaMKII represent interesting hits for follow-up experiments to explore novel mechanisms and signaling pathways in pyramidal neurons relevant for the development of ASD. SynGAP, which displayed a strongly increased presence in mutant SHANK3-associated protein complexes, was characterized as important regulator of biochemical signal transduction and synaptic plasticity in previous studies and acts as GTPase-activating protein (GAP) in dendritic spines (Fig. 23D; Gamache et al., 2020). Importantly, mutations in the *SYNGAP1* gene have been previously associated with ID as well as ASD and schizophrenia (Creson et al., 2019; Gamache et al., 2020). On the other hand, direct binding of active, autophosphorylated CaMKIIα to a tribasic motif in SHANK3 corresponding to residues 949-951 has been shown recently (Perfitt et al., 2020). Consequently, CaMKII enrichment in AviTag-GFP-SHANK3[(1-676)] associated complexes is likely resulting from either indirect binding via oligomerization of AviTag-GFP-SHANK3[(1-676)] variants with endogenous full-length SHANK3 or via other endogenous interaction partners. Nonetheless, a direct binding to other motifs, which have not yet been identified, cannot be excluded. Finally, CaMKII-dependent phosphorylation of SynGAP was demonstrated as important mechanism to trigger AMPAR insertion and spine enlargement during LTP (Araki et al., 2015). Therefore, SHANK3 might constitute an important regulatory component within the SynGAP-CaMKII signaling complex. Importantly, the proteomic analysis of SHANK3-associated protein complexes provides no information whether an identified protein directly binds to SHANK3 or rather represents an integral part of a complex without direct interaction. Therefore, individual mass spectrometry hits must be validated by independent experiments.

Here, the interaction of different GFP-tagged SHANK3 variants (1-676 and FL; WT, R12C and L68P) with SynGAP and CaMKII was probed by several pulldown experiments. Consistent with mass spectrometry data, both mutants indeed showed a strong increase in SynGAP signals of corresponding western blots of pulldown samples obtained from AviTag-GFP-SHANK3[(1-676)] variants (Fig. 24A). Due to the identified hyperphosphorylation of ASD-associated SHANK3 mutants, the dependency of this interaction on the phosphorylation-state of SHANK3 was additionally probed by performing pulldown experiments in the presence of phosphatase-inhibitors. This, however, did not alter the previously observed pattern of increased SynGAP signals for both mutants (Fig. 24B). As an internal control in both pulldown experiments, corresponding western blots were additionally tested for CaMKIIα, which should not yield a signal as the binding site is not present within SHANK3[(1-676)]. Surprisingly, signals were obtained for the WT but not mutant SHANK3 variants, although at a molecular weight, which might rather correspond to CaMKIIβ instead of CaMKIIα (Fig. 24A-B).
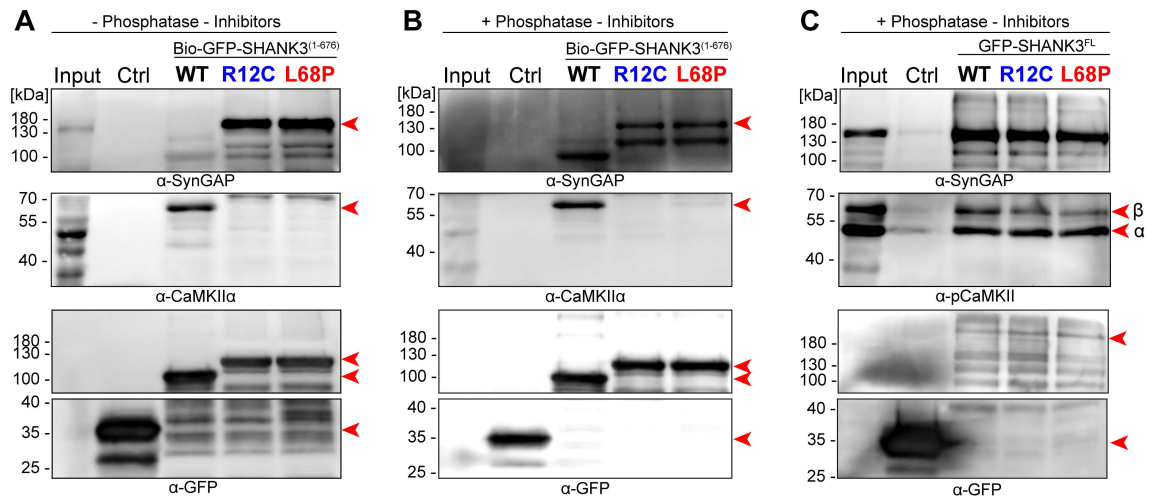
Figure 24: Differential interaction of SHANK3$^{(1-676)}$ and FL variants with SynGAP and CaMKII
To analyze potential mutation-induced differences in the interaction of SHANK3 variants with SynGAP and CaMKII, either AviTag-GFP-SHANK3$^{(1-676)}$ (WT, R12C, L68P) or GFP-SHANK3^{FL} were overexpressed in HEK293 cells. Following an initial purification step of recombinant SHANK3 variants from HEK293 cells using either GFP-trap (Chromotek) or magnetic Biotin/Streptavidin beads (Thermo Fisher), pulldowns were performed from rat brain lysates. (A) Obtained protein complexes were analyzed by western blotting. Consistent with mass spectrometry data, AviTag-GFP-SHANK3$^{(1-676)}$ R12C and L68P associated complexes exhibit a strong enrichment of SynGAP. As expected, no binding of CaMKIIα to AviTag-GFP-SHANK3$^{(1-676)}$ is found as the binding site on SHANK3 was previously mapped to residues 949-951 (Perfitt et al., 2020). The (potentially unspecific) signal found for the WT might arise from CaMKIIβ. Western blots with GFP detection show the individual protein amounts loaded. Relevant bands are marked with red arrowheads. (B) To probe whether the interaction with SynGAP might be regulated by phosphorylation, pulldowns described in (A) were repeated in the presence of a phosphatase inhibitor cocktail. Overall, no significant differences could be detected and both mutants show increased interaction with SynGAP. Additionally, under these conditions AviTag-GFP-SHANK3$^{(1-676)}$ (WT, R12C, L68P) seems to be unspecifically detected by the SynGAP antibody. (C) Independently, the interaction of WT and mutant GFP-SHANK3^{FL} variants with SynGAP and pCaMKII was tested in the presence of phosphatase inhibitors. For SynGAP, no difference in binding to WT or mutant GFP-SHANK3^{FL} could be detected under these conditions. Interestingly, both mutants specifically showed reduced binding to pCaMKIIβ (upper band) but not pCaMKIIα (lower band).

This was independently verified in pulldowns using GFP-SHANK3^{FL} variants, where western blots probed with a pCaMKII antibody showed that the WT interacts with both CaMKIIα and CaMKIIβ, while the mutants showed reduced signals only for CaMKIIβ (Fig. 24C). As peptides identified by mass spectrometry might be misassigned to the canonical proteoform by MaxQuant in individual cases if no specific peptides corresponding exclusively to a different isoform are identifiable, the presence of CaMKIIβ in WT and mutant SHANK3-associated protein complexes cannot be excluded. As CaMKIIβ has been shown to play an important non-enzymatic role by recruiting CaMKIIα to dendritic spines in the hippocampus as well as by exerting F-actin bundling activity, the interaction with SHANK3 might represent a novel regulatory hub, which will be followed up in future experiments (Borgesius et al., 2011; Wang, Chen et al., 2019).

Besides, no differential interaction of mutant SHANK3[FL] variants with SynGAP was observed anymore suggesting a potential SHANK3 isoform- specificity for this interaction (Fig. 24C). Collectively, both gain- and loss-of-function was observed for the binding of SHANK3 mutants to various interaction partners. Several SHANK3 interactors were identified with a particular focus on the SynGAP-SHANK3-CaMKII signaling complex, which might constitute a biochemical signaling entity relevant for the development of ASD.

2.3 Characterization of an L68P knock-in mouse as a model for ASD

The L68P knock-in mouse model was originally created in the lab of Prof. Eunjoon Kim (Korea Advanced Institute of Science and Technology, KAIST, Daejeon, South Korea) and was transferred to the ZMNH. Analysis of excitatory and inhibitory synaptic markers was performed with the help of Julia Bär (Institute of Biology, HU Berlin). STED imaging was conducted with help of Prof. Marina Mikhaylova (Institute of Biology, HU Berlin). Electrophysiological recordings were performed by Tomas Fanutza (ZMNH, Hamburg).

While the R12C mutation was previously rather seen as an ASD risk factor, the L68P mutation was suggested to be causative for the development of ASD (Durand et al., 2007; Gauthier et al., 2009). This is consistent with the results outlined here, which revealed generally more severe structural impairments of the L68P mutation related to partial unfolding and reduced structural stability on multiple levels as well as cellular consequences, which were not observed for the R12C mutation such as an increased dendritic cluster formation tendency. For this reason, a humanized mouse model of ASD was generated carrying the L68P mutation as a knock-in to study the cellular and network impact of this mutation under more physiological conditions. Hence, in this final section a preliminary characterization of the SHANK3 L68P knock-in mouse model is presented.

2.3.1 Genetic characterization of the L68P knock-in

The *SHANK3* L68P knock-in mouse line was originally generated from B6/N embryonal stem cells, where the endogenous mouse *Shank3* gene was replaced by the human *SHANK3* gene carrying the L68P mutation. Despite existing differences in the DNA sequence of the corresponding human and mouse gene, their principal intron-exon structure is very similar (Fig. 25A).
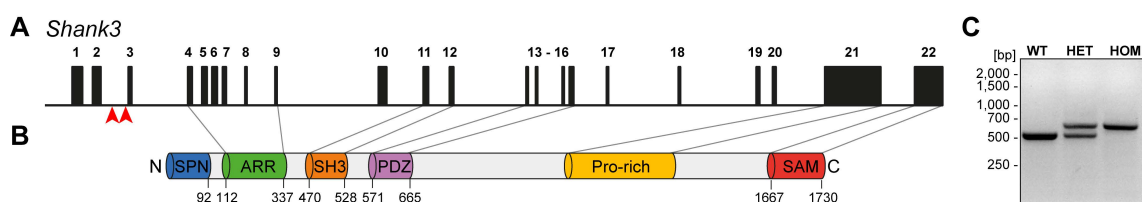
Figure 25: Genotyping of an ASD mouse model carrying a human *SHANK3*[L68P] knock-in
(A) The principal exon-intron gene structure of the mouse *Shank3* gene is shown, which contains 22 coding exons consistent with the human *SHANK3* gene. The binding sites for genotyping primers correspond to an intronic region located between exon 2 and 3 and are marked with red arrowheads. (B) The domain organization of the (full-length) mouse SHANK3 protein is depicted. Individual domains are linked to their corresponding exons on the *Shank3* gene structure scheme. (C) A representative agarose gel is shown for PCR-based genotyping of wild-type (WT), heterozygous (HET) and homozygous (HOM) mice using tail biopsies.

Interestingly, major sequence differences exist only on a DNA level, but not on a protein level as the mouse and human SHANK3 protein exhibit a sequence identity of 95.4% and harbor the same number, type and order of domains (Fig. 25B). Transgenic mice were subsequently backcrossed to a C57BL6/J background and are genotyped from tail biopsies by PCR using primers, which are binding to an intronic region between exon 2 and 3 (Fig. 25A and C). Thereby genotypes can be differentiated as the amplified fragment size of this region differs between the mouse and human gene variant resulting in a 508 bp band for WT mice and a 658 bp band for homozygous knock-in mice carrying two gene copies of the human *SHANK3* gene with the L68P mutation incorporated (Fig. 25C). Heterozygous knock-in mice therefore give rise to both diagnostic fragments as they carry one mouse and one human gene variant (Fig. 25C).

2.3.2 Characterization of hippocampal primary neurons derived from L68P mice: focus on synapses

It was demonstrated above that R12C or L68P mutant SHANK3 have no significant impact on the spine density of hippocampal primary neurons derived from rat embryos if the overexpression is limited to less than 24 hours. However, previous studies showed that overexpression of GFP-SHANK3[R12C] in hippocampal primary neurons indeed leads to reduced spine density (Durand et al., 2012). On the other hand, SHANK3[L68P] overexpressed for five days was reported to have no effect on spine density compared to the WT (Mameza et al., 2013). Due to these inconclusive results, the spine density of hippocampal primary neurons derived from L68P knock-in mice, which express endogenous levels of the SHANK3 protein, was analyzed to clarify the corresponding impact of the L68P mutation. Therefore, mature neurons (DIV 14-16) were stained for homer1 and gephyrin as excitatory and inhibitory markers, respectively. Strikingly, neurons from *Shank3*[+/L68P] as well as *Shank3*[L68P/L68P] mice exhibited a significantly reduced number of excitatory and inhibitory post-synaptic puncta compared to *Shank3*^{+/+} neurons, suggesting that the L68P mutation indeed impairs spinogenesis (Fig. 26A-B). However, excitatory and inhibitory marker puncta seemed to be reduced equally as no change in the corresponding excitatory/inhibitory (E/I) ratio could be observed (Fig. 26C). Notably, these preliminary results were obtained from only one neuronal culture preparation and thus have to be complemented with additional data from other independent cultures to draw reliable conclusions, which is part of ongoing research.

In line with previous data for the L68P mutation outlined in this work related to changes in the structure, stability, interactome or cellular distribution of SHANK3, the hypothesis may be generated that also the organization of SHANK3 at the PSD might be affected.
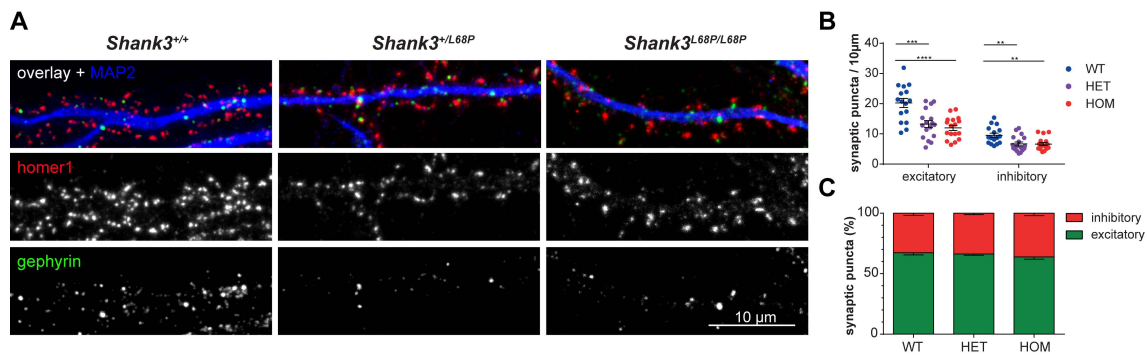
Figure 26: Reduced excitatory and inhibitory post-synaptic puncta in primary hippocampal neurons derived from *SHANK3^L68P* knock-in mice

(A) Representative images of primary hippocampal mouse neurons (DIV14 - 16) derived from either *Shank3^+/+*, *Shank3^+/L68P* or *Shank3^L68P/L68P* knock-in mice are shown. Neurons were immunostained for endogenous homer1 (red), gephyrin (green) and MAP2 (blue). (B) Quantification of excitatory (homer1) and inhibitory (gephyrin) synaptic puncta along ~30 - 70 µm long dendritic stretches of *Shank3^+/+*, *Shank3^+/L68P* and *Shank3^L68P/L68P* neurons (n = 10 cells per group). Individual data points representing synaptic puncta counts per dendrite are shown and are overlaid with the mean ± SEM. Both *Shank3^+/L68P* and *Shank3^L68P/L68P* neurons show a significant reduction in excitatory and inhibitory puncta (one-way ANOVA with Tukey's posthoc test; excitatory: p(*Shank3^+/+*/*Shank3^+/L68P*) < 0.001, p(*Shank3^+/+*/*Shank3^L68P/L68P*) < 0.0001; inhibitory: p(*Shank3^+/+*/*Shank3^+/L68P*) < 0.01, p(*Shank3^+/+*/*Shank3^L68P/L68P*) < 0.01). (C) The excitatory/inhibitory puncta ratio is shown for the quantification in (B). The ratio is not affected by the genotype.

Concerning this matter, it was shown that the nanoscale organization of the PSD constitutes an important factor to regulate synaptic strength and plasticity (MacGillavry et al., 2013). Accordingly, this study highlighted the distribution of scaffold molecules such as PSD-95 or SHANK3 in discrete subsynaptic nanoclusters within the PSD (MacGillavry et al., 2013). To test whether the L68P mutation alters this nanoscale architecture of SHANK3 within the PSD of mouse hippocampal primary neurons, stimulated emission depletion (STED) nanoscopy was performed on neurons, which have been stained for endogenous SHANK3, homer1 and bassoon, respectively. As expected, the nanoscale morphology of SHANK3 clusters in heterozygous or homozygous L68P knock-in neurons was remarkably different compared to WT neurons (Fig. 27). These preliminary results, however, provide no quantitative information on the number and size of mutant SHANK3 nanoclusters as such an analysis requires additional data from independent cultures. Nonetheless, it can be additionally noted that also homer1 displayed an altered nanoscale morphology, which appears to be overall very similar to the organization of SHANK3 (Fig. 27). Independently, transmission electron microscopy (TEM) analysis of excitatory spine synapses in the hippocampal CA1 region revealed a significant reduction of the PSD density, length and thickness in homozygous L68P knock-in mice compared to the WT, corroborating the morphological impairments identified by STED nanoscopy (*data not shown; based on personal communication with Prof. Eunjoon Kim*). Collectively, this data suggests that the L68P mutation critically interferes with spinogenesis and alters the nanoscale organization and overall morphology of the PSD by affecting the distribution of SHANK3 itself as well as its interaction partner homer1.
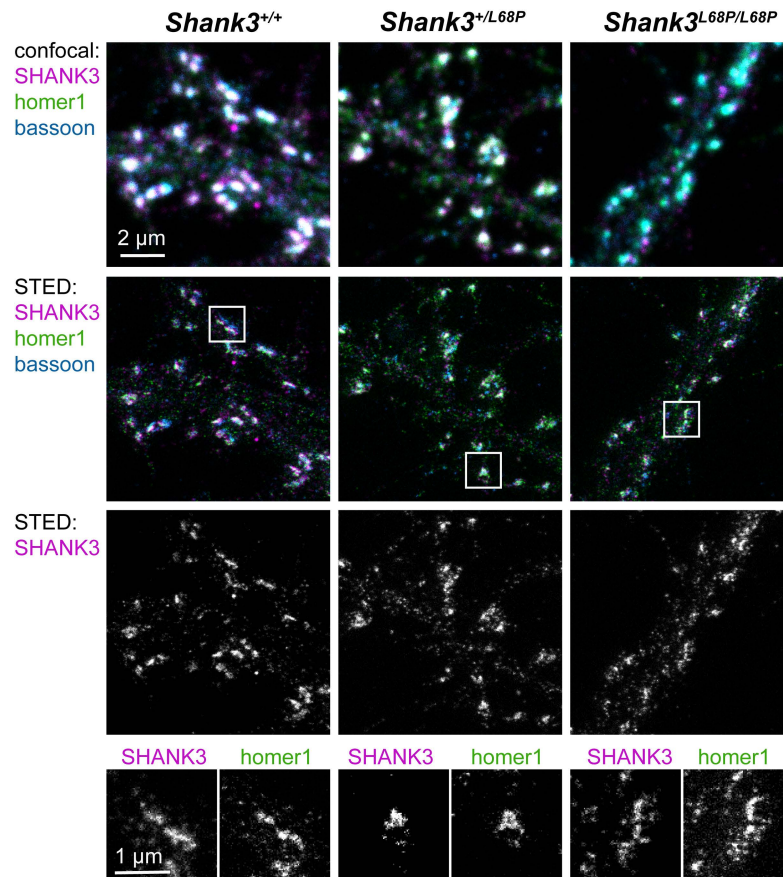
Figure 27: STED imaging of the post-synaptic architecture of L68P mutant SHANK3 nanoclusters

Representative confocal and STED images of primary hippocampal mouse neurons (DIV14 - 16) from *Shank3^{+/+}*, *Shank3^{+/L68P}* and *Shank3^{L68P/L68P}* mice are shown. Neurons were immunostained for endogenous SHANK3 (magenta), homer1 (green) and bassoon (blue). Enlarged regions on the bottom represent individual dendritic spines with altered nanostructural organization and morphology of SHANK3 in L68P mutant neurons. Notably, the nanostructural organization and morphology of homer1 is also altered in mutant neurons.

2.3.3 Electrophysiological characterization of L68P knock-in mice

The L68P mutation was shown to exert a profound impact on the number and morphology of dendritic spines from hippocampal pyramidal neurons, implicating functional consequences. To characterize these functional impairments, electrophysiological field recordings were performed on acute hippocampal slices prepared from 2 - 4 months old male mice. Therefore, I genotyped mice using tail biopsies before handing over individual mice of appropriate sex, age and genotype for blind measurements. In line with the reduced number of excitatory and inhibitory post-synaptic puncta found in primary culture, measurement of field excitatory post-synaptic potentials (fEPSPs) evoked by increasing current injection revealed a reduction of synaptic transmission in slices from heterozygous and homozygous knock-in mice (Fig. 28A). Surprisingly, *Shank3^{L68P/L68P}* mice also showed an increased fiber volley amplitude compared to the WT, suggesting a higher axonal recruitment (Fig. 28B).
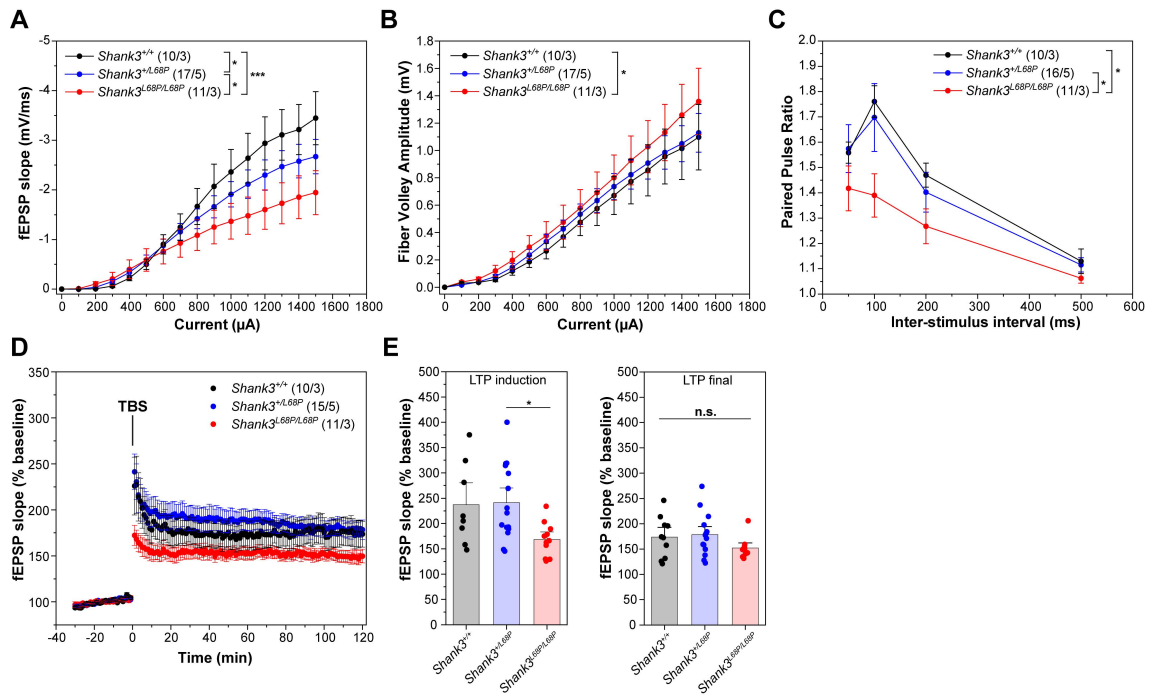
Figure 28: *SHANK3[L68P]* **knock-in mice show reduced synaptic transmission in acute brain slices**

(A) Input-output curves measured on acute slices from either *Shank3^{+/+}*, *Shank3[+/L68P]* or *Shank3[L68P/L68P]* knock-in mice (male, 2 - 4 months old) show an overall reduction of synaptic transmission for both mutant genotypes (two-way repeated measures ANOVA with Tukey posthoc test, * $p < 0.05$, *** $p < 0.0005$). The number of measured slices as well as the number of mice are indicated in parentheses (n slices / n mice). (B) *Shank3[L68P/L68P]* knock-in mice show an overall increase in their fiber volley amplitude suggesting an increased number of activated axons upon stimulation (two-way repeated measures ANOVA with Tukey posthoc test, * $p < 0.05$). The number of measured slices as well as the number of mice are indicated in parentheses (n slices / n mice). (C) Overall, *Shank3[L68P/L68P]* mice show a reduction in the paired pulse ratio (two-way repeated measures ANOVA with Tukey posthoc test, * $p < 0.05$). The number of measured slices as well as the number of mice are indicated in parentheses (n slices / n mice). (D) Long-term potentiation (LTP) was induced by theta burst stimulation (TBS) and was recorded for 120 min. The number of measured slices as well as the number of mice are indicated in parentheses (n slices / n mice). (E) fEPSP slope values were extracted from measured LTP curves directly after induction with TBS (left) as well as after 120 min of LTP (right). While no significant differences between genotypes could be observed after 120 min of LTP, *Shank3[L68P/L68P]* mice exhibit significantly reduced LTP induction compared to *Shank3[+/L68P]* mice (one-way ANOVA with Tukey posthoc test, * $p < 0.05$).

Furthermore, homozygous knock-in mice displayed a reduced paired pulse ratio (PPR) at CA1 Schaffer collateral synapses, suggesting potential short-term plasticity alterations elicited by the L68P mutation (Fig. 28C). As the PPR is generally thought to reflect the pre-synaptic vesicle release probability, these preliminary results might provide an indication for trans-synaptic effects of the L68P mutation, which is located post-synaptically. Additional data is required, however, to obtain reliable evidence for such effects. Finally, theta-burst stimulation (TBS) induced LTP was not significantly impaired in *Shank3[+/L68P]* or *Shank3[L68P/L68P]* mice (Fig. 28D and E(right)). However, significantly reduced LTP induction could be observed in slices prepared from *Shank3[L68P/L68P]* mice (Fig. 28E(left)).

Independently, patch-clamp recordings of miniature excitatory and inhibitory post-synaptic currents (mEPSCs and mIPSCs) in the hippocampal CA1 region of P21 *Shank3$^{+/+}$* and *Shank3$^{L68P/L68P}$* male mice revealed a significant reduction in the frequency and amplitude of mEPSCs but not mIPSCs (*data not shown; based on personal communication with Prof. Eunjoon Kim*). While this observed reduction in excitatory transmission is consistent with the reduced number of excitatory post-synaptic puncta in primary culture, discrepancies occur for inhibitory transmission. Although inhibitory post-synaptic puncta have been found to be reduced to a similar extent as excitatory post-synaptic puncta in primary culture, no changes of inhibitory transmission were evident in patch-clamp recordings. This suggests that in fact higher inhibitory transmission might be present compared to the WT but masked due to the reduction of inhibitory post-synapses. Collectively, these results indicate a potential shift in the E/I balance of homozygous knock-in mice.

Overall, this preliminary electrophysiological characterization of L68P knock-in mice demonstrates that cellular alterations translate to a functional network level and might result in reduced excitatory synaptic transmission in *Shank3$^{+/L68P}$* or *Shank3$^{L68P/L68P}$* mice. This is corroborated by patch-clamp recordings suggesting a reduced mEPSC frequency and amplitude. Additionally, L68P knock-in mice might exhibit a shifted E/I balance as no reduction in mIPSC frequency and amplitude was observed although neurons display a reduced number of inhibitory post-synapses.

3   Discussion and perspective

3.1   Mutation-induced structural alterations represent an initial breaking point for higher order pathogenic processes in SHANK3-mediated autism

The PSD integral scaffolding protein SHANK3 exerts a crucial function in organizing signaling events in glutamatergic post-synapses (Monteiro & Feng, 2017). Consequently, mutations and deletions in the *SHANK3* gene have been attributed a causal role for the development of ASD as well as other neuropsychiatric conditions such as the Phelan-McDermid syndrome (PMS) associated with intellectual disabilities of various severity (Leblond et al., 2014). Despite their clinical relevance, knowledge of the structural consequences of SHANK3 missense mutations is very limited.

Generally, proteins exert their physiological functions by forming spatiotemporally regulated interaction networks and complexes, which are based on their individual three-dimensional structures. Consequently, disease-associated missense mutations frequently alter several basic protein characteristics in parallel such as stability, dynamics or various types of interactions (Kucukkal et al., 2015). These structural properties, however, are highly interrelated resulting in unique local and global changes in response to a given missense mutation, making it difficult to directly assess or predict their physiological impact (Kucukkal et al., 2015). On the other hand, such difficulties might arise from the substantial paucity of studies linking mutation-induced structural perturbations of proteins relevant for the development of neuropsychiatric diseases to the corresponding cellular and functional consequences. Different plausible molecular mechanisms of disease-associated missense mutations have already been outlined elsewhere highlighting the relevance of detailed structural analyses to understand the origin of a disease (Hijikata et al., 2017; Stefl et al., 2013).

The present study demonstrates substantial differences in the structural consequences of the ASD-associated SHANK3 missense mutations R12C and L68P despite being located within the same domain. While the R12C substitution is located within an antiparallel beta-sheet directly at the N-terminus and represents a charge-loss mutation, L68P is found in the SPN/ARR domain interface region close to an α-helix and is thus expected to affect the folding and domain interface integrity of SHANK3. Specifically, the main structural differences between these mutant variants are associated with protein folding as well as secondary and tertiary structure stability. The R12C mutant showed no impairments in the corresponding tertiary structure stability. On the other hand, the L68P mutant displayed no stability reduction of the secondary structure but showed a significantly reduced tertiary structure stability. Furthermore, the L68P mutant appears to be partially unfolded, which is not observed for the R12C variant. This individuality of increased secondary structure thermal stability compared to the WT without exhibiting mutation-induced structural consequences is likely to impede a universal description of SHANK3-mediated autism. Additionally, the existence of several splice isoforms representing truncated versions of the FL protein and covering only a subset of domains constitutes another complicating factor. To date at least 10 different SHANK3 isoforms, which are differentially expressed in individual brain regions and across development have been described (Wang et al., 2014).
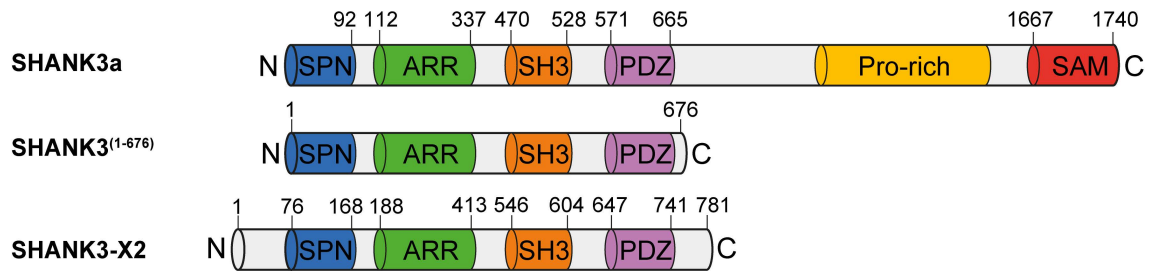
Figure 29: Domain scheme of the potential new SHANK3-X2 isoform
The upper scheme depicts the domain organization of the canonical SHANK3a isoform, which represents the FL protein. In the middle, the truncated SHANK3$^{(1-676)}$ variant is shown, which was used for the characterization of mutation-induced structural alterations. This protein variant may not represent the SHANK3b isoform, which was predicted to arise from alternative promoter usage within the *Shank3* gene and would thus lack most of the SPN domain. On the bottom, the predicted X2 isoform is shown, which is very similar to SHANK3$^{(1-676)}$ but exhibits an extended N- and C-terminus.

The existence of additional isoforms has been predicted but was not experimentally confirmed yet (Fig. 29). Ongoing work has demonstrated that one of these predicted isoforms, termed SHANK3-X2, might indeed exist in the mouse brain and is very similar to the SHANK3$^{(1-676)}$ fragment used for the analysis of structural consequences induced by the R12C and L68P missense mutations (Fig. 29). SHANK3 isoforms are likely to be differentially affected by a given missense mutation depending on the precise protein architecture, subcellular localization, developmental stage, and expression pattern resulting in various possible physiological outcomes. Simultaneously, potential dominant negative functions of mutation-carrying isoforms affecting other isoforms that do not carry the mutation by themselves cannot be excluded. Collectively, these aspects may constitute a molecular basis for the high phenotypic and symptomatic heterogeneity of patients carrying SHANK3 missense mutations. By understanding structural alterations elicited by these missense mutations as initial breaking points and origin of pathogenic processes associated with molecular interactions, signaling events, synaptic and network function, the broad phenotypic spectrum of SHANK3 patients might be better understood.

3.2 Cellular and signaling consequences of SHANK3 missense mutations

These distinguishable structural changes suggest that each individual pathogenic missense variant may be associated with a more or less unique profile of molecular, cellular and higher order impairments, although partial overlaps may exist. Recent attempts to create a unified picture of relevant ASD-pathways associated with different gene mutations therefore face the complexity and broad range of mutation-induced pathological alterations on multiple levels (Luo et al., 2018; Sakai et al., 2011). Due to the versatility of SHANK3 function in dendritic spines, multiple different missense mutation associated pathogenic processes such as modified dendritic spine morphologies, altered SHANK3 ligand binding affinities, epigenetic mechanisms or altered SHANK3 phosphorylation states have been described (Durand et al., 2012; Mameza et al., 2013; Qin et al., 2018; Wang, Pang et al., 2019). Additionally, novel SHANK3-associated pathogenic pathways might be discovered by systematically analyzing changes in the interactome of mutant SHANK3 variants and their corresponding cellular impact. Previous studies followed a similar approach by investigating brain-region specific SHANK3 interactomes from *EGFP-Shank3* transgenic mice to further understand the heterogeneity of SHANK3-associated disorders (Lee et al., 2017). The present work extends these findings by providing evidence that multiple biological processes such as cytoskeletal protein binding, protein kinase and phosphatase activity, ion binding or protein-containing complex binding are altered in response to either one or both studied SHANK3 missense mutations. Furthermore, no clear directionality of mutation-induced changes in the composition of SHANK3-associated complexes was identifiable as proteins within individual complexes (e.g. kinase, microtubule, pre-synaptic active zone or protein transport) were both up- or downregulated. This inconsistency was also present between the effects mediated by either the R12C or L68P mutation, which elicited comparable changes of proteins such as SynGAP1, CaMKIIa, SHANK1 or SIPA1L1 (upregulated) or AKAP8, KIF2A, MAP7D1 or USP7 (downregulated) but also distinct effects for proteins such as AKAP8L, DCLK2, ERC2, PAK7 or SYNJ1. Follow-up pulldown experiments validated the initial finding of increased binding of SynGAP1 to mutant SHANK3 and further demonstrated that the interaction of SHANK3 with SynGAP is likely to be isoform-specific as increased binding was only observed for the AviTag-GFP-SHANK3$^{(1-676)}$ construct but not for GFP-SHANK3^{FL}. Importantly, activity-dependent CaMKIIα mediated phosphorylation of SynGAP has been shown to result in rapid phospho-SynGAP dispersion out of the spine head thereby activating the Ras - Rac1 signaling cascade resulting in spine enlargement and increased post-synaptic AMPAR insertion (Araki et al., 2015). Furthermore, SynGAP mutations disrupting this mechanism have been linked to intellectual disability (Araki et al., 2015). In line with this notion, a PDZ-domain "slot binding" model has been proposed to explain the anchoring of PDZ-domain binding proteins such as SynGAP to the scaffold protein PSD-95 (Walkup et al., 2016). Besides PSD-95, however, SHANK3 might thus represent another crucial PDZ-domain containing interaction partner of SynGAP such that an increased interaction with SHANK3 mutants in the PSD potentially interferes with SynGAP dispersion, although the principal interaction of SHANK3 with SynGAP1 has been described previously (Sakai et al., 2011). Such a mechanism would imply consequences for the dynamics of the actin cytoskeleton in dendritic spines as well as for activity-induced AMPAR insertion and is likely to constitute a new ASD-relevant

pathogenic pathway, which will be investigated further by ongoing research, bringing together the two autism-associated synaptic proteins SynGAP and SHANK3.

In contrast to the results from the previous interactome analysis, follow-up pulldown experiments also suggested that not only CaMKIIα but also CaMKIIβ is binding to SHANK3. This interaction seems to be lost in both studied SHANK3 mutants and will be further investigated in ongoing research. Collectively, these results highlight that even a single missense mutation may elicit widespread changes in multiple different protein complexes and signaling pathways in parallel underpinning the high heterogeneity of such molecular alterations. Nonetheless, common effects such as the increased binding of the R12C and L68P mutant to SynGAP were also observed implicating that individual shared pathogenic pathways might exist.

Mass spectrometry of SHANK3[(1-676)] associated protein complexes revealed another shared feature as both mutants were observed to be hyperphosphorylated compared to the WT. Additionally, a previously unknown ubiquitination site was identified on the L68P mutant. Preliminary follow-up experiments suggested that indeed mutant SHANK3-associated protein complexes enriched from HEK293 cells are significantly more ubiquitinated leading to the expectation of increased *de novo* protein synthesis rates in affected neurons. In contrast, rat primary hippocampal neurons overexpressing mutant SHANK3 variants showed no change in relative protein translation rates compared to the WT. Recent studies, however, have highlighted the connection between SHANK3 phosphorylation and ubiquitination as a way to regulate intracellular SHANK3 stability (Wang, Adamski et al., 2019). Thereby, ERK2 was shown to phosphorylate SHANK3 leading to enhanced ubiquitination and proteasomal degradation (Wang, Adamski et al., 2019). Consistently, the present work suggests that the studied ASD-associated SHANK3 missense mutations might be dysregulated by exhibiting altered posttranslational modification patterns, adding another level of complexity to the pathogenicity of these mutations.

As most SHANK3-associated signaling events are central to the regulation of synaptic structure and function, it is likely that corresponding missense mutations will result in distinct forms of synaptic dysfunction via different mechanisms (Hassani Nia & Kreienkamp, 2018; Macgillavry et al., 2016; Wang, Adamski et al., 2019; Yi et al., 2016). FRAP experiments in rat hippocampal primary neurons, for example, demonstrated increased recovery kinetics of R12C mutant SHANK3, while the L68P mutant was indistinguishable from the WT. This increased mobility of R12C mutant SHANK3 presumably reduces the availability of functional SHANK3 proteins at the PSD, which might partially resemble haploinsufficiency. Notably, *SHANK3* gene dosage dependency of neuronal structure and function is well established leading to haploinsufficiency phenotypes associated with idiopathic autism and PMS (Betancur & Buxbaum, 2013; Durand et al., 2007; Yi et al., 2016). While SHANK3 haploinsufficiency has been mostly investigated using heterozygous knock-out models (Bozdagi et al., 2010; Lee et al., 2015), much less is known about patients carrying missense mutations in one allele, which do not result in altered overall amounts of translated SHANK3 protein per se. The present work provides an initial line of evidence that such a haploinsufficiency-like phenotype might not be restricted to patients carrying large *SHANK3* gene deletions but may also arise from individual *SHANK3* missense mutations. Additionally, both studied mutants were shown to alter the mobile fraction of the SHANK3 interaction partner cortactin, which is known to regulate actin dynamics in dendritic spines (Macgillavry et

al., 2016). This demonstrates that the pathogenic effects of SHANK3 missense mutations extend the level of altering static PPIs by directly or indirectly affecting the intracellular dynamics of interaction partners such as cortactin (Mikhaylova et al., 2018). Importantly, co-IP experiments highlight that the underlying interaction of SHANK3 mutants with cortactin is not impaired, demonstrating that the alteration of cortactin dynamics is not based on changes of the PPI itself, but is likely to modify the availability and function of cortactin in dendritic spines.

Simultaneously, the L68P mutant was found to exhibit a significantly increased dendritic cluster formation tendency with approximately half of these clusters representing excitatory shaft synapses based on their colocalization with bassoon. Interestingly, despite showing many changes in the structure, interactome and intracellular dynamics which are different from the L68P mutant, the R12C mutant exhibited a similar but less pronounced increase of dendritic cluster formation compared to the WT. All tested SHANK3 variants showed a colocalization with homer1 of approximately 30% in the dendritic shaft, which increases to almost 100% in dendritic spines suggesting a different post-synaptic protein composition of these excitatory shaft synapses. Notably, both mutant variants readily interacted with homer1 and had no effect on homer1 dynamics in rat primary hippocampal neurons. Collectively, an increased fraction of excitatory shaft synapses in neurons expressing L68P mutant SHANK3 indicates that the observed molecular impairments elicited by missense mutations translate to a functional level, which may lead to altered synaptic transmission and network function.

3.3   The *SHANK3^{L68P}* knock-in mouse as ASD model

Most studies addressing the molecular, physiological or behavioral basis of *SHANK3* associated neurological disorders focus on a full or partial gene knockout, which is well-suited to analyze SHANK3 dosage-dependent effects, but does not allow to investigate the pathogenicity of corresponding *SHANK3* missense mutations (Han et al., 2016; Lee et al., 2015; Yi et al., 2016; Yoo, Cho et al., 2019). Only one study recently described the generation of a *SHANK3* Q321R mutant knock-in mouse line with anxiolytic-like behavior, decreased seizure susceptibility and decreased excitability of CA1 pyramidal neurons (Yoo, Yoo et al., 2019). For this mutant, however, a detailed structural and biochemical characterization of molecular alterations is largely missing. In contrast, the present work provides a comprehensive analysis of structural, biochemical, and cellular alterations elicited by L68P mutant SHANK3, to which subsequent findings in the *SHANK3* L68P mutant knock-in mouse model can be related.

Thereby, the dendritic spine density serves as initial estimate for potential synaptic transmission impairments in neurons endogenously expressing L68P mutant SHANK3. Previous studies provide an inconclusive picture regarding the impact of SHANK3 missense mutations on the dendritic spine density. While overexpression of the L68P mutant in hippocampal primary neurons for 5 days was found to have no effect on the number of dendritic spines compared to WT (Mameza et al., 2013), the overexpressed R12C mutant was found to significantly reduce spine density (Durand et al., 2012). Independently, no changes of spine numbers were observed in the present work upon overexpression of R12C or L68P mutant SHANK3 variants in rat primary hippocampal neurons overnight. Notably, however, previous studies have demonstrated the sensitivity

of the dendritic spine morphology, density and function towards the overall amount of WT SHANK3 present (Peça et al., 2011; Wang et al., 2011). Consequently, the impact of overexpressed mutants might be partially alleviated by the presence of two endogenous WT *Shank3* alleles. Consistently, the quantification of homer1 and gephyrin puncta in *Shank3*$^{+/L68P}$ and *Shank3*$^{L68P/L68P}$ knock-in neurons prepared from newborn mouse hippocampi revealed a profound reduction of both excitatory (homer1) and inhibitory (gephyrin) post-synapses suggesting impairments in synaptic transmission.

On a PSD ultrastructural level, contrasting results are obtained as well for different *Shank3* knockout mouse models. While no changes in the length and thickness of PSDs from homozygous *Shank3*$^{Δe4-9}$ mice were observed (Wang et al., 2011), homozygous *Shank3B*$^{-/-}$ mice displayed significantly thinner and shorter PSDs compared to WT (Peça et al., 2011). The latter is consistent with TEM results obtained for *SHANK3*$^{L68P/L68P}$ mice exhibiting significantly reduced length, thickness and density of PSDs in CA1 pyramidal neurons (*data not shown in the present work; information from personal communication with Prof. Eunjoon Kim*). Overall, additional data from heterozygous *SHANK3*$^{+/L68P}$ mice are needed to estimate whether these ultrastructural changes are relevant for heterozygous patients carrying this mutation. Nonetheless, STED images recorded from both heterozygous and homozygous L68P knock-in mouse neurons suggest that the nanostructural organization of SHANK3 in dendritic spines is indeed significantly altered in both genotypes. Ongoing research is focusing on an appropriate quantification and extension of STED nanoscopy data.

Collectively, these morphological impairments elicited by the L68P mutation strongly suggest corresponding functional deficits. Consistently, electrophysiological field recordings from 2 - 4 months old male heterozygous and homozygous L68P knock-in mice revealed a reduced synaptic transmission, which could be independently confirmed by patch-clamp recordings from CA1 pyramidal neurons of 21 days old *Shank3*$^{L68P/L68P}$ mice demonstrating a reduced mEPSC frequency and amplitude (*patch-clamp data not shown in the present work; information from personal communication with Prof. Eunjoon Kim*). For optimal comparability, however, patch-clamp recordings from older mice additionally incorporating the heterozygous genotype are needed and are part of ongoing research. Furthermore, electrophysiological field recordings suggest the presence of trans-synaptic effects of the L68P mutation as alterations in the PPR of *Shank3*$^{L68P/L68P}$ mice were found. Such trans-synaptic effects could be potentially mediated by the neuroligin-neurexin pair as SHANK3 has been described to interact with neuroligins directly and indirectly (Betancur et al., 2009). Simultaneously, α-neurexin 1 was implicated in functional coupling of Ca^{2+} channels to the presynaptic membrane, relevant for Ca^{2+}-induced neurotransmitter release (Betancur et al., 2009). Finally, despite significantly reduced LTP induction in *Shank3*$^{L68P/L68P}$ mutant mice, stable expression of LTP was evident and comparable to the WT situation. Overall, functional analyses demonstrated that even a subtle change within SHANK3 such as a single missense mutation is enough to trigger profound alterations of neuronal communication.

The present work provides evidence that mutation-induced structural changes serve as starting point for a chain of defects acting on multiple different levels from altered intracellular protein dynamics to changes of biochemical signal transduction, PSD morphology or spine numbers and finally result in the observed functional and network impairments. The study further highlights the complexity and heterogeneity of molecular and cellular defects elicited by different SHANK3 missense mutations as well as the

potential to discover additional pathophysiological pathways relevant for the development of ASD and related neurological disorders by further investigating structure-function relationships of SHANK3 missense mutations. The provided data further puts ASD elicited by SHANK3 missense mutations in the context of protein conformational diseases, which are broadly described as pathological conditions arising from disturbances of the native protein conformation either by genetic mutations or other external triggers (Liguori et al., 2020; Tao & Conn, 2018). Novel therapeutic approaches for such pathologies thus aim to reconstitute the native protein fold by using pharmacological chaperones, which specifically bind to misfolded proteins (Liguori et al., 2020; Tao & Conn, 2018). The present work suggests that such a strategy might also be applicable for ASD elicited by SHANK3 missense mutations resulting in corresponding structural perturbations as molecular basis for higher-order pathological events. Further research is required, however, to determine the structural and functional impact of other SHANK3 missense variants and to shed light on the possibility of alleviating certain phenotypes by the development of pharmacological chaperones.

Materials and methods

The following methods have been published previously as part of this work and have been adapted with modifications from (Bucher et al., 2021).

Protein expression and purification

For structural studies, recombinant His$_6$-SUMO-SHANK3$^{(1-676)}$ or SHANK3$^{(1-676)}$ variants were expressed and purified from chemically competent *E. coli* BL21(DE3) bacteria, which have been transformed with the corresponding pET vectors. Bacteria were cultured in LB medium at 37 °C in the presence of kanamycin until OD$_{600}$ ~ 0.5, where recombinant protein expression was induced by addition of 300 µM isopropyl-b-D-thiogalactopyranoside (IPTG). Protein expression was continued for 16 - 18 hours at 18 °C. All subsequent steps were performed either on ice or at 4 °C to enhance protein stability. Bacteria were harvested by centrifugation and resuspended in 250 mM NaH$_2$PO$_4$, 250 mM NaCl, 0.5 mM DTT, 10 mM Imidazole, 1x Complete Protease Inhibitor Cocktail (Merck Millipore), pH = 6.5. Subsequently, bacterial lysis was performed by treatment with lysozyme for 30min on ice followed by mild sonication, a freeze-thaw cycle and another sonication step. To reduce the viscosity of the lysate, Benzonase nuclease was added to a final concentration of 50 U/ml and the lysate was finally cleared by centrifugation. His$_6$-tagged proteins were then captured from the lysate by Ni^{2+}-IDA chromatography (Profinity IMAC resin, Bio-Rad) under gravity flow and washed with 250 mM NaH$_2$PO$_4$, 250 mM NaCl, 0.5 mM DTT, 35 mM Imidazole, 1x Complete Protease Inhibitor Cocktail, pH = 6.5. For CD and nanoDSF measurements, protease inhibitors were removed prior to elution by additional washes with inhibitor-free washing buffer to facilitate SUMO-protease activity for recombinant tag removal. Proteins were subsequently eluted with 200 mM Imidazole (batch elution). To this preparation the home-made SUMO protease His$_6$-SenP2 was added to a final concentration of approximately 0.3 mg/ml and proteins were incubated for 2 hours at 4 °C under gentle rotation for cleavage of the His$_6$-SUMO tag. Following addition of Complete Protease Inhibitor Cocktail to inhibit any further proteolytic activity, the preparation was diluted to a final Imidazole concentration of approximately 30 mM and was loaded twice onto a freshly packed Ni^{2+}-IDA column to remove both His$_6$-SenP2 as well as the cleaved His$_6$-SUMO tag. Subsequently, dilute proteins were concentrated using Amicon Ultra 15 ml centrifugal filters (Merck Millipore, 10 kDa NMWCO) and subjected to single-step buffer exchange into SEC running buffer (100 mM NaH$_2$PO$_4$, 100 mM NaCl, 0.5 mM DTT, pH = 6.5) over a PD10 desalting column (GE Healthcare, Sephadex G-25 M matrix) under gravity flow. Eluted proteins were finally up-concentrated using Amicon Ultra 0.5 ml centrifugal filters (Merck Millipore, 30 kDa NMWCO) and stored on wet ice. For any downstream application such as CD spectroscopy, nanoDSF or SEC, purified proteins were always used freshly and were never frozen and thawed.

Size exclusion chromatography (SEC) for SAXS measurements

Bacterially expressed His$_6$-SUMO-SHANK3$^{(1-676)}$ variants were pre-purified over Ni^{2+}-IDA under gravity flow as described above and eluted in 500-750 µl fractions with 250 mM

NaH$_2$PO$_4$, 250 mM NaCl, 0.5 mM DTT, 200 mM Imidazole, 1x Complete Protease Inhibitor Cocktail, pH = 6.5. Subsequently, proteins were subjected to SEC at 4 °C with a flow rate of 0.4 ml/min (running buffer 100 mM NaH$_2$PO$_4$, 100 mM NaCl, 0.5 mM DTT, pH = 6.5) using a Superdex 75 10/300 GL column (GE Healthcare). Individual SEC peak fractions of His$_6$-SUMO-SHANK3$^{(1-676)}$ variants were pooled and pre-concentrated with an Amicon Ultra 4 ml centrifugal filter (Merck Millipore, 30 kDa NMWCO). Finally, protein concentration was determined spectrophotometrically based on 280 nm absorption using SEC running buffer for blank subtraction. Protein preparations were directly used for subsequent SAXS measurements without any intermediate storage.

Small-angle X-ray scattering (SAXS)

To establish protein dilution series for SAXS measurements, pre-concentrated SEC peak fractions of each His$_6$-SUMO-SHANK3$^{(1-676)}$ variant were diluted accordingly in SEC running buffer.

SAXS measurements (I(s) versus s with s[nm^{-1}] = 4πsin(θ)/λ and 2θ being the scattering angle) were performed at the EMBL-P12 bioSAXS beam line (PETRAIII, DESY, Hamburg; Blanchet et al., 2015) under default operating conditions (10 keV, λ = 0.124 nm, Pilatus 6M detector with a distance of 3.0 m) at 10 °C. Data was collected in the s-range of 0.0287–7.267 for 20 successive frames with an exposure time of 0.05 sec per frame. Primary data processing included radial averaging, normalization and buffer subtraction. Subsequently, data analysis was performed with the software package ATSAS 3.0.1 (Franke et al., 2017).

For experimental SAXS profiles the radius of gyration was calculated using the Guinier approximation with automated detection of a suitable Guinier range by AUTORG (Petoukhov et al., 2007). The R$_g$ values of the WT and R12C mutant variant of SHANK3 showed a linear concentration dependence so that subsequent analyses were performed on SAXS profiles, which were extrapolated to zero concentration. The real space pair-distance distribution functions (PDDFs, P(r) vs. r profiles) were approximated from the experimental scattering data via an indirect Fourier transform (IFT) procedure using the program GNOM (Svergun, 1992). Accordingly, the values for R$_g$ and D$_{max}$ were determined by using automated criteria for the Lagrange parameter and D$_{max}$. To model the topology of His$_6$-SUMO-SHANK3$^{(1-676)}$ variants from crystallographic structures of individual domains, the program CORAL was used (Petoukhov et al., 2012). Thereby, the employed crystallographic structures (SMT3(aa 13-98): chain C from PDB 2EKE, SPN-ARR: PDB 5G4X, SH3: PDB 5O99, PDZ: PDB 5OVA) are rotated and translated with certain restrictions to minimize the discrepancy between the experimental and the computed (model-derived) SAXS profile (Duda et al., 2007; Lilja et al., 2017; Ponna et al., 2017, 2018). Dimeric subunit structures were split into corresponding monomers before using them as input for CORAL. For zero-extrapolated SAXS profiles, no symmetry restrictions were used (P1 symmetry) to model the topology of monomeric His$_6$-SUMO-SHANK3$^{(1-676)}$ variants, while P2 symmetry restrictions were employed for corresponding dimer models from SAXS data merged between highest and lowest concentrations. The atomic model of the SPN-ARR fragment was allowed to move freely while all other subunits were fixed. N- and C-termini as well as missing inter-domain linker regions were added to the crystallographic structures as dummy residues (DRs) based on the ORF of His$_6$-SUMO-SHANK3$^{(1-676)}$ in the corresponding pET vector. To

account for a potential mutation-induced disruption of the SPN/ARR domain interface, monomeric CORAL models were additionally created using a split SPN-ARR fragment, where the unstructured linker region (KRRVYAQNLI) has been replaced by the same number of DRs to allow flexible movement of both domains. The resulting structural models were visualized using PyMOL. SAXS data was deposited to SASBDB (WT: SASDLJ3, R12C: SASDLL3 and L68P: SASDLK3).

To characterize the conformational ensemble of His_6-SUMO-SHANK3$^{(1-676)}$ variants, distributions of their R_g and D_{max} values were derived by fitting experimental SAXS data with the program EOM 2.0 of the ATSAS 3.0.1 package (Bernadó et al., 2007; Tria et al., 2015).

Circular dichroism spectroscopy

To analyze mutation-induced perturbations of the secondary structure, circular dichroism spectroscopy of SHANK3$^{(1-676)}$ variants was done on a Chirascan circular dichroism spectrometer (Applied Photophysics). For the measurement of full CD spectra, samples were prepared essentially as described above with some modifications. Briefly, pre-purified SHANK3$^{(1-676)}$ variants (approximately 1 mg/ml) were buffer exchanged into 10 mM KH_2PO_4, 100 mM KF, 0.5 mM DTT, pH = 6.5 using PD10 desalting columns (GE Healthcare) under gravity flow immediately before measurement. Protein concentration was adjusted to approximately 2 µM and far-UV CD spectra were subsequently acquired in the wavelength range of 260 - 185 nm at 10 °C in a 1 mm quartz cuvette (0.5 nm step size, 3 s/point, three repeats). Finally, data processing was performed as described elsewhere (Greenfield, 2007d).

Equilibrium chemical unfolding was performed from Ni^{2+}-IDA purified concentrated SHANK3$^{(1-676)}$ stock solutions without the necessity of further buffer exchange. Concentrated protein stock solutions were diluted to approximately 2 µM and mixed with 10 M Urea in SEC running buffer to establish a urea concentration series for each variant. Samples including blank were equilibrated on ice for at least 30 min and ellipticity was subsequently measured at 222 nm at 10 °C (3 s/point, 25 µs sample period, three repeats). After each CD measurement, the sample was recovered for subsequent assessment of protein concentration by BCA assay. The data was averaged, corrected for buffer absorption, and converted to the mean residue ellipticity [θ] as described elsewhere (Greenfield, 2007d). The equilibrium chemical unfolding data was subsequently fitted to a two-state unfolding transition model, which is given by the equation (Agashe & Udgaonkar, 1995):

$$y_{obs} = \frac{y_N^0 + m_N[D] - y_U^0 - m_U[D]}{1 + e^{-\frac{\Delta G^0 + m_G[D]}{RT}}} + y_U^0 + m_U[D] \qquad \text{Eq. (1)}$$

Here, the intercepts y_N^0 and y_U^0 as well as the slopes m_N and m_U of the native (N) and unfolded (U) baseline regions were obtained by linear extrapolation and used as fixed parameters in the fitting of equation (1) (Santoro & Bolen, 1988). The ideal gas constant R (8.31446 J/(mol·K)) as well as the temperature T (283.15 K) were used as additional constants and the denaturant concentration [D] was implemented as independent

variable. Parameters obtained from the fit were ΔG^0 and the cooperativity parameter m_G. This allows the subsequent calculation of the free energy of unfolding:

$$\Delta G_{unfold} = \Delta G^0 + m_G[D]$$

Eq. (2)

Previous experiments showed that for the tested SHANK3[(1-676)] variants aggregation precedes the onset of secondary structure melting upon thermal ramping. Therefore, melting curves were acquired in the presence of a non-denaturing urea concentration (2.0 M), which was determined from equilibrium chemical unfolding. Consequently, "2.0 M urea" samples from the equilibrium chemical unfolding series were recovered for subsequent thermal unfolding measurements. Thermal unfolding was performed as described previously (Greenfield, 2007c) with few modifications. Briefly, for each SHANK3[(1-676)] variant CD data was acquired at 222 nm for 3 s/point with a sampling period of 25 µs over a temperature range of 10 - 90 °C. Temperature changes were made in a stepped ramping mode with a heating rate of 1.0 °C/min (1.0 °C steps) and 30 s settling time (0.5 °C tolerance). Thereby, the actual sample temperature was monitored by a temperature sensor inside the sample and was used for further data processing. To determine the corresponding melting temperatures, the data was fitted to a Boltzmann model.

Nano differential scanning fluorimetry (nanoDSF)

To monitor changes in protein tertiary structure upon thermal ramping, label-free fluorescence measurements were performed on a Prometheus NT.48 nanoDSF instrument (NanoTemper Technologies). Thereby, differential exposure or shielding of intrinsic tryptophan reporter residues was used as a readout. Parallel measurements of up to 48 capillaries were done in a single run using nanoDSF grade standard capillaries (10 µl, NanoTemper Technologies). Experiments were set up and monitored with the software PR.ThermControl. Before the actual measurements were conducted, appropriate conditions (excitation power, protein concentration) were established for the tested SHANK3[(1-676)] variants (purified as described above) by several discovery scans to obtain initial fluorescence values of $F_{330nm} > 5,000$ fluorescence counts. For optimal comparability, nanoDSF samples were prepared from the same protein preparations which were used for CD spectroscopy. Ultimately, measurements were performed at 50% excitation power using a protein concentration of 0.5 mg/ml for each SHANK3[(1-676)] variant. Due to known attractive interparticle interactions and protein aggregation tendency, 0.25 - 2.0 M urea (factor 2 dilutions) was additionally added to the samples. Fluorescence emission was detected at 330 nm and 350 nm over a temperature-range of 15 - 90 °C with a heating rate of 1 °C/min. Thereby, thermally induced unfolding was observed to be irreversible and accompanied with protein precipitation even in the presence of 2 M urea. F_{330nm} and F_{350nm} curves were blank subtracted and the ratio F(350/330 nm) was subsequently plotted against temperature. From these melting curves, the first derivatives were calculated and smoothed by a moving average with a window of 100 points. Transition points were finally determined by peak analysis of the corresponding first derivative curves.

Intrinsic tryptophan and extrinsic ANS fluorescence spectroscopy

Fluorescence spectroscopy was performed on a F-7000 fluorescence spectrophotometer (Hitachi) using His$_6$-SUMO-SHANK3$^{(1-676)}$ variants which have been purified as described above. Samples were prepared by dilution of concentrated protein stock solutions to a final concentration of 2 µM in purification buffer (250 mM NaH$_2$PO$_4$, 250 mM NaCl, 0.5 mM DTT, 1x Complete Protease Inhibitor Cocktail (Merck Millipore), pH = 6.5). Measurements were conducted at room temperature in a standard 10 mm rectangular quartz cell. To detect intrinsic tryptophan fluorescence emission, a wavelength scan was performed from 300 to 400 nm with a scan speed of 240 nm/min at an excitation wavelength of 295 nm (5 nm excitation and emission slit, PMT voltage set to 700 V).

To measure protein surface hydrophobicity by extrinsic fluorescence spectroscopy, purified His$_6$-SUMO-SHANK3$^{(1-676)}$ variants (2 µM) in purification buffer were titrated with 10 - 100 µM of 8-anilino-1-naphthalenesulfonic acid (ANS). After equilibration at room temperature, ANS was excited at 365 nm and fluorescence was recorded between 400 - 700 nm with a scan speed of 240 nm/min. Finally, fluorescence spectra were Savitzky-Golay smoothed (third order, seven points window) and buffer subtracted.

Limited Proteolysis

To further test the conformational stability of individual SHANK3$^{(1-676)}$ variants, limited proteolysis was performed by treating proteins with trypsin for defined timepoints. Therefore, purified SHANK3$^{(1-676)}$ variants were incubated with trypsin-EDTA (Gibco Life Technologies) at a molar ratio of 200:1 for 0 - 60 min at room temperature. To a 1 mg/ml (13.5 µM) solution of SHANK3$^{(1-676)}$ WT, R12C or L68P, trypsin-EDTA was added to a final concentration of 67 nM in a total reaction volume of 120 µl. At each timepoint, 15 µl of the reaction mixture were removed and immediately added to 15 µl of 2x SDS sample buffer (125 mM Tris-HCl pH 6.8, 4% (w/v) SDS, 20% (v/v) glycerol, 10% (v/v) β-mercaptoethanol, 0.004% (w/v) bromophenol blue), which was preheated to 95 °C to stop the proteolytic reaction. Subsequently, samples were incubated at 95 °C for 5 min and separated by SDS-polyacrylamide gel electrophoresis on a 4–12% pre-cast NuPage Bis-Tris protein gel (ThermoFisher Scientific). Finally, proteins were stained by Coomassie brilliant blue (CBB). Analysis of lane profiles was done in ImageJ software (NIH).

Molecular dynamics simulations

MD simulations were performed with GROMACS 2018.4 using the Amber03 force field (Duan et al., 2003; Hess et al., 2008; Pronk et al., 2013). Initial coordinates were used from PDB 5G4X (Lilja et al., 2017). The single-point mutants R12C and L68P were created with UCSF Chimera (Pettersen et al., 2004). The peptides were solvated in a cubic box with periodic boundary conditions and a side length of ~110 Å (10 Å initial minimum distance of solute to all boundaries) comprising the protein, ~43,000 H$_2$O molecules and 2-3 chlorine ions to neutralize the protein charge. For all systems, the same molecular dynamics protocol was used. After a steepest descent energy minimization (convergence criteria: 500,000 steps or maximum force < 10 kJ mol^{-1} nm^{-1})

two 100 ps equilibration MD runs were performed. The first one was performed in the constant particle number, volume, temperature ensemble (NVT; with modified Berendsen thermostat with velocity rescaling at 300 K and a 0.1 ps timestep; separate heat baths for protein and solvent) and the second one in the constant particle number, pressure, temperature ensemble (NPT; Parrinello-Rahman pressure coupling at 1 bar with a compressibility of $4.5 \cdot 10^{-5}$ bar^{-1} and a 2 ps time constant; Bussi et al., 2007; Nosé & Klein, 1983; Parrinello & Rahman, 1981). During each equilibration run, a position restraint potential with a force constant of 1,000 kJ mol^{-1} nm^{-2} was added to all protein atoms.

For MD simulations the leap-frog integrator was used with a time step of 2 fs. Coordinates were saved every 10 ps. The same temperature and pressure coupling schemes as applied for the equilibration runs were used for the subsequent MD simulations. All bonds to hydrogen atoms were constrained using the Linear Constrained Solver (LINCS) with an order of 4 and one iteration (Hess et al., 1997). A grid-based neighbor list with a threshold of 10 Å was used and updated every 5 steps (10 fs). The particle-mesh Ewald method was used for long-range electrostatic interactions above 10 Å with a fourth order interpolation and a maximum spacing for the FFT grid of 1.6 Å (Darden et al., 1993; Essmann et al., 1995). Lennard-Jones interactions were cut-off above 10 Å. A long-range dispersion correction for energy and pressure was used to compensate for the Lennard-Jones interaction cut-off (Hess et al., 2008).

MD trajectories were visualized and analyzed using VMD 1.9.3 (Humphrey et al., 1996). Backbone RMSD and RMSF traces were calculated from every fifth frame using the inbuilt RMSD Trajectory Tool or a Tcl script, respectively.

Preparation of primary hippocampal neurons and transfection

All animal experiments were carried out in accordance with the European Communities Council Directive (2010/63/EU) and the Animal Welfare Law of the Federal Republic of Germany (Tierschutzgesetz der Bundesrepublik Deutschland, TierSchG) approved by the local authorities of the city-state Hamburg (Behörde für Gesundheit und Verbraucherschutz, Fachbereich Veterinärwesen) and the animal care committee of the University Medical Center Hamburg-Eppendorf.

Cultures of primary hippocampal neurons from rat embryos were essentially prepared as previously described (van Bommel et al., 2019). Pregnant Wistar rats Crl:WI (Charles River) were anesthetized with CO_2, sacrificed and hippocampi were dissected from E18 embryos in ice-cold HBSS (Sigma Aldrich). Following 5 washing steps with 9 ml of ice-cold HBSS each, dissected hippocampi were treated with 0.25% trypsin-EDTA (Thermo Fisher Scientific; 100 µl / hippocampus) in 2 ml of HBSS for 10 min at 37 °C. Subsequently, hippocampi were physically dissociated, and the cell suspension was filtered and plated with a density of 40,000 - 60,000 cells / ml on 18 mm glass coverslips, which have been coated with poly-L-lysine (PLL). Cells were initially plated in DMEM supplemented with 10% (v/v) fetal bovine serum (FBS) as well as Penicillin / Streptomycin (PS). After one hour, the medium was exchanged with BrainPhys neuronal medium supplemented with SM1 (Stemcell) and 0.5 mM glutamine. Neurons were grown and maintained at 37 °C, 5% CO_2 and 95% humidity.

Cultures of primary hippocampal neurons from early postnatal mice (P0) were essentially prepared as previously described (Beaudoin et al., 2012) and similar to the preparation of primary rat hippocampal neurons, with few modifications. Briefly, dissected mouse hippocampi were collected in 450 µl of ice-cold HBSS and 50 µl of 0.25% trypsin-EDTA (Thermo Fisher Scientific) was added to a final concentration of 0.025%. The tissue was incubated in a water bath at 37 °C for 15 min and subsequently washed twice with 500 µl of pre-warmed HBSS. After removal of HBSS, the hippocampi were resuspended in 1 ml of pre-warmed plating medium (DMEM + 10% FCS + Penicillin / Streptomycin) and physically dissociated. Finally, the cell suspension was filtered and plated with a density of 80,000 cells / ml on PLL-coated glass coverslips. After one hour, the plating medium was exchanged with Neurobasal A medium supplemented with B27 (Gibco Life Technologies), 4 mM glutamine and 1 mM sodium pyruvate. Neurons were grown and maintained at 37 °C, 5% CO_2 and 95% humidity.

For transfection both plasmid DNA and lipofectamine 2000 were diluted accordingly in blank BrainPhys neuronal medium, mixed (DNA/lipofectamine ratio 1:2) and incubated at room temperature for 40min. In parallel the neuronal growth medium was collected and replaced by pre-warmed BrainPhys medium supplemented with 0.5 mM glutamine. Subsequently, the transfection mix was added to the neurons for 1 – 1.5 hours before the medium was exchanged back to the conditioned medium. Expression periods were limited to < 24 hours.

Immunostainings, spinning disk confocal microscopy and image analysis

For immunostainings, cultured mouse or rat primary hippocampal neurons were fixed in phosphate-buffered formaldehyde (PBS pH = 7.4, 4% formaldehyde, 4% (w/v) sucrose) for 10 min at room temperature. Following three washes with PBS (pH = 7.4) cells were permeabilized by treatment with PBS-T (PBS pH = 7.4, 0.2% (v/v) Triton X-100) for 10 min at room temperature. Subsequently, neurons were washed three times with PBS (pH = 7.4) and incubated with blocking buffer (PBS pH = 7.4, 10% (v/v) horse serum, 0.1% (v/v) Triton X-100) for 45 - 60 min at room temperature. Cells were incubated with primary antibodies diluted accordingly in blocking buffer at 4 °C overnight and were washed three times with PBS (pH = 7.4) before incubation with corresponding secondary antibodies in blocking buffer for 2 hours at room temperature. Following three final washes with PBS (pH = 7.4) cells were mounted on microscopy slides with Mowiol (Carl Roth, prepared according to manufacturer's protocol including DABCO as antifading agent).

Spinning-disk confocal microscopy was done using a Nikon Eclipse Ti-E microscope, which was controlled by the VisiView software (Visitron Systems). The microscope was equipped with 488, 561 and 639 nm excitation lasers coupled to a CSU-X1 spinning-disk unit (Yokogawa) via a single-mode fiber. Emission was collected through a quad-band filter (Chroma, ZET 405 / 488 / 561 / 647 nm) on an Orca flash 4.0LT CMOS camera (Hamamatsu). For fixed primary hippocampal neurons, z-stack images were taken by using a 100x objective (Nikon, ApoTIRF 100_/1.49 oil) with a pixel size of 65 nm^2 and a z-stack interval of 0.3 µm.

All images were processed and analyzed using ImageJ. For co-localization analysis of either endogenous SHANK3 or overexpressed GFP-SHANK3^{FL} variants (WT, R12C or

L68P) with synaptic markers (homer and bassoon), the shape of the entire analyzed dendrite including spines was drawn based on the MAP2 and synaptic marker staining by hand using the segmented line tool. Subsequently, the number of individual SHANK3, homer and bassoon as well as co-localized puncta was detected via the ComDet v.0.5.1 plugin. Co-localization was then calculated by dividing the amount of co-localized puncta by the total number of individual SHANK3, homer and bassoon puncta, respectively.

Spine density and the number of SHANK3 clusters were quantified in neurons overexpressing both GFP-SHANK3^{FL} variants (WT, R12C, L68P) as well as mRuby2 as a volume marker. For spine density analysis, a construct expressing GFP alone was used as a control to monitor the dosage-dependent effect of SHANK3 overexpression. The number of spines was counted using the multi-point tool based on the mRuby2 channel and was normalized to a dendrite length of 10 µm. The number of SHANK3 clusters in the dendrite (SHANK3$_{den}$) as well as in spines (SHANK3$_{spi}$) was quantified for each genotype using the multi-point tool. The fraction of SHANK3 clusters in dendrite versus spines was then calculated for each genotype by individually dividing SHANK3$_{den}$ and SHANK3$_{spi}$ by the total number of SHANK3 clusters.

For the fluorescence intensity ratio analysis of SHANK3 clusters in dendrites and spines, a line profile covering the entire spine width was drawn based on the mRuby2 and SHANK3 channel. The line profile initiates at the head of a measured spine and terminates on its adjacent dendrite. Subsequently, the mean gray value was plotted along the line profile. Finally, detected peak values from the spine and dendritic region were divided by each other to calculate the ratio of SHANK3 cluster distribution.

Fluorescence recovery after photobleaching (FRAP)

FRAP measurements were conducted in living primary rat hippocampal neurons, which were prepared as described above and which were co-transfected at DIV14-16 with 1.8 µg / well of pHAGE-EF1α-GFP-SHANK3^{FL} (WT, R12C, L68P) and 0.5 µg / well of pAAV-mRuby2 for a maximum of 16 - 18 hours to avoid morphological artifacts of SHANK3 overexpression. Subsequent live imaging and photobleaching was performed on a Nikon Eclipse Ti-E microscope using a 100x objective (CFI Apochromat TIRF 100XC oil, 1.49 NA) where imaging parameters were defined within the software VisiView (Visitron Systems). Specifically, after five baseline images (16-bit, 65 nm^2 / pixel, 5 s interval) photobleaching was achieved by scanning each ROI (i.e. individually selected spines) for 2 ms / pixel with a 488 nm laser at 50 - 70% laser power (acquisition turned off during photobleaching). Subsequently, 120 post-bleach images were acquired with 5 s interval. To stimulate neuronal activity, cultures were pre-incubated with 50 µM (+) - bicuculline (Tocris) for 5 min at 5% CO_2 and 37 °C and subsequently imaged for a maximum of 45 min to avoid artifacts from neuronal over-activation.

For FRAP measurements of SHANK3 interaction partners (cortactin, homer1), cultures of primary rat hippocampal neurons were co-transfected at DIV14-16 with 1.0 µg / well of pHAGE-EF1α-GFP-SHANK3^{FL} (WT, R12C, L68P) and 1.0 µg / well of either pFUGW-f(syn)homer1-tdTomato-WPRE or mCherry-cortactin for 16 - 18 hours. Live imaging was performed as described above, except for photobleaching, which was achieved by scanning each ROI for 3 ms / pixel with a 561 nm laser at 100% laser power.

Finally, image analysis was performed on raw, unprocessed images using ImageJ. Mean gray values were obtained from ROIs of bleached spines, non-bleached control regions and the background for each frame by using the "plot z-axis profile" function within ImageJ. Subsequently, FRAP curves of each analyzed spine were background subtracted, normalized to the non-bleached control region and scaled between 0 and 1. Ultimately, individual FRAP curves were averaged for each condition and statistical analysis was performed with the Origin 2019b software package (OriginLab).

Fluorescent non-canonical amino acid tagging (FUNCAT)

To visualize the newly synthesized protein pool in primary rat hippocampal neurons, FUNCAT was performed as described previously with few modifications (Dieterich et al., 2010). Briefly, primary rat hippocampal neurons were transfected at DIV14-16 with 1.8 µg / well of pHAGE-EF1α-GFP-SHANK3^{FL} (WT, R12C, L68P) for 16 - 18 hours. One group of transfected neurons was additionally pharmacologically silenced by treatment with 1 µM tetrodotoxin (TTX) and 50 µM D-(-)-2-amino-5-phosphonopentanoic acid (D-APV) prior to metabolic labeling to account for the neuronal activity dependence of *de novo* protein synthesis. Subsequently, transfected neurons were metabolically labelled by initially replacing the growth medium with methionine-free HibA medium (BrainBits LLC) for 20 min to deplete the cells of endogenous methionine. Thereafter, neurons were incubated either with 4 mM L-azidohomoalanine (AHA; Click Chemistry Tools) or 4 mM L-methionine (Sigma Aldrich) in HibA medium for 2 - 3 hours at 37 °C and 5% CO_2. Following metabolic incorporation of functionalized amino acids, neurons were washed with cold PBS-MC (PBS pH = 7.4, 1 mM $MgCl_2$, 0.1 mM $CaCl_2$) on ice and fixed in phosphate-buffered formaldehyde (PBS pH = 7.4, 4% formaldehyde, 4% (w/v) sucrose) for 10 min at room temperature. Following three washing steps with PBS (pH = 7.4), fixed cells were permeabilized by treatment with PBS-T (PBS pH = 7.4, 0.25% (v/v) Triton X-100) for 10 min at room temperature and washed again three times with PBS (pH = 7.4). Subsequently, cells were incubated with blocking buffer (PBS pH = 7.4, 10% (v/v) horse serum, 0.1% (v/v) Triton X-100) for 1 hour at room temperature and finally washed three times with PBS (pH = 7.8).

For click-labeling of endogenous AHA-labeled proteins by copper-catalyzed azide-alkyne [3 + 2] cycloaddition (CuAAC), a reaction mix containing 200 µM Tris-[(1-benzyl-1H-1,2,3-triazol-4-yl)-methyl]-amine (TBTA; Sigma Aldrich), 500 µM Tris(2-carboxyethyl)phosphine hydrochloride (TCEP; Sigma Aldrich), 2 µM fluorescent alkyne tag (TAMRA-PEG4-alkyne; Click Chemistry Tools), and 200 µM $CuSO_4$ (Sigma Aldrich) was prepared in PBS (pH = 7.8). Special attention was paid to the addition of compounds in correct order as listed above to prevent unwanted side reactions and the reaction mix was vortexed for several seconds after each addition of a reagent. Stock solutions of these reagents were prepared in sterile, distilled H_2O, except for TBTA, which was dissolved in DMSO. Subsequently, neurons were incubated with the reaction mix in a dark, humidified chamber overnight at room temperature with gentle agitation. Following three consecutive washes with FUNCAT wash buffer (PBS pH = 7.8, 0.5 mM EDTA, 1% (v/v) Tween-20) and two additional washes with PBS (pH = 7.4), neurons were immunostained for homer as described above to facilitate the detection of labeled and unlabeled excitatory spines. Finally, click-labeled and immunostained cells were mounted on microscopy slides with Mowiol (Carl Roth, prepared according to manufacturer's protocol including DABCO as antifading agent) and imaged by spinning-

disk confocal microscopy as described above. Analysis of synaptic TAMRA intensities was done in ImageJ and data was plotted and statistically analyzed using Origin 2019b (OriginLab).

Additional Methods

The following methods and associated results have not been included in the publication mentioned above but are part of this thesis.

Constructs and cloning

For cloning of the pEGFP-C2-AviTag-GFP-SHANK3$^{(1-676)}$ WT construct, the SHANK3$^{(1-676)}$ coding sequence (*rattus norvegicus*; accession NM_021676.3; 2028 bp) was PCR amplified from the pET-His$_6$-SUMO-SHANK3$^{(1-676)}$ WT construct, which has been described elsewhere (Bucher et al., 2021). To facilitate PCR amplification of this GC-rich sequence, the template construct was previously linearized by restriction with *XbaI*. The PCR product was then inserted into an empty pEGFP-C2 vector using the *SalI* and *BglII* restriction sites. Since the SHANK3$^{(1-676)}$ coding sequence carries several internal restriction sites, cloning of the corresponding R12C and L68P mutant pEGFP-C2-AviTag-GFP-SHANK3$^{(1-676)}$ constructs was done without PCR amplification. Therefore, an internal 1589 bp fragment of SHANK3 was obtained from both the pET-His$_6$-SUMO-SHANK3$^{(1-676)}$ R12C and L68P construct by *BstXI* and *XhoI* restriction and inserted into the previously cloned pEGFP-C2-AviTag-GFP-SHANK3$^{(1-676)}$ WT plasmid thereby introducing the desired point mutations. All newly cloned constructs were verified by sequencing. Other expression constructs used in this work were kind gifts from collaborators and a complete list is provided at the end of this section.

Mass spectrometric analysis of mutant SHANK3 interactomes

To analyze the effect of SHANK3 mutations on their interactomes, mass spectrometry of corresponding pulldown samples was performed. In essence, recombinant AviTag-GFP-SHANK3$^{(1-676)}$ variants (WT, R12C, L68P) were purified from HEK239 cells and used as bait for pulldowns from freshly prepared rat brain lysates. Pulldown samples were then separated by SDS-PAGE and analyzed by LC-MS/MS.

For preparation of individual AviTag-GFP-SHANK3$^{(1-676)}$ variants (WT, R12C, L68P), HEK293 cells were co-transfected with either 5.0 µg of pEGFP-C2-AviTag-GFP-SHANK3$^{(1-676)}$ (WT or mutant) or 5.0 µg of pEGFP-C2-AviTag-GFP (control group) and 2.0 µg of pCl-Neo-BirA per dish (100 mm) using linear polyethyleneimine (PEI; MW 40,000; Polysciences). To facilitate efficient biotinylation of the AviTag by the biotin ligase BirA, the growth medium was replaced with a 1:1 mixture of DMEM (Gibco Life Technologies) and Ham's F10 medium (Biozym) supplemented with 10% (v/v) FBS (Gibco Life Technologies) as well as PS (Invitrogen) shortly before addition of the transfection mix. Following overnight expression of recombinant proteins, cells were harvested in ice-cold, protease inhibitor-supplemented TBS (20 mM Tris-HCl pH = 7.4, 150 mM NaCl, 1x Complete Protease Inhibitor Cocktail). After centrifugation of the cell

suspension at 1,000 g for 3 min at 4 °C, the supernatant (SN) was aspirated and the cell pellet was resuspended in 500 μl / dish of ice-cold HEK extraction buffer (20 mM Tris-HCl pH = 7.4, 150 mM NaCl, 1% (v/v) Triton X-100, 1x Complete Protease Inhibitor Cocktail). To lyse the cells, samples were frozen at -80 °C and subsequently thawed at room temperature to break up cell membranes. To improve protein extraction, the pre-lysate was additionally incubated for 30 min on ice and mixed regularly. Finally, the pre-lysate was centrifuged at 20,000 g for 15 min at 4 °C and the SNs containing recombinant biotinylated AviTag-GFP-SHANK3$^{(1-676)}$ variants were collected. Here, SNs from two 100 mm dishes were pooled for each group (WT, R12C, L68P and GFP-control) resulting in a total lysate volume of 1 ml per group for subsequent protein isolation.

To purify biotinylated AviTag-GFP-SHANK3$^{(1-676)}$ variants from the corresponding lysates, 200 μl of magnetic dynabeads M-280 (50 μl per group; Thermo Fisher Scientific) containing covalently attached Streptavidin were pre-washed three times with 1 ml of normal wash buffer (20 mM Tris-HCl pH = 7.4, 150 mM NaCl, 0.1% (v/v) Triton X-100) each. Subsequently, the beads were blocked in 1 ml of beads blocking buffer (20 mM Tris-HCl pH = 7.4, 150 mM NaCl, 0.2% (w/v) chicken egg albumin) for 1 hour at room temperature under gentle rotation to minimize unspecific protein binding thereby reducing the protein background observed by mass spectrometry. After blocking, the beads were washed once with 1 ml of normal wash buffer and resuspended in 200 μl of extraction buffer. To 1 ml of lysate 50 μl of resuspended, blocked dynabeads were added and incubated for 2 hours at 4 °C under gentle rotation. Thereafter, beads were magnetically separated from the lysate and washed twice with 1 ml each of low salt wash buffer (20 mM Tris-HCl pH = 7.4, 100 mM NaCl, 0.1% (v/v) Triton X-100, 1x Complete Protease Inhibitor Cocktail), twice with 1 ml each of high salt wash buffer (20 mM Tris-HCl pH = 7.4, 500 mM NaCl, 0.1% (v/v) Triton X-100, 1x Complete Protease Inhibitor Cocktail) and another two times with 1 ml each of low salt wash buffer. The isolated AviTag-GFP-SHANK3$^{(1-676)}$ variants were subsequently used as bait for pulldowns from freshly prepared rat brain lysates.

To prepare rat brain lysates, an adult male or female Wistar rat Crl:WI (Charles River) was anesthetized with CO_2, sacrificed and the brain was removed. The cerebellum was cut off with a scalpel and the remaining tissue was transferred to a sterile, pre-chilled 15 ml tube on ice. After weighing, the tissue was rinsed with approximately 5 ml of ice-cold TBS (pH = 7.4) and transferred to a pre-chilled Potter-Elvehjem tissue homogenization tube. To the tissue, 9 ml / g ice-cold tissue lysis buffer (50 mM Tris-HCl pH = 7.4, 150 mM NaCl, 0.1% (w/v) SDS, 0.2% (v/v) NP-40, 1x Complete Protease Inhibitor Cocktail) was added and the tissue was homogenized with several strokes at 300 - 1000 rpm using a Potter-Elvehjem homogenizer (Sartorius) at 4 °C. The homogenate was pre-cleared from residual cell debris by centrifugation at 900 g for 15 min at 4 °C and the SN was again centrifuged at 15,000 g for 20 min at 4 °C to obtain the final lysate.

To probe the differential interactome of SHANK3 mutants, 1 ml of freshly prepared rat brain lysate was added to 50 μl of each purified, biotinylated AviTag-GFP-SHANK3$^{(1-676)}$ variant (WT, R12C, L68P) or to 50 μl of the purified AviTag-GFP control protein. The samples were incubated at 4 °C for 4 hours under gentle rotation and were subsequently washed five times with 1 ml of normal wash buffer supplemented with 1x Complete Protease Inhibitor Cocktail each. The washed beads were resuspended in 50 μl of 2x NuPage LDS sample buffer (supplemented with 2x NuPage reducing reagent; Thermo Fisher Scientific) and incubated for 10 min at 70 °C to strip off bound protein complexes.

Ultimately, the beads were magnetically removed from the solution and proteins were separated on a 4-12% NuPage Bis-Tris gel (Thermo Fisher Scientific) using NuPage MOPS SDS running buffer (Thermo Fisher Scientific). The gel was stained with Coomassie brilliant blue (CBB) to visualize separated proteins and to facilitate subsequent gel band excision for mass spectrometric analysis.

For the AviTag-GFP-SHANK3[(1-676)] interactome and phosphorylation state analysis, SDS-PAGE gel lanes were cut into 2 mm slices and subjected to in-gel reduction with dithiothreitol (DTT), alkylation with iodoacetamide and digestion with trypsin (sequencing grade; Promega) as previously described (Schwertman et al., 2012). Nanoflow liquid chromatography tandem mass spectrometry (nLC-MS/MS) was performed on an EASY-nLC coupled to an Orbitrap Fusion Tribrid mass spectrometer (ThermoFisher Scientific) operating in positive mode. Peptides were separated on a ReproSil-C18 reversed-phase column (Dr Maisch; 15 cm × 50 μm) using a linear gradient of 0–80 % acetonitrile (in 0.1 % formic acid) during 90 min at a rate of 200 nl/min. The elution was directly sprayed into the electrospray ionization (ESI) source of the mass spectrometer. Spectra were acquired in continuum mode; fragmentation of the peptides was performed in data-dependent mode by higher energy collision dissociation (HCD).

Raw mass spectrometry data were analyzed with the MaxQuant software suite (Cox et al., 2009) as described previously (Schwertman et al., 2012) with the additional options 'LFQ' and 'iBAQ' selected. The A false discovery rate (FDR) of 0.01 for proteins and peptides and a minimum peptide length of 7 amino acids were set. The Andromeda search engine was used to search the MS/MS spectra against a Uniprot database, taxonomy *Rattus norvegicus* (version January 2019) concatenated with the reversed versions of all sequences. A maximum of two missed cleavages was allowed. The peptide tolerance was set to 10 ppm and the fragment ion tolerance was set to 0.6 Da for HCD spectra. The enzyme specificity was set to trypsin and cysteine carbamidomethylation was set as a fixed modification, while methionine oxidation, phosphorylation (STY) and ubiquitination (GlyGly (K)) were set as variable modifications. Both the peptide spectral match (PSM) and protein FDR were set to 0.01. If the identified peptides of two proteins were the same or the identified peptides of one protein included all peptides of another protein, these proteins were combined by MaxQuant and reported as one protein group. Known contaminants and reverse hits were removed. Both the 'evidence' and 'modificationsspecificpeptides' output text files were used for further in-depth analysis.

GO-term enrichment analysis of identified proteins was performed using the database STRING to identify biological processes affected by either of the mutations. Independently, identified proteins were functionally clustered using the database for annotation, visualization and integrated discovery (DAVID). Individual clusters were selected and known interactions between proteins within a given cluster were subsequently visualized using Cytoscape. Finally, proteins were color-coded according to their mutation-induced change in abundance relative to the WT dataset.

Analysis of SHANK3[(1-676)]-associated protein complex ubiquitination

To probe the ubiquitination state of SHANK3[(1-676)]-associated protein complexes, HEK293 cells were co-transfected with 3.5 μg of pEGFP-C2-AviTag-GFP-SHANK3[(1-676)]

(WT or mutant) and 1.5 µg of pcDNA3-HA-Ubiquitin (addgene #18712) per 100 mm dish using PEI as described above. After recombinant protein expression overnight, cells were harvested in ice-cold PBS (pH = 7.4) and lysed with 500 µl / dish of ice-cold HEK extraction buffer as described above. Following a freeze and thaw cycle and subsequent incubation on ice for 30 min, the pre-lysate was centrifuged for 15 min at 20,000g at 4 °C and the SNs were collected for subsequent pulldowns.

To isolate ubiquitinated SHANK3$^{(1-676)}$-complexes from HEK293 lysates, 20 µl / dish of GFP-trap magnetic agarose beads (Chromotek) were first washed by adding 1 ml of HEK extraction buffer each. After removal of the washing solution, 500 µl of each HEK293 lysate (containing ubiquitinated AviTag-GFP-SHANK3$^{(1-676)}$ protein complexes) were added to the beads and incubated for 2 hours at 4 °C under gentle rotation. Subsequently, the beads were washed three times each with 1 ml of GFP-trap washing buffer (20 mM Tris-HCl pH = 8.0, 150 mM NaCl, 5 mM MgCl$_2$, 0.5% (v/v) Triton X-100, 1x Complete protease Inhibitor Cocktail) and were finally resuspended in 50 µl of 2x SDS sample buffer each. Proteins were eluted and denatured at 95 °C for 5 min, separated by SDS-PAGE at 120 - 180 V and blotted on a PVDF membrane for 80 min at 110 V in blotting buffer (25 mM Tris, 192 mM glycine, 20% (v/v) methanol). The membrane was blocked with 5% (w/v) milk in TBS for 1.5 hours at room temperature and subsequently incubated with the primary antibody (rat-α-HA, Roche; diluted 1:1000 in TBS) overnight at 4 °C with gentle agitation. After washing three times with TBS-T, the membrane was incubated with the corresponding HRP-linked secondary antibody at room temperature for 2 hours. After three final washes with TBS-T, chemiluminescence was detected using a self-made substrate solution (100 mM Tris-HCl pH = 8.5, 1.25 mM luminol, 2 mM 4-iodophenylboronic acid, 5.3 mM H$_2$O$_2$). Membranes were scanned using a ChemoCam imaging system (Intas) and obtained images were processed with Fiji.

Excitatory and inhibitory spine quantification in primary hippocampal mouse neurons

To analyze the effect of the L68P mutation on excitatory and inhibitory spine densities, primary hippocampal mouse neurons derived from either WT, heterozygous or homozygous *Shank3^{L68P}* knock-in mice, were immunostained for homer (excitatory spine marker), gephyrin (inhibitory spine marker) and MAP2 as described above. Confocal laser scanning microscopy (CLSM) was essentially performed as described elsewhere (van Bommel et al., 2019). Briefly, images were acquired on a Leica TCS SP5 confocal microscope (Leica Microsystems) equipped with a 488 nm argon laser, a 561 nm solid state laser and a 633 nm He-Ne laser using a 63x oil objective (1.40 NA) and an image size of 1024 x 1024 pixels with 4x zoom (frame average = 2, z-stack interval = 0.29 µm). Main dendrites proximal to the soma were imaged with a minimum distance from the soma of 10 µm.

Image processing and analysis was performed with Fiji. For spine quantification, maximum intensity projections of z-stacks were used. Subsequently, the length of individual dendrites was measured before excitatory and inhibitory marker puncta were counted in the corresponding channels using the "find maxima" function within Fiji. Detected excitatory and inhibitory marker puncta were normalized to a dendrite length of 10 µm. Finally, comparisons between genotypes within the excitatory or inhibitory spine groups were done by 1-way ANOVA with Tukey's posthoc test.

SHANK3 pulldown and western blot analysis of the interaction with SynGAP and CaMKIIa

To verify mass spectrometry results indicating differential binding of SHANK3[(1-676)] mutants to different PSD-associated proteins, pulldown experiments were performed from adult rat brain lysates. These pulldowns were essentially done as described in the chapter "mass spectrometric analysis of mutant SHANK3 interactomes" with few modifications. Briefly, HEK293 cells were co-transfected with 5.0 µg of pEGFP-C2-AviTag-GFP-SHANK3[(1-676)] (WT or mutant) or 5.0 µg of pEGFP-C2-AviTag-GFP (control group) and 2.0 µg of pCl-Neo-BirA per 100 mm dish (2 dishes per group, 4 groups) using PEI as described above. Transfected cells were harvested after overnight expression and cell lysates were prepared by resuspension of harvested cells in 500 µl / dish of ice-cold HEK extraction buffer. In contrast to the procedure described above, here half of the cells (i.e. one dish per group) was lysed in the presence of a self-made phosphatase-inhibitor cocktail (final concentrations: 10 mM KF, 2 mM Na_3VO_4, 1.15 mM $Na_2MoO_4 \cdot 2 H_2O$, 1 mM dibasic sodium pyrophosphate, 2 mM Imidazole), which was added to the HEK extraction buffer to additionally probe the dependence of individual PPIs on the phosphorylation state of either SHANK3 itself or its interaction partners. Following lysis, biotinylated and differentially phosphorylated AviTag-GFP-SHANK3[(1-676)] (WT or mutant) was enriched from the lysates using magnetic dynabeads M-280 (25 µl / dish; Thermo Fisher Scientific) as described above. Enriched SHANK3[(1-676)] variants as well as the AviTag-GFP control were subsequently added to 1 ml of rat brain lysate each (prepared as described above, 4 x with phosphatase inhibitors and 4 x without phosphatase inhibitors) and were incubated for 4 hours at 4 °C. Finally, the samples were washed five times with each 1 ml of normal wash buffer supplemented with 1x Complete Protease Inhibitor Cocktail and for half of the samples additionally supplemented with phosphatase inhibitors. The washed beads were resuspended in 50 µl of 2x SDS sample buffer and proteins were eluted by heating for 5 - 10 min at 98 °C.

Eluted proteins were subsequently separated by SDS-PAGE and transferred on a PVDF membrane for 80 min at 110V in blotting buffer. The membrane was blocked in 5% (w/v) milk in TBS for 1.5 hours at room temperature followed by incubation with the primary antibody overnight at 4 °C with gentle agitation. After washing three times with TBS-T, the membrane was incubated with the corresponding HRP-linked secondary antibody at room temperature for 2 hours. After three final washes with TBS-T, chemiluminescence was detected using a self-made substrate solution. Membranes were scanned using a ChemoCam imaging system (Intas) and obtained images were processed with Fiji.

STED imaging of SHANK3 nanoclusters in primary hippocampal mouse neurons and data analysis

To analyze the nanoarchitecture of SHANK3 in spines by gated STED imaging, primary hippocampal mouse neurons derived from P0 pups of *Shank3[L68P]* knock-in mice (WT, heterozygous or homozygous for the L68P mutation) were immunostained for SHANK3, bassoon and homer as described above (see chapter Immunostainings, spinning disk confocal microscopy and image analysis). Subsequent gated STED imaging was performed as described previously (van Bommel et al., 2019). Briefly, STED images were acquired on a Leica TCS SP8-3X system (Leica Microsystems) equipped with a white light laser (WLL) for excitation in the range of 470 - 670 nm using a 100x oil

objective (HC PL APO 100x/1.40 OIL; Leica Microsystems). Excitation of dyes conjugated to corresponding secondary antibodies was performed at 650 nm for Atto647N (emission detection between 660 - 730 nm), at 561 nm for Abberior STAR 580 (emission detection between 580 - 620 nm) and at 488 nm for Alexa Fluor 488 (emission detection between 500 - 530 nm). STED was achieved using a 592 nm continuous wave depletion laser for Alexa Fluor 488 and a 775 nm pulsed depletion laser for both Atto647N and Abberior STAR 580 dyes. The image size was set to 1,024 x 1,024 pixels using an optical zoom factor of 5 resulting in a pixel size of 22.73 nm. Images were acquired with a scan speed of 600 lines per second and 16x line averaging. Confocal images were obtained with the same principal settings but with reduced laser power.

Subsequent image processing and analysis was done using Fiji. First, initial excitatory spine detection was done using the confocal homer signal, which was converted to an 8-bit image and blurred using a Gaussian filter (radius = 2 pixels). Homer puncta were detected using the "find maxima" function in Fiji (prominence value depending on the individual intensity distributions). While the initial number of homer spot counts was saved, the ROIs of detected maxima were enlarged (radius = 0.25 μm) to create corresponding masks, which were used for the subsequent quantification of the number and area of SHANK3 nanoclusters in the STED channel. Prior to particle analysis within the STED channel (SHANK3 signal), the corresponding image was blurred using a Gaussian filter (radius = 1 pixel) followed by thresholding and watershed segmentation to separate overlapping SHANK3 clusters. The individually processed STED images were then overlaid with the previously created homer masks to avoid dendritic SHANK3 signals. Finally, the number and area of SHANK3 nanoclusters was measured within the homer masks using the "analyze particles" function in Fiji (particle cutoff = 4 pixels, circularity = 0.0 - 1.0). Both parameters were normalized to the number of homer puncta and data was plotted and statistically analyzed using Origin 2019b.

Electrophysiological field recordings

For extracellular field recordings, 8-16 weeks old C57BL6/J $Shank3^{+/+}$, $Shank3^{+/L68P}$ or $Shank3^{L68P/L68P}$ male mice were used to prepare transversal brain slices containing the hippocampal formation. Briefly, animals were anesthetized with 80% CO_2 / 20% O_2 and sacrificed by decapitation. Brains were rapidly removed from the skull and placed in ice-cold modified artificial cerebrospinal fluid (aCSF; 110 mM Choline chloride, 25 mM $NaHCO_3$, 25 mM D-Glucose, 11.6 mM Na-L-Ascorbate, 7 mM $MgSO_4$, 1.25 mM NaH_2PO_4, 2.5 mM KCl, 0.5 mM $CaCl_2$, pH 7.4, equilibrated with 95% O_2 / 5% CO_2). Transversal brain slices (400 μm) were prepared with a microtome vf-200 tissue slicer (Compresstome, Precisionary Instruments) and then incubated at 30 °C for approximately 90 min in physiological aCSF (124 mM NaCl, 26 mM $NaHCO_3$, 10 mM D-Glucose, 1 mM $MgSO_4$, 1 mM NaH_2PO_4, 4 mM KCl, 2.4 mM $CaCl_2$, pH 7.4, equilibrated with 95% O_2 / 5% CO_2). The hemi-slices were subsequently transferred to the Synchroslice (Lohmann Research Equipment) recording chambers perfused with aCSF at a flow rate of ~2 ml/min using a peristaltic pump (MINIPULS 3, Gilson). All recordings were performed at a temperature of 30°C using a 2-channel Miniature Preamplifier (Multi Channel Systems). For extracellular field recordings, a single fiber electrode (Lohmann Research Equipment) was placed in the middle third of the *stratum radiatum* of the CA1 hippocampal area (recording electrode). Field excitatory postsynaptic potentials (fEPSPs) were evoked by activating Schaffer collaterals (SCs) using a semi-micro

concentric bipolar electrode (Lohmann Research Equipment) placed in the middle third of the *stratum radiatum* 150 - 200 μm away from the recording electrode. Square-wave current pulses were generated by a stimulus generator (STG 4008, Multi Channel Systems) and delivered to the tissue. Input/Output (I/O) curves were generated by stimulating with increasing current pulses from 100 to 1500 μA in an interval of 100 μA. The paired-pulse ratio (PPR) was measured by delivering two stimuli each using 50, 100, 200 and 500 ms inter-stimulus intervals respectively. Therefore, synaptic facilitation was examined by repetitive stimulation (5 times) for each inter-stimulus interval and the resulting potentials were averaged. The PPR was then calculated by dividing the slope of the second EPSP by the slope of the first EPSP. For long-term potentiation (LTP) experiments, the synaptic strength was determined based on the EPSP slope. Baseline recordings were performed using stimuli that resulted in a response equal to 30-40% of the maximum response, applying one stimulus every 30 s for 30 minutes. LTP was induced after the baseline with a single theta burst stimulation consisting of a series of 10 bursts, 5 stimuli each (100 Hz within the burst and 200 ms inter-burst interval). Data analysis was performed blindly.

Key Resource Table

List of key resources used for the work presented here.

Reagent	Designation	Source or reference	Identifier	Additional information
primary antibody	guinea pig polyclonal Shank3	Synaptic Systems	162304	for ICC (1:500)
primary antibody	rabbit polyclonal homer-1,2,3	Synaptic Systems	160103	for ICC (1:500)
primary antibody	chicken polyclonal bassoon	Synaptic Systems	141016	for ICC (1:500)
primary antibody	mouse monoclonal bassoon	Enzo Life Sciences	ADI-VAM-PS003-D	for ICC (STED) (1:250)
primary antibody	mouse monoclonal gephyrin	Synaptic Systems	147011	for ICC (1:500)
primary antibody	mouse monoclonal MAP2-AF488	Merck Millipore	MAB3418X	for ICC (1:500)
primary antibody	rabbit polyclonal SynGAP	Synaptic Systems	157003	for Western Blot (1:1000)
primary antibody	rabbit polyclonal CaMKIIα	Cell Signaling Technology	3357	for Western Blot (1:1000)
primary antibody	rabbit monoclonal pCaMKII (Thr286)	Cell Signaling Technology	12716	for Western Blot (1:1000)

primary antibody	mouse monoclonal GFP	Covance	MMS-118P-500	for Western Blot (1:3000)
primary antibody	rat monoclonal RFP	Chromotek	5F8	for Western Blot (1:1000)
secondary antibody	goat polyclonal anti-mouse IgG (H+L)-AF488	Thermo Fisher Scientific	A-11029	for ICC (STED) (1:250)
secondary antibody	goat polyclonal anti-guinea pig IgG-STAR 580	Abberior	ST580-1006-500UG	for ICC (STED) (1:250)
secondary antibody	rabbit polyclonal IgG anti-chicken IgY (H+L)-Cy3	Dianova	303-165-003	for ICC (1:500)
secondary antibody	goat polyclonal anti-rabbit IgG (H+L)-AF568	Thermo Fisher Scientific	A-11036	for ICC (1:500)
secondary antibody	goat polyclonal anti-guinea pig IgG-STAR 635P	Abberior	ST635P-1006	for ICC (1:500)
secondary antibody	goat polyclonal anti-rabbit IgG-Atto647N	Sigma-Aldrich	40839	for ICC (STED) (1:250)
secondary antibody	goat polyclonal anti-mouse IgG-AF647	Thermo Fisher Scientific	A-21236	for ICC (1:500)
secondary antibody	goat polyclonal anti-rat IgG (H+L)-HRP	Jackson ImmunoResearch	112-035-062; RRID:AB_2338133	for Western Blot (1:2500)
secondary antibody	goat polyclonal anti-mouse IgG (H+L)-HRP	Jackson ImmunoResearch	115-035-003; RRID:AB_10015289	for Western Blot (1:2500)
bacterial strain (*Escherichia coli*)	XL10 gold	Stratagene	200314	for plasmid DNA production
bacterial strain (*Escherichia coli*)	BL21(DE3)	Thermo Fisher Scientific	K30001	for protein purification
bacterial strain (*Escherichia coli*)	Stbl2	Invitrogen	10268-019	obtained from Matthias Kneussel
bacterial strain (*Escherichia coli*)	embryonic kidney (HEK 293T)	ATCC	CRL-3216; RRID:CVCL_0063	for co-IP

plasmid construct (rat)	pET-His$_6$-SUMO-SHANK3$^{(1-676)}$ WT	a gift from Hans-Jürgen Kreienkamp (UKE)	for bacterial protein production
plasmid construct (rat)	pET-His$_6$-SUMO-SHANK3$^{(1-676)}$ R12C	a gift from Hans-Jürgen Kreienkamp (UKE)	for bacterial protein production
plasmid construct (rat)	pET-His$_6$-SUMO-SHANK3$^{(1-676)}$ L68P	a gift from Hans-Jürgen Kreienkamp (UKE)	for bacterial protein production
plasmid construct (rat)	pEGFP-C2-AviTag-GFP-SHANK3$^{(1-676)}$ WT	this study	for mass spectrometry and pulldown studies
plasmid construct (rat)	pEGFP-C2-AviTag-GFP-SHANK3$^{(1-676)}$ R12C	this study	for mass spectrometry and pulldown studies
plasmid construct (rat)	pEGFP-C2-AviTag-GFP-SHANK3$^{(1-676)}$ L68P	this study	for mass spectrometry and pulldown studies
plasmid construct (rat)	pHAGE2-EF1a-EGFP-SHANK3^{FL} WT	a gift from Hans-Jürgen Kreienkamp (UKE)	for transfection of hippocampal primary neurons
plasmid construct (rat)	pHAGE2-EF1a-EGFP-SHANK3^{FL} R12C	a gift from Hans-Jürgen Kreienkamp (UKE)	for transfection of hippocampal primary neurons
plasmid construct (rat)	pHAGE2-EF1a-EGFP-SHANK3^{FL} L68P	a gift from Hans-Jürgen Kreienkamp (UKE)	for transfection of hippocampal primary neurons
plasmid construct (rat)	pmRFP-N3-SHANK3^{FL} WT	doi: 10.1038/ncb3487	for transfection of HEK293 cells and co-IP
plasmid construct (rat)	pmRFP-N3-SHANK3^{FL} R12C	doi: 10.1038/ncb3487	for transfection of HEK293 cells and co-IP
plasmid construct (rat)	pmRFP-N3-SHANK3^{FL} L68P	doi: 10.1038/ncb3487	for transfection of HEK293 cells and co-IP
plasmid construct (rat)	pEGFP-C1-Homer1b	Hans-Jürgen Kreienkamp (UKE)	for transfection of HEK293 cells and co-IP

plasmid construct (rat)	pEGFP-C1-SAPAP1	Hans-Jürgen Kreienkamp (UKE)		for transfection of HEK293 cells and co-IP
plasmid construct (human)	pEGFP-C1-Cortactin	Hans-Jürgen Kreienkamp (UKE)		for transfection of HEK293 cells and co-IP
plasmid construct (mouse)	mCherry-Cortactin-C-12	doi: 10.1016/j.neuron.2018.01.046	Addgene plasmid #55020	for transfection of hippocampal primary neurons
plasmid construct (rat)	pFUGW-f(syn)Homer1-tdTomato-WPRE	a gift from Christian Rosenmund (Charité Universitätsmedizin Berlin)	BL-1034	for transfection of hippocampal primary neurons
plasmid construct	pAAV-Syn-mRuby2	doi: 10.15252/embj.2018101183		for transfection of hippocampal primary neurons
plasmid construct	pMAX-GFP	Lonza Bioscience	V4XP-3012	for transfection of hippocampal primary neurons
plasmid construct (human)	pETM11-T7-His$_6$-SenP2	EMBL Heidelberg		for recombinant protein tag removal
recombinant protein	His$_6$-SUMO-SHANK3$^{(1-676)}$ WT	this study		purified from BL21(DE3)
recombinant protein	His$_6$-SUMO-SHANK3$^{(1-676)}$ R12C	this study		purified from BL21(DE3)
recombinant protein	His$_6$-SUMO-SHANK3$^{(1-676)}$ L68P	this study		purified from BL21(DE3)
recombinant protein	SHANK3$^{(1-676)}$ WT	this study		purified from BL21(DE3)
recombinant protein	SHANK3$^{(1-676)}$ R12C	this study		purified from BL21(DE3)
recombinant protein	SHANK3$^{(1-676)}$ L68P	this study		purified from BL21(DE3)
recombinant protein	His$_6$-SenP2	this study		purified from BL21(DE3); for recombinant protein tag removal

chemical compound	Profinity IMAC resin, Ni^{2+}-charged	Bio-Rad	1560135		for protein purification
chemical compound	RFP-trap agarose	Chromotek	rta-20		for co-IP
pharma-cological agent	(+)-Bicuculline	Tocris Bioscience	0130		for treatment of hippocampal primary neurons
pharma-cological agent	Tetrodotoxin	Tocris Bioscience	1078		for treatment of hippocampal primary neurons
pharma-cological agent	D-APV	Tocris Bioscience	0106		for treatment of hippocampal primary neurons
chemical compound	Lipofectamine 2000	Thermo Fisher Scientific	11668019		for transfection of primary hippocampal neurons
chemical compound	TurboFect transfection reagent	Thermo Fisher Scientific	R0532		for transfection of HEK293 cells
commercial assay or kit	BCA protein assay	Thermo Fisher Scientific	23250		for determination of protein concentration
commercial assay or kit	plasmid midi kit	Qiagen	12145		for purification of plasmid DNA
commercial assay or kit	WesternBright chemiluminescence substrate	Biozym	541003		for western blot detection
software	VMD 1.9.3	doi: 10.1016/0263-7855(96)00018-5			for analysis and visualization of molecular graphics
software	Origin 2019b	OriginLab			for graphing and data analysis
software	PyMOL 2.3.4	Schrödinger, Inc.			for molecular visualization
software	ImageJ/Fiji	NIH			for image processing and analysis
software	Adobe Illustrator 2021	Adobe Inc.			for graphing and visualization

software	ATSAS 3.0.1	doi: 10.1107/ S1600576720013412	for analysis of SAXS data
software	SnapGene	GSL Biotech LLC	for plasmid cloning
software	POV-Ray 3.7	other	for ray tracing of molecular graphics

References

Abrahams, B. S., & Geschwind, D. H. (2008). Advances in autism genetics: On the threshold of a new neurobiology. *Nature Reviews Genetics*, *9*(5), 341–355. https://doi.org/10.1038/nrg2346

Agashe, V. R., & Udgaonkar, J. B. (1995). Thermodynamics of Denaturation of Barstar: Evidence for Cold Denaturation and Evaluation of the Interaction with Guanidine Hydrochloride. *Biochemistry*, *34*(10), 3286–3299. https://doi.org/10.1021/bi00010a019

Alexander, C. G., Wanner, R., Johnson, C. M., Breitsprecher, D., Winter, G., Duhr, S., Baaske, P., & Ferguson, N. (2014). Novel microscale approaches for easy, rapid determination of protein stability in academic and commercial settings. *Biochimica et Biophysica Acta - Proteins and Proteomics*, *1844*(12), 2241–2250. https://doi.org/10.1016/j.bbapap.2014.09.016

Araki, Y., Zeng, M., Zhang, M., & Huganir, R. L. (2015). Rapid Dispersion of SynGAP from Synaptic Spines Triggers AMPA Receptor Insertion and Spine Enlargement during LTP. *Neuron*, *85*(1), 173–189. https://doi.org/10.1016/j.neuron.2014.12.023

Atwood, H. L., & Karunanithi, S. (2002). Diversification of synaptic strength: Presynaptic elements. *Nature Reviews Neuroscience*, *3*(7), 497–516. https://doi.org/10.1038/nrn876

Avery, A. W., Fealey, M. E., Wang, F., Orlova, A., Thompson, A. R., Thomas, D. D., Hays, T. S., & Egelman, E. H. (2017). Structural basis for high-affinity actin binding revealed by a β-III-spectrin SCA5 missense mutation. *Nature Communications*, *8*(1), 1–7. https://doi.org/10.1038/s41467-017-01367-w

Baron, M. K., Boeckers, T. M., Vaida, B., Faham, S., Gingery, M., Sawaya, M. R., Salyer, D., Gundelfinger, E. D., & Bowie, J. U. (2006). An Architectural Framework That May Lie at the Core of the Postsynaptic Density. *Science*, *311*(5760), 531–535. https://doi.org/10.1126/science.1118995

Bean, B. P. (2007). The action potential in mammalian central neurons. *Nature Reviews Neuroscience*, *8*(6), 451–465. https://doi.org/10.1038/nrn2148

Beaudoin, G. M. J., Lee, S. H., Singh, D., Yuan, Y., Ng, Y. G., Reichardt, L. F., & Arikkath, J. (2012). Culturing pyramidal neurons from the early postnatal mouse hippocampus and cortex. *Nature Protocols*, *7*(9), 1741–1754. https://doi.org/10.1038/nprot.2012.099

Benavides-Piccione, R., Regalado-Reyes, M., Fernaud-Espinosa, I., Kastanauskaite, A., Tapia-González, S., León-Espinosa, G., Rojo, C., Insausti, R., Segev, I., & Defelipe, J. (2020). Differential Structure of Hippocampal CA1 Pyramidal Neurons in the Human and Mouse. *Cerebral Cortex*, *30*(2), 730–752. https://doi.org/10.1093/cercor/bhz122

Bernadó, P., Mylonas, E., Petoukhov, M. V., Blackledge, M., & Svergun, D. I. (2007). Structural Characterization of Flexible Proteins Using Small-Angle X-ray Scattering. *Journal of the American Chemical Society*, *2*, 5656–5664. https://doi.org/10.1021/ja069124n

Berryer, M. H., Hamdan, F. F., Klitten, L. L., Møller, R. S., Carmant, L., Schwartzentruber, J., Patry, L., Dobrzeniecka, S., Rochefort, D., Neugnot-Cerioli, M., Lacaille, J. C., Niu, Z., Eng, C. M., Yang, Y., Palardy, S., Belhumeur, C., Rouleau, G. A., Tommerup, N., Immken, L., … Di Cristo, G. (2013). Mutations in SYNGAP1 Cause Intellectual Disability, Autism, and a Specific Form of Epilepsy by Inducing Haploinsufficiency. *Human Mutation*, *34*(2), 385–394. https://doi.org/10.1002/humu.22248

Betancur, C., & Buxbaum, J. D. (2013). SHANK3 haploinsufficiency: A "common" but underdiagnosed highly penetrant monogenic cause of autism spectrum disorders. *Molecular Autism*, *4*(1), 4–6. https://doi.org/10.1186/2040-2392-4-17

Betancur, C., Sakurai, T., & Buxbaum, J. D. (2009). The emerging role of synaptic cell-adhesion pathways in the pathogenesis of autism spectrum disorders. *Trends in Neurosciences*, *32*(7), 402–412. https://doi.org/10.1016/j.tins.2009.04.003

Blanchet, C. E., Spilotros, A., Schwemmer, F., Graewert, M. A., Kikhney, A., Jeffries, C. M., Franke, D., Mark, D., Zengerle, R., Cipriani, F., Fiedler, S., Roessle, M., & Svergun, D. I. (2015). Versatile sample environments and automation for biological solution X-ray scattering experiments at the P12 beamline (PETRA III, DESY). *Journal of Applied Crystallography*, *48*, 431–443. https://doi.org/10.1107/S160057671500254X

Blanchet, C. E., & Svergun, D. I. (2013). Small-Angle X-Ray Scattering on Biological Macromolecules and Nanocomposites in Solution. *Annual Review of Physical Chemistry*, *64*(1), 37–54. https://doi.org/10.1146/annurev-physchem-040412-110132

Böckers, T. M., Mameza, M. G., Kreutz, M. R., Bockmann, J., Weise, C., Buck, F., Richter, D., Gundelfinger, E. D., & Kreienkamp, H. J. (2001). Synaptic scaffolding proteins in rat brain: Ankyrin repeats of the multidomain Shank protein family interact with the cytoskeletal protein α-fodrin. *Journal of Biological Chemistry*, *276*(43), 40104–40112. https://doi.org/10.1074/jbc.M102454200

Bodmer, W., & Bonilla, C. (2008). Common and rare variants in multifactorial susceptibility to common diseases. *Nature Genetics*, *40*(6), 695–701. https://doi.org/10.1038/ng.f.136

Boeckers, T. M., Inter, C., Smalla, K. H., Kreutz, M. R., Bockmann, J., Seidenbecher, C., Garner, C. C., & Gundelfinger, E. D. (1999). Proline-rich synapse-associated proteins ProSAP1 and ProSAP2 interact with synaptic proteins of the SAPAP/GKAP family. *Biochemical and Biophysical Research Communications*, *264*(1), 247–252. https://doi.org/10.1006/bbrc.1999.1489

Boeckers, T. M., Liedtke, T., Spilker, C., Dresbach, T., Bockmann, J., Kreutz, M. R., & Gundelfinger, E. D. (2005). C-terminal synaptic targeting elements for postsynaptic density proteins ProSAP1/Shank2 and ProSAP2/Shank3. *Journal of Neurochemistry*, *92*(3), 519–524. https://doi.org/10.1111/j.1471-4159.2004.02910.x

Borgesius, N. Z., van Woerden, G. M., Buitendijk, G. H. S., Keijzer, N., Jaarsma, D., Hoogenraad, C. C., & Elgersma, Y. (2011). βCaMKII plays a nonenzymatic role in hippocampal synaptic plasticity and learning by targeting α;CaMKII to synapses. *Journal of Neuroscience*, *31*(28), 10141–10148. https://doi.org/10.1523/JNEUROSCI.5105-10.2011

Bozdagi, O., Sakurai, T., Papapetrou, D., Wang, X., Dickstein, D. L., Takahashi, N., Kajiwara, Y., Yang, M., Katz, A. M., Scattoni, M., Harris, M. J., Saxena, R., Silverman, J. L., Crawley, J. N., Zhou, Q., Hof, P. R., & Buxbaum, J. D. (2010). Haploinsufficiency of the autism-associated Shank3 gene leads to deficits in synaptic function, social interaction, and social communication. *Molecular Autism*, *1*(1), 1–15. https://doi.org/10.1186/2040-2392-1-15

Bucher, M., Fanutza, T., & Mikhaylova, M. (2020). Cytoskeletal makeup of the synapse: Shaft versus spine. *Cytoskeleton*, *77*(3–4), 55–64. https://doi.org/10.1002/cm.21583

Bucher, M., Niebling, S., Han, Y., Molodenskiy, D., Nia, F. H., Kreienkamp, H. J., Svergun, D., Kim, E., Kostyukova, A. S., Kreutz, M. R., & Mikhaylova, M. (2021). Autism-associated shank3 missense point mutations impact conformational fluctuations and protein turnover at synapses. *ELife*, *10*, 1–31. https://doi.org/10.7554/eLife.66165

Bulheller, B. M., Rodger, A., & Hirst, J. D. (2007). Circular and linear dichroism of proteins. *Physical Chemistry Chemical Physics*, *9*(17), 2020–2035. https://doi.org/10.1039/b615870f

Bussi, G., Donadio, D., & Parrinello, M. (2007). Canonical sampling through velocity rescaling. *Journal of Chemical Physics*, *126*(1). https://doi.org/10.1063/1.2408420

Cai, Q., Hosokawa, T., Zeng, M., Hayashi, Y., & Zhang, M. (2020). Shank3 Binds to and Stabilizes the Active Form of Rap1 and HRas GTPases via Its NTD-ANK Tandem with Distinct Mechanisms. *Structure*, *28*(3), 290-300.e4. https://doi.org/10.1016/j.str.2019.11.018

Chattopadhyay, G., & Varadarajan, R. (2019). Facile measurement of protein stability and folding kinetics using a nano differential scanning fluorimeter. *Protein Science*, *28*(6), 1127–1134. https://doi.org/10.1002/pro.3622

Chen, X., Winters, C., Azzam, R., Li, X., Galbraith, J. A., Leapman, R. D., & Reese, T. S. (2008). Organization of the core structure of the postsynaptic density. *Proceedings of the National Academy of Sciences of the United States of America*, *105*(11), 4453–4458. https://doi.org/10.1073/pnas.0800897105

Chubykin, A. A., Atasoy, D., Etherton, M. R., Brose, N., Kavalali, E. T., Gibson, J. R., & Südhof, T. C. (2007). Activity-Dependent Validation of Excitatory versus Inhibitory Synapses by Neuroligin-1 versus Neuroligin-2. *Neuron*, *54*(6), 919–931. https://doi.org/10.1016/j.neuron.2007.05.029

Citri, A., & Malenka, R. C. (2008). Synaptic plasticity: Multiple forms, functions, and mechanisms. *Neuropsychopharmacology*, *33*(1), 18–41. https://doi.org/10.1038/sj.npp.1301559

Comoletti, D., Grishaev, A., Whitten, A. E., Tsigelny, I., Taylor, P., & Trewhella, J. (2007). Synaptic Arrangement of the Neuroligin/β-Neurexin Complex Revealed by X-Ray and Neutron Scattering. *Structure*, *15*(6), 693–705. https://doi.org/10.1016/j.str.2007.04.010

Cox, J., Matic, I., Hilger, M., Nagaraj, N., Selbach, M., Olsen, J. V., & Mann, M. (2009). A practical guide to the MaxQuant computational platform for SILAC-based quantitative proteomics. *Nature Protocols*, *4*(5), 698–705. https://doi.org/10.1038/nprot.2009.36

Creson, T. K., Rojas, C., Hwaun, E., Vaissiere, T., Kilinc, M., Jimenez-Gomez, A., Holder, J. L., Tang, J., Colgin, L. L., Miller, C. A., & Rumbaugh, G. (2019). Re-expression of SynGAP protein in adulthood improves translatable measures of brain function and behavior. *ELife*, *8*, 1–19. https://doi.org/10.7554/eLife.46752

Darden, T., York, D., & Pedersen, L. (1993). Particle mesh Ewald: An N·log(N) method for Ewald sums in large systems. *The Journal of Chemical Physics*, *98*(12), 10089–10092. https://doi.org/10.1063/1.464397

De Rubeis, S., Siper, P. M., Durkin, A., Weissman, J., Muratet, F., Halpern, D., Trelles, M. D. P., Frank, Y., Lozano, R., Wang, A. T., Holder, J. L., Betancur, C., Buxbaum, J. D., & Kolevzon, A. (2018). Delineation of the genetic and clinical spectrum of Phelan-McDermid syndrome caused by SHANK3 point mutations. *Molecular Autism*, *9*(1), 1–20. https://doi.org/10.1186/s13229-018-0205-9

Dieterich, D. C., Hodas, J. J. L., Gouzer, G., Shadrin, I. Y., Ngo, J. T., Triller, A., Tirrell, D. A., & Schuman, E. M. (2010). In situ visualization and dynamics of newly synthesized proteins in rat hippocampal neurons. *Nature Neuroscience*, *13*(7), 897–905. https://doi.org/10.1038/nn.2580

Dolphin, A. C., & Lee, A. (2020). Presynaptic calcium channels: specialized control of synaptic neurotransmitter release. *Nature Reviews Neuroscience*, *21*(4), 213–229. https://doi.org/10.1038/s41583-020-0278-2

Dosemeci, A., Weinberg, R. J., Reese, T. S., & Tao-Cheng, J. H. (2016). The postsynaptic density: There is more than meets the eye. *Frontiers in Synaptic Neuroscience*, *8*(AUG), 1–8. https://doi.org/10.3389/fnsyn.2016.00023

Duan, Y., Wu, C., Chowdhury, S., Lee, M. C., Xiong, G., Zhang, W., Yang, R., Cieplak, P., Luo, R., Lee, T., Caldwell, J., Wang, J., & Kollman, P. (2003). A Point-Charge Force Field for Molecular Mechanics Simulations of Proteins Based on Condensed-Phase Quantum Mechanical Calculations. *Journal of Computational Chemistry*, *24*(16), 1999–2012. https://doi.org/10.1002/jcc.10349

Duda, D. M., van Waardenburg, R. C. A. M., Borg, L. A., McGarity, S., Nourse, A., Waddell, M. B., Bjornsti, M. A., & Schulman, B. A. (2007). Structure of a SUMO-binding-motif Mimic Bound to Smt3p-Ubc9p: Conservation of a Non-covalent Ubiquitin-like Protein-E2 Complex as a Platform for Selective Interactions within a SUMO Pathway. *Journal of Molecular Biology*, *369*(3), 619–630. https://doi.org/10.1016/j.jmb.2007.04.007

Durand, C. M., Perroy, J., Loll, F., Perrais, D., Fagni, L., Bourgeron, T., Montcouquiol, M., & Sans, N. (2012). SHANK3 mutations identified in autism lead to modification of dendritic spine morphology via an actin-dependent mechanism. *Molecular Psychiatry*, *17*(1), 71–84. https://doi.org/10.1038/mp.2011.57

Durand, Christelle M., Betancur, C., Boeckers, T. M., Bockmann, J., Chaste, P., Fauchereau, F., Nygren, G., Rastam, M., Gillberg, I. C., Anckarsäter, H., Sponheim, E., Goubran-Botros, H., Delorme, R., Chabane, N., Mouren-Simeoni, M. C., De Mas, P., Bieth, E., Rogé, B., Héron, D., … Bourgeron, T. (2007). Mutations in the gene encoding the synaptic scaffolding protein SHANK3 are associated with autism spectrum disorders. *Nature Genetics*, *39*(1), 25–27. https://doi.org/10.1038/ng1933

Ebert, D. H., & Greenberg, M. E. (2013). Activity-dependent neuronal signalling and autism spectrum disorder. *Nature*, *493*(7432), 327–337. https://doi.org/10.1038/nature11860

Essmann, U., Perera, L., Berkowitz, M. L., Darden, T., Lee, H., & Pedersen, L. G. (1995). A smooth particle mesh Ewald method. *The Journal of Chemical Physics*, *103*(19), 8577–8593. https://doi.org/10.1063/1.470117

Fakhoury, M. (2015). Autistic spectrum disorders: A review of clinical features, theories and diagnosis. *International Journal of Developmental Neuroscience*, *43*, 70–77. https://doi.org/10.1016/j.ijdevneu.2015.04.003

Fejtova, A., & Gundelfinger, E. D. (2006). Molecular organization and assembly of the presynaptic active zone of neurotransmitter release. *Results and Problems in Cell Differentiation*, *43*(June), 49–68. https://doi.org/10.1007/400_012

Feng, W., & Zhang, M. (2009). Organization and dynamics of PDZ-domain-related supramodules in the postsynaptic density. *Nature Reviews Neuroscience*, *10*(2), 87–99. https://doi.org/10.1038/nrn2540

Franke, D., Petoukhov, M. V., Konarev, P. V., Panjkovich, A., Tuukkanen, A., Mertens, H. D. T., Kikhney, A. G., Hajizadeh, N. R., Franklin, J. M., Jeffries, C. M., & Svergun, D. I. (2017). ATSAS 2.8: A comprehensive data analysis suite for small-angle scattering from macromolecular solutions. *Journal of Applied Crystallography*, *50*, 1212–1225. https://doi.org/10.1107/S1600576717007786

Gamache, T. R., Araki, Y., & Huganir, R. L. (2020). Twenty years of syngap research: From synapses to cognition. *Journal of Neuroscience*, *40*(8), 1596–1605. https://doi.org/10.1523/JNEUROSCI.0420-19.2020

Gauthier, J., Champagne, N., Lafrenière, R. G., Xiong, L., Spiegelman, D., Brustein, E., Lapointe, M., Peng, H., Côté, M., Noreau, A., Hamdan, F. F., Addington, A. M., Rapoport, J. L., DeLisi, L. E., Krebs, M. O., Joober, R., Fathalli, F., Mouaffak, F., Haghighi, A. P., … Gourion, D. (2010). De novo mutations in the gene encoding the synaptic scaffolding protein SHANK3 in patients ascertained for schizophrenia. *Proceedings of the National Academy of Sciences of the United States of America*, *107*(17), 7863–7868. https://doi.org/10.1073/pnas.0906232107

Gauthier, J., Spiegelman, D., Piton, A., Lafreniére, R. G., Laurent, S., St-Onge, J., Lapointe, L., Hamdan, F. F., Cossette, P., Mottron, L., Fombonne, É., Joober, R., Marineau, C., Drapeau, P., & Rouleau, G. A. (2009). Novel de novo SHANK3 mutation in autistic patients. *American Journal of Medical Genetics, Part B: Neuropsychiatric Genetics*, *150*(3), 421–424. https://doi.org/10.1002/ajmg.b.30822

Gogolla, N., LeBlanc, J. J., Quast, K. B., Südhof, T. C., Fagiolini, M., & Hensch, T. K. (2009). Common circuit defect of excitatory-inhibitory balance in mouse models of autism. *Journal of Neurodevelopmental Disorders*, *1*(2), 172–181. https://doi.org/10.1007/s11689-009-9023-x

Grabrucker, A. M. (2014). A role for synaptic zinc in ProSAP/Shank PSD scaffold malformation in autism spectrum disorders. *Developmental Neurobiology*, *74*(2), 136–146. https://doi.org/10.1002/dneu.22089

Greenfield, N. J. (2007a). Analysis of the kinetics of folding of proteins and peptides using circular dichroism. *Nature Protocols*, *1*(6), 2891–2899. https://doi.org/10.1038/nprot.2006.244

Greenfield, N. J. (2007b). Determination of the folding of proteins as a function of denaturants, osmolytes or ligands using circular dichroism. *Nature Protocols*, *1*(6), 2733–2741. https://doi.org/10.1038/nprot.2006.229

Greenfield, N. J. (2007c). Using circular dichroism collected as a function of temperature to determine the thermodynamics of protein unfolding and binding interactions. *Nature Protocols*, *1*(6), 2527–2535. https://doi.org/10.1038/nprot.2006.204

Greenfield, N. J. (2007d). Using circular dichroism spectra to estimate protein secondary structure. *Nature Protocols*, *1*(6), 2876–2890. https://doi.org/10.1038/nprot.2006.202

Guang, S., Pang, N., Deng, X., Yang, L., He, F., Wu, L., Chen, C., Yin, F., & Peng, J. (2018). Synaptopathology involved in autism spectrum disorder. *Frontiers in Cellular Neuroscience*, *12*(December), 1–16. https://doi.org/10.3389/fncel.2018.00470

Guilmatre, A., Huguet, G., Delorme, R., & Bourgeron, T. (2014). The emerging role of SHANK genes in neuropsychiatric disorders. *Developmental Neurobiology*, *74*(2), 113–122. https://doi.org/10.1002/dneu.22128

Han, K., Holder, J. L., Schaaf, C. P., Lu, H., Chen, H., Kang, H., Tang, J., Wu, Z., Hao, S., Cheung, S. W., Yu, P., Sun, H., Breman, A. M., Patel, A., Lu, H. C., & Zoghbi, H. Y. (2013). SHANK3 overexpression causes manic-like behaviour with unique pharmacogenetic properties. *Nature*, *503*(7474), 72–77. https://doi.org/10.1038/nature12630

Han, Q., Kim, Y. H., Wang, X., Liu, D., Zhang, Z. J., Bey, A. L., Lay, M., Chang, W., Berta, T., Zhang, Y., Jiang, Y. H., & Ji, R. R. (2016). SHANK3 Deficiency Impairs Heat Hyperalgesia and TRPV1 Signaling in Primary Sensory Neurons. *Neuron*, *92*(6), 1279–1293. https://doi.org/10.1016/j.neuron.2016.11.007

Hassani Nia, F., & Kreienkamp, H. J. (2018). Functional Relevance of Missense Mutations Affecting the N-Terminal Part of Shank3 Found in Autistic Patients. *Frontiers in Molecular Neuroscience*, *11*(August), 1–6. https://doi.org/10.3389/fnmol.2018.00268

Hassani Nia, F., Woike, D., Martens, V., Klüssendorf, M., Hönck, H. H., Harder, S., & Kreienkamp, H. J. (2020). Targeting of δ-catenin to postsynaptic sites through interaction with the Shank3 N-terminus. *Molecular Autism*, *11*(1), 1–17. https://doi.org/10.1186/s13229-020-00385-8

Hess, B., Bekker, H., Berendsen, H. J. C., & Fraaije, J. G. E. M. (1997). LINCS: A Linear Constraint Solver for molecular simulations. *Journal of Computational Chemistry*, *18*(12), 1463–1472. https://doi.org/10.1002/(SICI)1096-987X(199709)18:12<1463::AID-JCC4>3.0.CO;2-H

Hess, B., Kutzner, C., Van Der Spoel, D., & Lindahl, E. (2008). GROMACS 4: Algorithms for highly efficient, load-balanced, and scalable molecular simulation. *Journal of Chemical Theory and Computation*, *4*(3), 435–447. https://doi.org/10.1021/ct700301q

Higley, M. J., & Sabatini, B. L. (2012). Calcium signaling in dendritic spines. *Cold Spring Harbor Perspectives in Biology*, *4*(4). https://doi.org/10.1101/cshperspect.a005686

Hijikata, A., Tsuji, T., Shionyu, M., & Shirai, T. (2017). Decoding disease-causing mechanisms of missense mutations from supramolecular structures. *Scientific Reports*, *7*(1), 1–8. https://doi.org/10.1038/s41598-017-08902-1

Hollingsworth, S. A., & Dror, R. O. (2018). Molecular Dynamics Simulation for All. *Neuron*, *99*(6), 1129–1143. https://doi.org/10.1016/j.neuron.2018.08.011

Humphrey, W., Dalke, A., & Schulten, K. (1996). VMD: Visual Molecular Dynamics. *Journal of Molecular Graphics*, *14*(October 1995), 33–38. https://www.tapbiosystems.com/tap/products/index.htm

Iossifov, I., O'Roak, B. J., Sanders, S. J., Ronemus, M., Krumm, N., Levy, D., Stessman, H. A., Witherspoon, K. T., Vives, L., Patterson, K. E., Smith, J. D., Paeper, B., Nickerson, D. A., Dea, J., Dong, S., Gonzalez, L. E., Mandell, J. D., Mane, S. M., Murtha, M. T., … Wigler, M. (2014). The contribution of de novo coding mutations to autism spectrum disorder. *Nature*, *515*(7526), 216–221. https://doi.org/10.1038/nature13908

Jeffries, C. M., Ilavsky, J., Martel, A., Hinrichs, S., Meyer, A., Pedersen, J. S., Sokolova, A. V., & Svergun, D. I. (2021). Small-angle X-ray and neutron scattering. In *Nature Reviews Methods Primers* (Vol. 1, Issue 1). Springer US. https://doi.org/10.1038/s43586-021-00064-9

Jiang, Y. hui, & Ehlers, M. D. (2013). Modeling Autism by SHANK Gene Mutations in Mice. *Neuron*, *78*(1), 8–27. https://doi.org/10.1016/j.neuron.2013.03.016

Jimenez-Gomez, A., Niu, S., Andujar-Perez, F., McQuade, E. A., Balasa, A., Huss, D., Coorg, R., Quach, M., Vinson, S., Risen, S., & Holder, J. L. (2019). Phenotypic characterization of individuals with SYNGAP1 pathogenic variants reveals a potential correlation between posterior dominant rhythm and developmental progression. *Journal of Neurodevelopmental Disorders*, *11*(1), 1–11. https://doi.org/10.1186/s11689-019-9276-y

Kandel, E. R. (2013). *Principles of neural science* (5th ed.). McGraw-Hill Medical.

Kelly, S. M., Jess, T. J., & Price, N. C. (2005). How to study proteins by circular dichroism. *Biochimica et Biophysica Acta - Proteins and Proteomics*, *1751*(2), 119–139. https://doi.org/10.1016/j.bbapap.2005.06.005

Kennedy, M. B. (2016). Synaptic signaling in learning and memory. *Cold Spring Harbor Perspectives in Biology*, *8*(2), 1–16. https://doi.org/10.1101/cshperspect.a016824

Kim, E., & Sheng, M. (2004). PDZ domain proteins of synapses. *Nature Reviews Neuroscience*, *5*(10), 771–781. https://doi.org/10.1038/nrn1517

Klepeis, J. L., Lindorff-Larsen, K., Dror, R. O., & Shaw, D. E. (2009). Long-timescale molecular dynamics simulations of protein structure and function. *Current Opinion in Structural Biology*, *19*(2), 120–127. https://doi.org/10.1016/j.sbi.2009.03.004

Kotaleski, J. H., & Blackwell, K. T. (2010). Modelling the molecular mechanisms of synaptic plasticity using systems biology approaches. *Nature Reviews Neuroscience*, *11*(4), 239–251. https://doi.org/10.1038/nrn2807

Kucukkal, T. G., Petukh, M., Li, L., & Alexov, E. (2015). Structural and physico-chemical effects of disease and non-disease nsSNPs on proteins. *Current Opinion in Structural Biology*, *32*, 18–24. https://doi.org/10.1016/j.sbi.2015.01.003

Leblond, C. S., Nava, C., Polge, A., Gauthier, J., Huguet, G., Lumbroso, S., Giuliano, F., Stordeur, C., Depienne, C., Mouzat, K., Pinto, D., Howe, J., Lemière, N., Durand, C. M., Guibert, J., Ey, E., Toro, R., Peyre, H., Mathieu, A., … Bourgeron, T. (2014). Meta-analysis of SHANK Mutations in Autism Spectrum Disorders: A Gradient of Severity in Cognitive Impairments. *PLoS Genetics*, *10*(9). https://doi.org/10.1371/journal.pgen.1004580

Lee, J., Chung, C., Ha, S., Lee, D., Kim, D. Y., Kim, H., & Kim, E. (2015). Shank3-mutant mice lacking exon 9 show altered excitation/inhibition balance, enhanced rearing, and spatial memory deficit. *Frontiers in Cellular Neuroscience*, *9*(March), 1–14. https://doi.org/10.3389/fncel.2015.00094

Lee, Y., Kang, H., Lee, B., Zhang, Y., Kim, Y., Kim, S., Kim, W. K., & Han, K. (2017). Integrative analysis of brain region-specific Shank3 interactomes for understanding the heterogeneity of neuronal pathophysiology related to SHANK3 mutations. *Frontiers in Molecular Neuroscience*, *10*(April), 1–13. https://doi.org/10.3389/fnmol.2017.00110

Leterrier, C. (2018). The axon initial segment: An updated viewpoint. *Journal of Neuroscience*, *38*(9), 2135–2145. https://doi.org/10.1523/JNEUROSCI.1922-17.2018

Li, Z., & Hirst, J. D. (2017). Quantitative first principles calculations of protein circular dichroism in the near-ultraviolet. *Chemical Science*, *8*(6), 4318–4333. https://doi.org/10.1039/c7sc00586e

Liguori, L., Monticelli, M., Allocca, M., Mele, B. H., Lukas, J., Cubellis, M. V., & Andreotti, G. (2020). Pharmacological chaperones: A therapeutic approach for diseases caused by destabilizing missense mutations. *International Journal of Molecular Sciences*, *21*(2). https://doi.org/10.3390/ijms21020489

Lilja, J., Zacharchenko, T., Georgiadou, M., Jacquemet, G., De Franceschi, N., Peuhu, E., Hamidi, H., Pouwels, J., Martens, V., Nia, F. H., Beifuss, M., Boeckers, T., Kreienkamp, H. J., Barsukov, I. L., & Ivaska, J. (2017). SHANK proteins limit integrin activation by directly interacting with Rap1 and R-Ras. *Nature Cell Biology*, *19*(4), 292–305. https://doi.org/10.1038/ncb3487

Lim, S., Sala, C., Yoon, J., Park, S., Kuroda, S., Sheng, M., & Kim, E. (2001). Sharpin, a novel postsynaptic density protein that directly interacts with the shank family of proteins. *Molecular and Cellular Neuroscience*, *17*(2), 385–397. https://doi.org/10.1006/mcne.2000.0940

Lord, C., Brugha, T. S., Charman, T., Cusack, J., Dumas, G., Frazier, T., Jones, E. J. H., Jones, R. M., Pickles, A., State, M. W., Taylor, J. L., & Veenstra-VanderWeele, J. (2020). Autism spectrum disorder. *Nature Reviews Disease Primers*, *6*(1). https://doi.org/10.1038/s41572-019-0138-4

Luo, W., Zhang, C., Jiang, Y. H., & Brouwer, C. R. (2018). Systematic reconstruction of autism biology from massive genetic mutation profiles. *Science Advances*, *4*(4), 1–15. https://doi.org/10.1126/sciadv.1701799

Macgillavry, H. D., Kerr, J. M., Kassner, J., Frost, N. A., & Blanpied, T. A. (2016). Shank-cortactin interactions control actin dynamics to maintain flexibility of neuronal spines and synapses. *European Journal of Neuroscience*, *43*(2), 179–193. https://doi.org/10.1111/ejn.13129

MacGillavry, H. D., Song, Y., Raghavachari, S., & Blanpied, T. A. (2013). Nanoscale scaffolding domains within the postsynaptic density concentrate synaptic ampa receptors. *Neuron*, *78*(4), 615–622. https://doi.org/10.1016/j.neuron.2013.03.009

Mameza, M. G., Dvoretskova, E., Bamann, M., Hönck, H. H., Güler, T., Boeckers, T. M., Schoen, M., Verpelli, C., Sala, C., Barsukov, I., Dityatev, A., & Kreienkamp, H. J. (2013). SHANK3 gene mutations associated with autism facilitate ligand binding to the shank3 ankyrin repeat region. *Journal of Biological Chemistry*, *288*(37), 26697–26708. https://doi.org/10.1074/jbc.M112.424747

Manalastas-Cantos, K., Konarev, P. V., Hajizadeh, N. R., Kikhney, A. G., Petoukhov, M. V., Molodenskiy, D. S., Panjkovich, A., Mertens, H. D. T., Gruzinov, A., Borges, C., Jeffries, C. M., Svergun, D. I., & Franke, D. (2021). *ATSAS 3.0*: expanded functionality and new tools for small-angle scattering data analysis. *Journal of Applied Crystallography*, *54*(1), 54. https://doi.org/10.1107/S1600576720013412

Masland, R. H. (2004). Neuronal cell types. *Current Biology*, *14*(13), R497–R500. https://doi.org/10.1016/j.cub.2004.06.035

Mikhaylova, M., Bär, J., van Bommel, B., Schätzle, P., YuanXiang, P. A., Raman, R., Hradsky, J., Konietzny, A., Loktionov, E. Y., Reddy, P. P., Lopez-Rojas, J., Spilker, C., Kobler, O., Raza, S. A., Stork, O., Hoogenraad, C. C., & Kreutz, M. R. (2018). Caldendrin Directly Couples Postsynaptic Calcium Signals to Actin Remodeling in Dendritic Spines. *Neuron*, *97*(5), 1110-1125.e14. https://doi.org/10.1016/j.neuron.2018.01.046

Moessner, R., Marshall, C. R., Sutcliffe, J. S., Skaug, J., Pinto, D., Vincent, J., Zwaigenbaum, L., Fernandez, B., Roberts, W., Szatmari, P., & Scherer, S. W. (2007). Contribution of SHANK3 mutations to autism spectrum disorder. *American Journal of Human Genetics*, *81*(6), 1289–1297. https://doi.org/10.1086/522590

Monteiro, P., & Feng, G. (2017). SHANK proteins: Roles at the synapse and in autism spectrum disorder. *Nature Reviews Neuroscience*, *18*(3), 147–157. https://doi.org/10.1038/nrn.2016.183

Naisbitt, S., Eunjoon, K., Tu, J. C., Xiao, B., Sala, C., Valtschanoff, J., Weinberg, R. J., Worley, P. F., & Sheng, M. (1999). Shank, a novel family of postsynaptic density proteins that binds to the NMDA receptor/PSD-95/GKAP complex and cortactin. *Neuron*, *23*(3), 569–582. https://doi.org/10.1016/S0896-6273(00)80809-0

Narayan, A., Bhattacharjee, K., & Naganathan, A. N. (2019). Thermally versus Chemically Denatured Protein States. *Biochemistry*, *58*(21), 2519–2523. https://doi.org/10.1021/acs.biochem.9b00089

Nelson, S. B., & Valakh, V. (2015). Excitatory/Inhibitory Balance and Circuit Homeostasis in Autism Spectrum Disorders. *Neuron*, *87*(4), 684–698. https://doi.org/10.1016/j.neuron.2015.07.033

Nosé, S., & Klein, M. L. (1983). Constant pressure molecular dynamics for molecular systems. *Molecular Physics*, *50*(5), 1055–1076. https://doi.org/10.1080/00268978300102851

Nowak, L. M., Young, A. B., & Macdonald, R. L. (1982). GABA and bicuculline actions on mouse spinal cord and cortical neurons in cell culture. *Brain Research*, *244*(1), 155–164. https://doi.org/10.1016/0006-8993(82)90913-1

Obashi, K., Taraska, J. W., & Okabe, S. (2021). The role of molecular diffusion within dendritic spines in synaptic function. *Journal of General Physiology*, *153*(4), 1–13. https://doi.org/10.1085/jgp.202012814

Ozkan, E. D., Creson, T. K., Kramár, E. A., Rojas, C., Seese, R. R., Babyan, A. H., Shi, Y., Lucero, R., Xu, X., Noebels, J. L., Miller, C. A., Lynch, G., & Rumbaugh, G. (2014). Reduced cognition in Syngap1 mutants is caused by isolated damage within developing forebrain excitatory neurons. *Neuron*, *82*(6), 1317–1333. https://doi.org/10.1016/j.neuron.2014.05.015

Parrinello, M., & Rahman, A. (1981). Polymorphic transitions in single crystals: A new molecular dynamics method. *Journal of Applied Physics*, *52*(12), 7182–7190. https://doi.org/10.1063/1.328693

Peça, J., Feliciano, C., Ting, J. T., Wang, W., Wells, M. F., Venkatraman, T. N., Lascola, C. D., Fu, Z., & Feng, G. (2011). Shank3 mutant mice display autistic-like behaviours and striatal dysfunction. *Nature*, *472*(7344), 437–442. https://doi.org/10.1038/nature09965

Perfitt, T. L., Wang, X., Dickerson, M. T., Stephenson, J. R., Nakagawa, T., Jacobson, D. A., & Colbran, R. J. (2020). Neuronal L-type calcium channel signaling to the nucleus requires a novel CaMKIIα-SHANK3 interaction. *Journal of Neuroscience*, *40*(10), 2000–2014. https://doi.org/10.1523/JNEUROSCI.0893-19.2020

Petoukhov, M. V., Franke, D., Shkumatov, A. V., Tria, G., Kikhney, A. G., Gajda, M., Gorba, C., Mertens, H. D. T., Konarev, P. V., & Svergun, D. I. (2012). New developments in the ATSAS program package for small-angle scattering data analysis. *Journal of Applied Crystallography*, *45*(2), 342–350. https://doi.org/10.1107/S0021889812007662

Petoukhov, M. V., Konarev, P. V., Kikhney, A. G., & Svergun, D. I. (2007). ATSAS 2.1 - Towards automated and web-supported small-angle scattering data analysis. *Journal of Applied Crystallography*, *40*(SUPPL. 1), 223–228. https://doi.org/10.1107/S0021889807002853

Pettersen, E. F., Goddard, T. D., Huang, C. C., Couch, G. S., Greenblatt, D. M., Meng, E. C., & Ferrin, T. E. (2004). UCSF Chimera - A visualization system for exploratory research and analysis. *Journal of Computational Chemistry*, *25*(13), 1605–1612. https://doi.org/10.1002/jcc.20084

Ponna, S. K., Myllykoski, M., Boeckers, T. M., & Kursula, P. (2017). Structure of an unconventional SH3 domain from the postsynaptic density protein Shank3 at ultrahigh resolution. *Biochemical and Biophysical Research Communications*, *490*(3), 806–812. https://doi.org/10.1016/j.bbrc.2017.06.121

Ponna, S. K., Ruskamo, S., Myllykoski, M., Keller, C., Boeckers, T. M., & Kursula, P. (2018). Structural basis for PDZ domain interactions in the post-synaptic density scaffolding protein Shank3. *Journal of Neurochemistry*, *145*(6), 449–463. https://doi.org/10.1111/jnc.14322

Pronk, S., Páll, S., Schulz, R., Larsson, P., Bjelkmar, P., Apostolov, R., Shirts, M. R., Smith, J. C., Kasson, P. M., Van Der Spoel, D., Hess, B., & Lindahl, E. (2013). GROMACS 4.5: A high-throughput and highly parallel open source molecular simulation toolkit. *Bioinformatics*, *29*(7), 845–854. https://doi.org/10.1093/bioinformatics/btt055

Qin, L., Ma, K., Wang, Z. J., Hu, Z., Matas, E., Wei, J., & Yan, Z. (2018). Social deficits in Shank3-deficient mouse models of autism are rescued by histone deacetylase (HDAC) inhibition. *Nature Neuroscience*, *21*(4), 564–575. https://doi.org/10.1038/s41593-018-0110-8

Reim, D., Distler, U., Halbedl, S., Verpelli, C., Sala, C., Bockmann, J., Tenzer, S., Boeckers, T. M., & Schmeisser, M. J. (2017). Proteomic analysis of post-synaptic density fractions from Shank3 mutant mice reveals brain region specific changes relevant to autism spectrum disorder. *Frontiers in Molecular Neuroscience*, *10*(February), 1–10. https://doi.org/10.3389/fnmol.2017.00026

Richards, S. E. V., & Van Hooser, S. D. (2018). Neural architecture: From cells to circuits. *Journal of Neurophysiology*, *120*(2), 854–866. https://doi.org/10.1152/jn.00044.2018

Rollenhagen, A., & Lübke, J. H. R. (2006). The morphology of excitatory central synapses: From structure to function. *Cell and Tissue Research*, *326*(2), 221–237. https://doi.org/10.1007/s00441-006-0288-z

Roussignol, G., Ango, F., Romorini, S., Tu, J. C., Sala, C., Worley, P. F., Bockaert, J., & Fagni, L. (2005). Shank expression is sufficient to induce functional dendritic spine synapses in aspiny neurons. *Journal of Neuroscience*, *25*(14), 3560–3570. https://doi.org/10.1523/JNEUROSCI.4354-04.2005

Royer, C. A. (2006). Probing Protein Folding and Conformational Transitions with Fluorescence. *Chemical Reviews*, 1769–1784. https://doi.org/10.1021/cr0404390

Sakai, Y., Shaw, C. A., Dawson, B. C., Dugas, D. V., Al-Mohtaseb, Z., Hill, D. E., & Zoghbi, H. Y. (2011). Protein interactome reveals converging molecular pathways among autism disorders. *Science Translational Medicine*, *3*(86). https://doi.org/10.1126/scitranslmed.3002166

Sala, C., Vicidomini, C., Bigi, I., Mossa, A., & Verpelli, C. (2015). Shank synaptic scaffold proteins: Keys to understanding the pathogenesis of autism and other synaptic disorders. *Journal of Neurochemistry*, *135*(5), 849–858. https://doi.org/10.1111/jnc.13232

Salomaa, S. I., Miihkinen, M., Kremneva, E., Paatero, I., Lilja, J., Jacquemet, G., Vuorio, J., Antenucci, L., Kogan, K., Hassani Nia, F., Hollos, P., Isomursu, A., Vattulainen, I., Coffey, E. T., Kreienkamp, H.-J., Lappalainen, P., & Ivaska, J. (2021). SHANK3 conformation regulates direct actin binding and crosstalk with Rap1 signaling. *Current Biology*, 1–15. https://doi.org/10.1016/j.cub.2021.09.022

Santini, E., & Klann, E. (2014). Reciprocal signaling between translational control pathways and synaptic proteins in autism spectrum disorders. *Science Signaling*, *7*(349), 1–11. https://doi.org/10.1126/scisignal.2005832

Santoro, M. M., & Bolen, D. W. (1988). Unfolding Free Energy Changes Determined by the Linear Extrapolation Method. 1. Unfolding of Phenylmethanesulfonyl a-Chymotrypsin Using Different Denaturants. *Biochemistry*, *27*(21), 8063–8068. https://doi.org/10.1021/bi00421a014

Schwertman, P., Lagarou, A., Dekkers, D. H. W., Raams, A., Van Der Hoek, A. C., Laffeber, C., Hoeijmakers, J. H. J., Demmers, J. A. A., Fousteri, M., Vermeulen, W., & Marteijn, J. A. (2012). UV-sensitive syndrome protein UVSSA recruits USP7 to regulate transcription-coupled repair. *Nature Genetics*, *44*(5), 598–602. https://doi.org/10.1038/ng.2230

Sheng, M., & Kim, E. (2011). The postsynaptic organization of synapses. *Cold Spring Harbor Perspectives in Biology*, *3*(12), 1–20. https://doi.org/10.1101/cshperspect.a005678

Sheng, M., & Kim, M. J. (2002). Postsynaptic signaling and plasticity mechanisms. *Science*, *298*(5594), 776–780. https://doi.org/10.1126/science.1075333

Singh, S. K., & Eroglu, C. (2013). Neuroligins provide molecular links between syndromic and nonsyndromic autism. *Science Signaling*, *6*(283), 2–6. https://doi.org/10.1126/scisignal.2004102

Soler, J., Fañanás, L., Parellada, M., Krebs, M. O., Rouleau, G. A., & Fatjó-Vilas, M. (2018). Genetic variability in scaffolding proteins and risk for schizophrenia and autism-spectrum disorders: A systematic review. *Journal of Psychiatry and Neuroscience*, *43*(4), 223–244. https://doi.org/10.1503/jpn.170066

Soykan, T., Schneeberger, D., Tria, G., Buechner, C., Bader, N., Svergun, D., Tessmer, I., Poulopoulos, A., Papadopoulos, T., Varoqueaux, F., Schindelin, H., & Brose, N. (2014). A conformational switch in collybistin determines the differentiation of inhibitory postsynapses. *The EMBO Journal*, *33*(18), 2113–2133. https://doi.org/10.15252/embj.201488143

Spruston, N. (2008). Pyramidal neurons: Dendritic structure and synaptic integration. *Nature Reviews Neuroscience*, *9*(3), 206–221. https://doi.org/10.1038/nrn2286

Stefl, S., Nishi, H., Petukh, M., Panchenko, A. R., & Alexov, E. (2013). Molecular mechanisms of disease-causing missense mutations. *Journal of Molecular Biology*, *425*(21), 3919–3936. https://doi.org/10.1016/j.jmb.2013.07.014

Stephenson, J. R., Wang, X., Perfitt, T. L., Parrish, W. P., Shonesy, B. C., Marks, C. R., Mortlock, D. P., Nakagawa, T., Sutcliffe, J. S., & Colbran, R. J. (2017). A novel human CAMK2a mutation disrupts dendritic morphology and synaptic transmission, and causes ASD-related behaviors. *Journal of Neuroscience*, *37*(8), 2216–2233. https://doi.org/10.1523/JNEUROSCI.2068-16.2017

Strucksberg, K. H., Rosenkranz, T., & Fitter, J. (2007). Reversible and irreversible unfolding of multi-domain proteins. *Biochimica et Biophysica Acta - Proteins and Proteomics*, *1774*(12), 1591–1603. https://doi.org/10.1016/j.bbapap.2007.09.005

Svergun, D. I. (1992). Determination of the regularization parameter in indirect-transform methods using perceptual criteria. *Journal of Applied Crystallography*, *25*(pt 4), 495–503. https://doi.org/10.1107/S0021889892001663

Tao, Y. X., & Conn, P. M. (2018). Pharmacoperones as novel therapeutics for diverse protein conformational diseases. *Physiological Reviews*, *98*(2), 697–725. https://doi.org/10.1152/physrev.00029.2016

Tatti, R., Haley, M. S., Swanson, O. K., Tselha, T., & Maffei, A. (2017). Neurophysiology and Regulation of the Balance Between Excitation and Inhibition in Neocortical Circuits. *Biological Psychiatry*, *81*(10), 821–831. https://doi.org/10.1016/j.biopsych.2016.09.017

Ting, J. T., Peça, J., & Feng, G. (2012). Functional consequences of mutations in postsynaptic scaffolding proteins and relevance to psychiatric disorders. *Annual Review of Neuroscience*, *35*, 49–71. https://doi.org/10.1146/annurev-neuro-062111-150442

Traynelis, S. F., Wollmuth, L. P., McBain, C. J., Menniti, F. S., Vance, K. M., Ogden, K. K., Hansen, K. B., Yuan, H., Myers, S. J., & Dingledine, R. (2010). Glutamate receptor ion channels: Structure, regulation, and function. *Pharmacological Reviews*, *62*(3), 405–496. https://doi.org/10.1124/pr.109.002451

Tria, G., Mertens, H. D. T., Kachala, M., & Svergun, D. I. (2015). Advanced ensemble modelling of flexible macromolecules using X-ray solution scattering. *IUCrJ*, *2*, 207–217. https://doi.org/10.1107/S205225251500202X

Tu, J. C., Xiao, B., Naisbitt, S., Yuan, J. P., Petralia, R. S., Brakeman, P., Doan, A., Aakalu, V. K., Lanahan, A. A., Sheng, M., & Worley, P. F. (1999). Coupling of mGluR/Homer and PSD-95 complexes by the Shank family of postsynaptic density proteins. *Neuron*, *23*(3), 583–592. https://doi.org/10.1016/S0896-6273(00)80810-7

Tuukkanen, A. T., Spilotros, A., & Svergun, D. I. (2017). Progress in small-angle scattering from biological solutions at high-brilliance synchrotrons. *IUCrJ*, *4*, 518–528. https://doi.org/10.1107/S2052252517008740

Uchino, S., Wada, H., Honda, S., Nakamura, Y., Ondo, Y., Uchiyama, T., Tsutsumi, M., Suzuki, E., Hirasawa, T., & Kohsaka, S. (2006). Direct interaction of post-synaptic density-95/Dlg/ZO-1 domain-containing synaptic molecule Shank3 with GluR1 α-amino-3-hydroxy-5-methyl-4-isoxazole propionic acid receptor. *Journal of Neurochemistry*, *97*(4), 1203–1214. https://doi.org/10.1111/j.1471-4159.2006.03831.x

van Bommel, B., Konietzny, A., Kobler, O., Bär, J., & Mikhaylova, M. (2019). F-actin patches associated with glutamatergic synapses control positioning of dendritic lysosomes. *The EMBO Journal*, *38*(15), 1–17. https://doi.org/10.15252/embj.2018101183

Varoqueaux, F., Aramuni, G., Rawson, R. L., Mohrmann, R., Missler, M., Gottmann, K., Zhang, W., Südhof, T. C., & Brose, N. (2006). Neuroligins Determine Synapse Maturation and Function. *Neuron*, *51*(6), 741–754. https://doi.org/10.1016/j.neuron.2006.09.003

Verpelli, C., Schmeisser, M. J., Sala, C., & Boeckers, T. M. (2012). Scaffold Proteins at the Postsynaptic Density. In M. R. Kreutz & C. Sala (Eds.), *Synaptic Plasticity: Dynamics, Development and Disease* (pp. 29–61). Springer Vienna. https://doi.org/10.1007/978-3-7091-0932-8_2

Vessey, J. P., & Karra, D. (2007). More than just synaptic building blocks: Scaffolding proteins of the post-synaptic density regulate dendritic patterning. *Journal of Neurochemistry*, *102*(2), 324–332. https://doi.org/10.1111/j.1471-4159.2007.04662.x

Vivian, J. T., & Callis, P. R. (2001). Mechanisms of tryptophan fluorescence shifts in proteins. *Biophysical Journal*, *80*(5), 2093–2109. https://doi.org/10.1016/S0006-3495(01)76183-8

Voglis, G., & Tavernarakis, N. (2006). The role of synaptic ion channels in synaptic plasticity. *EMBO Reports*, *7*(11), 1104–1110. https://doi.org/10.1038/sj.embor.7400830

Walkup, W. G., Mastro, T. L., Schenker, L. T., Vielmetter, J., Hu, R., Iancu, A., Reghunathan, M., Bannon, B. D., & Kennedy, M. B. (2016). A model for regulation by SynGAP-α1 of binding of synaptic proteins to PDZ-domain "Slots" in the postsynaptic density. *ELife*, *5*, 1–31. https://doi.org/10.7554/elife.16813

Wang, L., Adamski, C. J., Bondar, V. V., Craigen, E., Collette, J. R., Pang, K., Han, K., Jain, A., Y. Jung, S., Liu, Z., Sifers, R. N., Holder, J. L., & Zoghbi, H. Y. (2019). A kinome-wide RNAi screen identifies ERK2 as a druggable regulator of Shank3 stability. *Molecular Psychiatry*. https://doi.org/10.1038/s41380-018-0325-9

Wang, L., Pang, K., Han, K., Adamski, C. J., Wang, W., He, L., Lai, J. K., Bondar, V. V., Duman, J. G., Richman, R., Tolias, K. F., Barth, P., Palzkill, T., Liu, Z., Holder, J. L., & Zoghbi, H. Y. (2019). An autism-linked missense mutation in SHANK3 reveals the modularity of Shank3 function. *Molecular Psychiatry*. https://doi.org/10.1038/s41380-018-0324-x

Wang, Q., Chen, M., Schafer, N. P., Bueno, C., Song, S. S., Hudmon, A., Wolynes, P. G., Neal Waxham, M., & Cheung, M. S. (2019). Assemblies of calcium/calmodulin-dependent kinase II with actin and their dynamic regulation by calmodulin in dendritic spines. *Proceedings of the National Academy of Sciences of the United States of America*, *116*(38), 18937–18942. https://doi.org/10.1073/pnas.1911452116

Wang, X., McCoy, P. A., Rodriguiz, R. M., Pan, Y., Je, H. S., Roberts, A. C., Kim, C. J., Berrios, J., Colvin, J. S., Bousquet-Moore, D., Lorenzo, I., Wu, G., Weinberg, R. J., Ehlers, M. D., Philpot, B. D., Beaudet, A. L., Wetsel, W. C., & Jiang, Y. H. (2011). Synaptic dysfunction and abnormal behaviors in mice lacking major isoforms of Shank3. *Human Molecular Genetics*, *20*(15), 3093–3108. https://doi.org/10.1093/hmg/ddr212

Wang, X., Xu, Q., Bey, A. L., Lee, Y., & Jiang, Y. H. (2014). Transcriptional and functional complexity of Shank3 provides a molecular framework to understand the phenotypic heterogeneity of SHANK3 causing autism and Shank3 mutant mice. *Molecular Autism*, *5*(1), 1–14. https://doi.org/10.1186/2040-2392-5-30

Willatt, L., Cox, J., Barber, J., Cabanas, E. D., Collins, A., Donnai, D., FitzPatrick, D. R., Maher, E., Martin, H., Parnau, J., Pindar, L., Ramsay, J., Shaw-Smith, C., Sistermans, E. A., Tettenborn, M., Trump, D., De Vries, B. B. A., Walker, K., & Raymond, F. L. (2005). 3q29 microdeletion syndrome: Clinical and molecular characterization of a new syndrome. *American Journal of Human Genetics*, *77*(1), 154–160. https://doi.org/10.1086/431653

Xing, J., Kimura, H., Wang, C., Ishizuka, K., Kushima, I., Arioka, Y., Yoshimi, A., Nakamura, Y., Shiino, T., Oya-Ito, T., Takasaki, Y., Uno, Y., Okada, T., Iidaka, T., Aleksic, B., Mori, D., & Ozaki, N. (2016). Resequencing and association analysis of Six PSD-95-related genes as possible susceptibility genes for schizophrenia and autism spectrum disorders. *Scientific Reports*, *6*(December 2015), 1–8. https://doi.org/10.1038/srep27491

Yang, X., & Specht, C. G. (2019). Subsynaptic domains in super-resolution microscopy: The treachery of images. *Frontiers in Molecular Neuroscience*, *12*(July). https://doi.org/10.3389/fnmol.2019.00161

Yang, Y., Tao-Cheng, J. H., Bayer, K. U., Reese, T. S., & Dosemeci, A. (2013). Camkii-Mediated Phosphorylation Regulates Distributions of Syngap-α1 and -α2 at the Postsynaptic Density. *PLoS ONE*, *8*(8), 6–11. https://doi.org/10.1371/journal.pone.0071795

Yi, F., Danko, T., Botelho, S. C., Patzke, C., Pak, C., Wernig, M., & Südhof, T. C. (2016). Autism-associated SHANK3 haploinsufficiency causes Ih channelopathy in human neurons. *Science*, *352*(6286). https://doi.org/10.1126/science.aaf2669

Yoo, T., Cho, H., Park, H., Lee, J., & Kim, E. (2019). Shank3 Exons 14–16 Deletion in Glutamatergic Neurons Leads to Social and Repetitive Behavioral Deficits Associated With Increased Cortical Layer 2/3 Neuronal Excitability. *Frontiers in Cellular Neuroscience*, *13*(October), 1–17. https://doi.org/10.3389/fncel.2019.00458

Yoo, Y. E., Yoo, T., Lee, S., Lee, J., Kim, D., Han, H. M., Bae, Y. C., & Kim, E. (2019). Shank3 mice carrying the human q321r mutation display enhanced self-grooming, abnormal electroencephalogram patterns, and suppressed neuronal excitability and seizure susceptibility. *Frontiers in Molecular Neuroscience*, *12*(June), 1–23. https://doi.org/10.3389/fnmol.2019.00155

Yuste, R., & Bonhoeffer, T. (2004). Genesis of dendritic spines: Insights from ultrastructural and imaging studies. *Nature Reviews Neuroscience*, *5*(1), 24–34. https://doi.org/10.1038/nrn1300

Zeng, H., & Sanes, J. R. (2017). Neuronal cell-type classification: Challenges, opportunities and the path forward. *Nature Reviews Neuroscience*, *18*(9), 530–546. https://doi.org/10.1038/nrn.2017.85

Zhang, H., Maximov, A., Fu, Y., Xu, F., Tang, T. S., Tkatch, T., Surmeier, D. J., & Bezprozvanny, I. (2005). Association of Cav1.3 L-type calcium channels with shank. *Journal of Neuroscience*, *25*(5), 1037–1049. https://doi.org/10.1523/JNEUROSCI.4554-04.2005

Ziff, E. B. (1997). Enlightening the Postsynaptic Density. *Neuron*, *19*, 1163–1174. https://doi.org/10.1016/S0896-6273(00)80409-2

Zoghbi, H. Y., & Bear, M. F. (2012). Synaptic dysfunction in neurodevelopmental disorders associated with autism and intellectual disabilities. *Cold Spring Harbor Perspectives in Biology*, *4*(3). https://doi.org/10.1101/cshperspect.a009886

Appendix

Principal SAXS parameters

For each of the studied His$_6$-SUMO-SHANK3$^{(1-676)}$ variants, direct analysis of the 1D scattering profiles using the ATSAS 3.0.1 software package provided several structurally relevant parameters including the radius of gyration (R_g), molecular weight (MW) estimates as well as the maximum particle diameter (D_{max}). Values for R_g were determined by Guinier approximation in the very low angular range, MW estimates were obtained by a bayesian inference approach and D_{max} was derived from corresponding pair distance distribution functions (PDDFs). The table below provides an overview of these principal SAXS parameters.

Overview of principal SAXS parameters computed for His$_6$-SUMO-SHANK3$^{(1-676)}$ variants.

His$_6$-SUMO-SHANK3$^{(1-676)}$	conc (mg/ml)	R_g (nm)	MW (kDa)	D_{max} (nm)
WT	9.2	6.36 ± 0.02	185.8	30.16
	7	5.85 ± 0.02	157.1	28.00
	5	5.38 ± 0.02	138.2	24.00
	3	4.83 ± 0.03	113.7	19.00
	1	4.31 ± 0.04	101.1	16.00
	0.5	4.15 ± 0.07	83.1	15.00
	0*	4.18‡	85.65†	14.00
	4.85§	4.47‡	83.13†	17.00
R12C	8.1	6.36 ± 0.02	185.8	30.32
	6	5.61 ± 0.02	146.8	26.00
	4	5.14 ± 0.02	118.8	24.00
	2	4.54 ± 0.03	94.2	20.00
	1	4.31 ± 0.04	94.2	19.00
	0.5	4.17 ± 0.09	109.1	17.00
	0*	4.10‡	94.23†	13.75
	4.30§	4.31‡	85.65†	16.00
L68P	4.1	5.28 ± 0.02	113.7	23.00
	2	5.08 ± 0.03	118.8	20.00
	1	4.53 ± 0.05	109.1	19.00
	0.5	4.11 ± 0.10	109.1	15.00
	0*	4.56‡	83.13†	14.82
	2.30§	4.32‡	74.33†	15.60

* Extrapolated to infinite dilution

‡ Real space R_g from GNOM analysis

† The molecular weight estimation is based on bayesian inference (expected = 87,5 kDa)

§ Nominal concentrations calculated as average between concentrations of merged SAXS profiles

The Globally Harmonized System of Classification and Labeling of Chemicals (GHS)

The following figure shows the individual hazard class pictograms according to the GHS.

GHS01 Explosives	GHS02 Flammables	GHS03 Oxidizers
GHS04 Compressed Gases	GHS05 Corrosives	GHS06 Acute Toxicity
GHS07 Irritant	GHS08 Systemic health hazard	GHS09 Environmental hazard
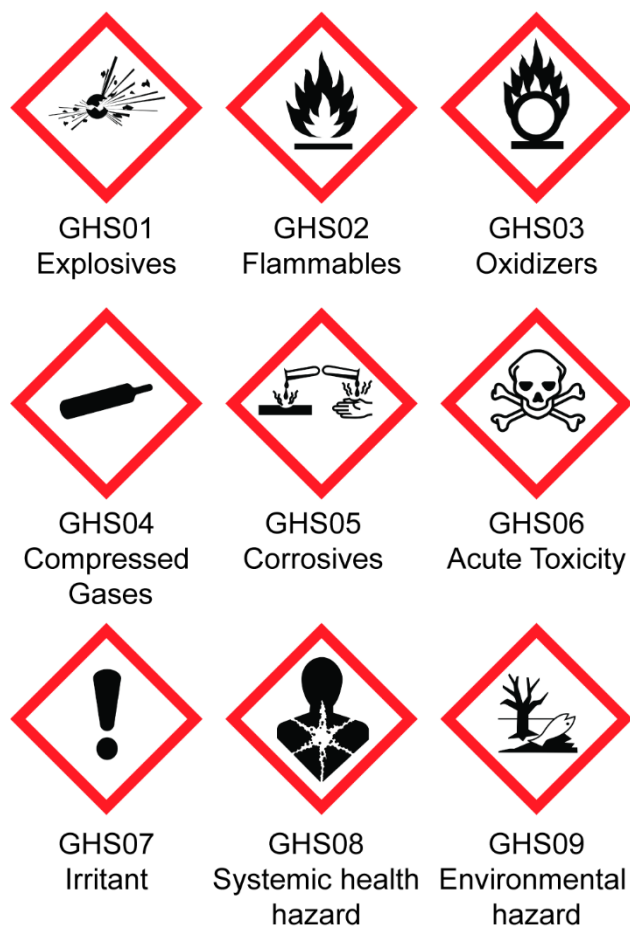
Hazard class pictograms according to the GHS. Shown are the individual pictograms, their respective numbers and signal words.

List of H- and P-statements according to the GHS

Tables listing the individual GHS hazard (H) and precautionary (P) statements are shown below.

List of GHS hazard statements.

Code	Hazard (H) Statement
H200	Unstable Explosive
H201	Explosive; mass explosion hazard
H202	Explosive; severe projection hazard
H203	Explosive; fire, blast or projection hazard

H204	Fire or projection hazard
H205	May mass explode in fire
H206	Fire, blast or projection hazard; increased risk of explosion if desensitizing agent is reduced
H207	Fire or projection hazard; increased risk of explosion if desensitizing agent is reduced
H208	Fire hazard; increased risk of explosion if desensitizing agent is reduced
H210	Very sensitive
H211	Maybe sensitive
H220	Extremely flammable gas
H221	Flammable gas
H222	Extremely flammable aerosol
H223	Flammable aerosol
H224	Extremely flammable liquid and vapor
H225	Highly Flammable liquid and vapor
H226	Flammable liquid and vapor
H227	Combustible liquid
H228	Flammable solid
H229	Pressurized container: may burst if heated
H230	May react explosively even in the absence of air
H231	May react explosively even in the absence of air at elevated pressure and/or temperature
H232	May ignite spontaneously if exposed to air
H240	Heating may cause an explosion
H241	Heating may cause a fire or explosion
H242	Heating may cause a fire
H250	Catches fire spontaneously if exposed to air
H251	Self-heating; may catch fire
H252	Self-heating in large quantities; may catch fire
H260	In contact with water releases flammable gases which may ignite spontaneously
H261	In contact with water releases flammable gas
H270	May cause or intensify fire; oxidizer
H271	May cause fire or explosion; strong Oxidizer
H272	May intensify fire; oxidizer
H280	Contains gas under pressure; may explode if heated
H281	Contains refrigerated gas; may cause cryogenic burns or injury
H282	Extremely flammable chemical under pressure: may explode if heated
H283	Flammable chemical under pressure: may explode if heated
H284	Chemical under pressure: may explode if heated
H290	May be corrosive to metals
H300	Fatal if swallowed
H301	Toxic if swallowed
H302	Harmful if swallowed
H303	May be harmful if swallowed
H304	May be fatal if swallowed and enters airways
H305	May be fatal if swallowed and enters airways
H310	Fatal in contact with skin
H311	Toxic in contact with skin
H312	Harmful in contact with skin
H313	May be harmful in contact with skin
H314	Causes severe skin burns and eye damage
H315	Causes skin irritation
H316	Causes mild skin irritation

H317	May cause an allergic skin reaction
H318	Causes serious eye damage
H319	Causes serious eye irritation
H320	Causes eye irritation
H330	Fatal if inhaled
H331	Toxic if inhaled
H332	Harmful if inhaled
H333	May be harmful if inhaled
H334	May cause allergy or asthma symptoms or breathing difficulties if inhaled
H335	May cause respiratory irritation
H336	May cause drowsiness or dizziness
H340	May cause genetic defects
H341	Suspected of causing genetic defects
H350	May cause cancer
H350i	May cause cancer by inhalation
H351	Suspected of causing cancer
H360	May damage fertility or the unborn child
H360F	May damage fertility
H360D	May damage the unborn child
H360FD	May damage fertility; May damage the unborn child
H360Fd	May damage fertility; Suspected of damaging the unborn child
H360Df	May damage the unborn child; Suspected of damaging fertility
H361	Suspected of damaging fertility or the unborn child
H361f	Suspected of damaging fertility
H361d	Suspected of damaging the unborn child
H361fd	Suspected of damaging fertility; Suspected of damaging the unborn child
H362	May cause harm to breast-fed children
H370	Causes damage to organs
H371	May cause damage to organs
H372	Causes damage to organs through prolonged or repeated exposure
H373	Causes damage to organs through prolonged or repeated exposure
H400	Very toxic to aquatic life
H401	Toxic to aquatic life
H402	Harmful to aquatic life
H410	Very toxic to aquatic life with long lasting effects
H411	Toxic to aquatic life with long lasting effects
H412	Harmful to aquatic life with long lasting effects
H413	May cause long lasting harmful effects to aquatic life
H420	Harms public health and the environment by destroying ozone in the upper atmosphere

List of GHS precautionary statements.

Code	Precautionary (P) Statement
P101	If medical advice is needed, have product container or label at hand.
P102	Keep out of reach of children.
P103	Read carefully and follow all instructions.
P201	Obtain special instructions before use.
P202	Do not handle until all safety precautions have been read and understood.

P203	Obtain, read and follow all safety instructions before use.
P210	Keep away from heat, hot surface, sparks, open flames and other ignition sources. No smoking.
P211	Do not spray on an open flame or other ignition source.
P212	Avoid heating under confinement or reduction of the desensitized agent.
P220	Keep away from clothing and other combustible materials.
P221	Take any precaution to avoid mixing with combustibles/...
P222	Do not allow contact with air.
P223	Do not allow contact with water.
P230	Keep wetted with ...
P231	Handle and store contents under inert gas/...
P232	Protect from moisture.
P233	Keep container tightly closed.
P234	Keep only in original container.
P235	Keep cool.
P236	Keep only in original packaging; Division ... in the transport configuration.
P240	Ground/bond container and receiving equipment.
P241	Use explosion-proof [electrical/ventilating/lighting/.../] equipment.
P242	Use only non-sparking tools.
P243	Take precautionary measures against static discharge.
P244	Keep valves and fittings free from oil and grease.
P250	Do not subject to grinding/shock/friction/...
P251	Do not pierce or burn, even after use.
P260	Do not breathe dust/fume/gas/mist/vapors/spray.
P261	Avoid breathing dust/fume/gas/mist/vapors/spray.
P262	Do not get in eyes, on skin, or on clothing.
P263	Avoid contact during pregnancy/while nursing.
P264	Wash hands [and …] thoroughly after handling.
P265	Do not touch eyes.
P270	Do not eat, drink or smoke when using this product.
P271	Use only outdoors or in a well-ventilated area.
P272	Contaminated work clothing should not be allowed out of the workplace.
P273	Avoid release to the environment.
P280	Wear protective gloves/protective clothing/eye protection/face protection/hearing protection/...
P281	Use personal protective equipment as required.
P282	Wear cold insulating gloves and either face shield or eye protection.
P283	Wear fire resistant or flame retardant clothing.
P284	[In case of inadequate ventilation] Wear respiratory protection.
P285	In case of inadequate ventilation wear respiratory protection.
P231+P232	Handle and store contents under inert gas/... Protect from moisture.
P264+P265	Wash hands [and …] thoroughly after handling. Do not touch eyes.

P235+P410	Keep cool. Protect from sunlight.
P301	IF SWALLOWED:
P302	IF ON SKIN:
P303	IF ON SKIN (or hair):
P304	IF INHALED:
P305	IF IN EYES:
P306	IF ON CLOTHING:
P307	IF exposed:
P308	IF exposed or concerned:
P309	IF exposed or if you feel unwell
P310	Immediately call a POISON CENTER or doctor/physician.
P311	Call a POISON CENTER or doctor/...
P312	Call a POISON CENTER or doctor/... if you feel unwell.
P313	Get medical advice/attention.
P314	Get medical advice/attention if you feel unwell.
P315	Get immediate medical advice/attention.
P316	Get emergency medical help immediately.
P317	Get emergency medical help.
P318	If exposed or concerned, get medical advice.
P319	Get medical help if you feel unwell.
P320	Specific treatment is urgent (see ... on this label).
P321	Specific treatment (see ... on this label).
P322	Specific measures (see ...on this label).
P330	Rinse mouth.
P331	Do NOT induce vomiting.
P332	IF SKIN irritation occurs:
P333	If skin irritation or rash occurs:
P334	Immerse in cool water [or wrap in wet bandages].
P335	Brush off loose particles from skin.
P336	Thaw frosted parts with lukewarm water. Do not rub affected area.
P337	If eye irritation persists:
P338	Remove contact lenses, if present and easy to do. Continue rinsing.
P340	Remove person to fresh air and keep comfortable for breathing.
P341	If breathing is difficult, remove victim to fresh air and keep at rest in a position comfortable for breathing.
P342	If experiencing respiratory symptoms:
P350	Gently wash with plenty of soap and water.
P351	Rinse cautiously with water for several minutes.
P352	Wash with plenty of water/...
P353	Rinse skin with water [or shower].
P354	Immediately rinse with water for several minutes.
P360	Rinse immediately contaminated clothing and skin with plenty of water before removing clothes.
P361	Take off immediately all contaminated clothing.
P362	Take off contaminated clothing.
P363	Wash contaminated clothing before reuse.
P364	And wash it before reuse.
P370	In case of fire:
P371	In case of major fire and large quantities:
P372	Explosion risk.

P373	DO NOT fight fire when fire reaches explosives.
P374	Fight fire with normal precautions from a reasonable distance.
P375	Fight fire remotely due to the risk of explosion.
P376	Stop leak if safe to do so.
P377	Leaking gas fire: Do not extinguish, unless leak can be stopped safely.
P378	Use ... to extinguish.
P380	Evacuate area.
P381	In case of leakage, eliminate all ignition sources.
P390	Absorb spillage to prevent material damage.
P391	Collect spillage.
P301+P310	IF SWALLOWED: Immediately call a POISON CENTER/doctor/...
P301+P312	IF SWALLOWED: call a POISON CENTER/doctor/... IF you feel unwell.
P301+P316	IF SWALLOWED: Get emergency medical help immediately.
P301+P317	IF SWALLOWED: Get medical help.
P301+P330+P331	IF SWALLOWED: Rinse mouth. Do NOT induce vomiting.
P302+P317	IF ON SKIN: Get medical help.
P302+P334	IF ON SKIN: Immerse in cool water or wrap in wet bandages.
P302+P335+P334	Brush off loose particles from skin. Immerse in cool water [or wrap in wet bandages].
P302+P350	IF ON SKIN: Gently wash with plenty of soap and water.
P302+P352	IF ON SKIN: wash with plenty of water/...
P302+P361+P354	IF ON SKIN: Take off Immediately all contaminated clothing. Immediately rinse with water for several minutes.
P303+P361+P353	IF ON SKIN (or hair): Take off immediately all contaminated clothing. Rinse SKIN with water [or shower].
P304+P312	IF INHALED: Call a POISON CENTER/doctor/... if you feel unwell.
P304+P317	IF INHALED: Get medical help.
P304+P340	IF INHALED: Remove person to fresh air and keep comfortable for breathing.
P304+P341	IF INHALED: If breathing is difficult, remove victim to fresh air and keep at rest in a position comfortable for breathing.
P305+P351+P338	IF IN EYES: Rinse cautiously with water for several minutes. Remove contact lenses if present and easy to do - continue rinsing.
P305+P354+P338	IF IN EYES: Immediately rinse with water for several minutes. Remove contact lenses if present and easy to do. Continue rinsing.
P306+P360	IF ON CLOTHING: Rinse Immediately contaminated CLOTHING and SKIN with plenty of water before removing clothes.
P308+P316	IF exposed or concerned: Get emergency medical help immediately.
P307+P311	IF exposed: call a POISON CENTER or doctor/physician.

P308+P311	IF exposed or concerned: Call a POISON CENTER/doctor/...
P308+P313	IF exposed or concerned: Get medical advice/attention.
P309+P311	IF exposed or if you feel unwell: call a POISON CENTER or doctor/physician.
P332+P313	IF SKIN irritation occurs: Get medical advice/attention.
P332+P317	If skin irritation occurs: Get medical help.
P333+P317	If skin irritation or rash occurs: Get medical help.
P336+P317	Immediately thaw frosted parts with lukewarm water. Do not rub affected area. Get medical help.
P337+P317	If eye irritation persists: Get medical help.
P342+P316	If experiencing respiratory symptoms: Get emergence medical help immediately.
P333+P313	IF SKIN irritation or rash occurs: Get medical advice/attention.
P335+P334	Brush off loose particles from skin. Immerse in cool water/wrap in wet bandages.
P337+P313	IF eye irritation persists: Get medical advice/attention.
P342+P311	IF experiencing respiratory symptoms: Call a POISON CENTER/doctor/...
P361+P364	Take off immediately all contaminated clothing and wash it before reuse.
P362+P364	Take off contaminated clothing and wash it before reuse.
P370+P376	in case of fire: Stop leak if safe to do so.
P370+P378	In case of fire: Use ... to extinguish.
P370+P380	In case of fire: Evacuate area.
P370+P380+P375	In case of fire: Evacuate area. Fight fire remotely due to the risk of explosion.
P371+P380+P375	In case of major fire and large quantities: Evacuate area. Fight fire remotely due to the risk of explosion.
P370+P372+P380+P373	In case of fire: Explosion risk. Evacuate area. DO NOT fight fire when fire reaches explosives.
P370+P380+P375[+P378]	In case of fire: Evacuate area. Fight fire remotely due to the risk of explosion. [Use…to extinguish].
P401	Store in accordance with ...
P402	Store in a dry place.
P403	Store in a well-ventilated place.
P404	Store in a closed container.
P405	Store locked up.
P406	Store in corrosive resistant/... container with a resistant inner liner.
P407	Maintain air gap between stacks or pallets.
P410	Protect from sunlight.
P411	Store at temperatures not exceeding ... °C/...°F.
P412	Do not expose to temperatures exceeding 50 °C/ 122 °F.
P413	Store bulk masses greater than ... kg/...lbs at temperatures not exceeding ... °C/...°F.
P420	Store separately.
P422	Store contents under ...
P402+P404	Store in a dry place. Store in a closed container.
P403+P233	Store in a well-ventilated place. Keep container tightly closed.

P403+P235	Store in a well-ventilated place. Keep cool.
P410+P403	Protect from sunlight. Store in a well-ventilated place.
P410+P412	Protect from sunlight. Do not expose to temperatures exceeding 50 °C/122°F.
P411+P235	Store at temperatures not exceeding ... °C/...°F. Keep cool.
P501	Dispose of contents/container to ...
P502	Refer to manufacturer or supplier for information on recovery or recycling
P503	Refer to manufacturer/supplier... for information on disposal/recovery/recycling.

List of hazardous substances used according to the GHS

List of used GHS-classified substances in the work presented here.

Substance (CAS#)	Pictogram	Hazard (H) statements	Precautionary (P) statements
Acetic acid (64-19-7)	GHS02, GHS05	H226, 314	P210, 233, 240, 241, 242, 243, 260, 264, 280, 301+330+331, 303+361+353, 304+340, 305+351+338, 310, 321, 363, 370+378, 403+235, 405, 501
Acrylamide (79-06-1)	GHS06, GHS07, GHS08	H301, 312, 315, 317, 319, 332, 340, 350, 361f, 372	P201, 202, 260, 261, 264, 270, 271, 272, 280, 281, 301+310, 302+352, 304+312, 304+340, 305+351+338, 308+313, 312, 314, 321, 322, 330, 332+313, 333+313, 337+313, 362, 363, 405, 501
Ampicillin disodium salt (69-52-3)	GHS07, GHS08	H317, 334	P261, 272, 280, 285, 302+352, 304+341, 321, 333+313, 342+311, 363, 501
Ammonium persulfate (APS) (7727-54-0)	GHS03, GHS07, GHS08	H272, 302, 315, 317, 319, 334, 335	P210, 220, 221, 261, 264, 270, 271, 272, 280, 285, 301+312, 302+352, 304+340, 304+341, 305+351+338, 312, 321, 330, 332+313, 333+313, 337+313, 342+311, 362, 363, 370+378, 403+233, 405, 501
Benzamidine hydrochloride hydrate (206752-36-5)	GHS07	H315, 319, 335	P261, 264, 271, 280, 302+352, 304+340, 305+351+338, 312, 321,

			332+313, 337+313, 362, 403+233, 405, 501
Bromophenol blue sodium salt (62625-28-9)	GHS07	H315, 319, 335	P261, 264, 271, 280, 302+352, 304+340, 305+351+338, 312, 321, 332+313, 337+313, 362, 403+233, 405, 501
(+)-Bicuculline (485-49-4)	GHS06, GHS09	H300, 311, 331, 400	P260, 264, 273, 280, 301+310, 302+352, 304+340
Chloramphenicol (56-75-7)	GHS05, GHS07, GHS08	H317, 318, 350, 351, 360, 361	P201, 202, 261, 272, 280, 281, 302+352, 305+351+338, 308+313, 310, 321, 333+313, 363, 405, 501
cOmplete, EDTA-free protease inhibitor tablets (Roche)	GHS05	H314	P260, 280, 301+330+331, 303+361+353, 304+340+310, 305+351+338+310
Copper sulfate (7758-98-7)	GHS07, GHS09	H302, 315, 319, 400, 410	P264, 270, 273, 280, 301+312, 302+352, 305+351+338, 321, 330, 332+313, 337+313, 362, 391, 501
D-(-)-2-Amino-5-phosphonopentanoic acid (D-APV) (79055-68-8)	GHS07	H315, 319, 335	P261, 264, 271, 280, 302+352, 304+340, 305+351+338, 312, 321, 332+313, 337+313, 362, 403+233, 405, 501
Dibasic sodium pyrophosphate (DSPP) (7758-16-9)	GHS07	H319	P305+351+338
Dimethylsulfoxide (DMSO) (67-68-5)	GHS07	H315, 319, 335	P261, 264, 271, 280, 302+352, 304+340, 305+351+338, 312, 321, 332+313, 337+313, 362, 403+233, 405, 501
Dithiothreitol (DTT) (3483-12-3)	GHS05, GHS07	H302, 315, 318	P264, 270, 280, 301+312, 302+352, 305+351+338
Ethylenediaminetetraacetic acid (EDTA) (6381-92-6)	GHS07, GHS08	H302, 312, 315, 319, 332, 335, 373, 412	P260, 261, 264, 270, 271, 273, 280, 301+312, 302+352, 304+312, 304+340, 305+351+338, 312, 314, 321, 322, 330, 332+313, 337+313, 362, 363, 403+233, 405, 501
Ethanol (64-17-5)	GHS02	H225	P210, 233, 240, 241, 242, 243, 280, 303+361+353, 370+378, 403+235, 501
Formaldehyde (ROTI Histofix, 10% solution, phosphate buffered, pH 7) (50-00-0)	GHS05, GHS06, GHS07, GHS08	H302+312, 315, 317, 319, 335, 341, 350, 371	P260, 280, 302+352, 305+351+338, 308+313

2-[4-(2-Hydroxyethyl)piperazin-1-yl]ethane-1-sulfonic acid (HEPES) (7365-45-9)	GHS07	H315, 319, 335,	P280, 301+312, 302+352, 304+312, 304+340, 305+351+338, 321, 322, 330, 332+313, 337+313, 362, 363, 403+233, 405, 501
Hydrochloric acid (7647-01-0)	GHS05, GHS06	H314, 331	P260, 261, 264, 271, 280, 301+330+331, 303+361+353, 304+340, 305+351+338, 310, 311, 321, 363, 403+233, 405, 501
Hydrogen peroxide (7722-84-1)	GHS03, GHS05, GHS07	H271, 302, 314, 332	P210, 220, 221, 260, 261, 264, 270, 271, 280, 283, 301+312, 301+330+331, 303+361+353, 304+312, 304+340, 305+351+338, 306+360, 310, 312, 321, 330, 363, 370+378, 371+380+375, 405, 501
Imidazole (288-32-4)	GHS05, GHS07, GHS08	H302, 314, 360D	P201, 202, 260, 264, 270, 280, 281, 301+312, 301+330+331, 303+361+353, 304+340, 305+351+338, 308+313, 310, 321, 330, 363, 405, 501
4-Iodophenylboronic acid (4-IPBA) (5122-99-6)	GHS07	H302, 315, 319, 335	P261, 264, 270, 271, 280, 301+312, 302+352, 304+340, 305+351+338, 312, 321, 330, 332+313, 337+313, 362, 403+233, 405, 501
Isopropanol (67-63-0)	GHS02	H228	P210, 240, 241, 280, 370+378
Isopropyl-β-D-thiogalactopyranoside (IPTG) (367-93-1)	GHS07, GHS08	H319, 351	P281, 305+351+338
Kanamycin sulfate (25389-94-0)	GHS08	H360	P201, 202, 281, 308+313, 405, 501
L-Azidohomoalanine hydrochloride (942518-29-8)	GHS02	H242	P210, 234, 235, 240, 370+378, 403
Luminol (521-31-3)	GHS07	H302, 315, 319, 335	P261, 264, 270, 271, 280, 301+312, 302+352, 304+340, 305+351+338, 312, 321, 330, 332+313, 337+313, 362, 403+233, 405, 501
Lysozyme (12650-88-3)	GHS08	H334	P261, 284, 501
2-Mercaptoethanol (60-24-2)	GHS05, GHS06, GHS07,	H301, 302, 310, 311, 314, 315,	P201, 202, 260, 261, 262, 264, 270, 271, 272, 273, 280, 281, 301+310,

	GHS08, GHS09	317, 318, 331, 332, 361, 373, 400, 410, 411	301+312, 301+330+331, 302+350, 302+352, 303+361+353, 304+312, 304+340, 305+351+338, 308+313, 310, 311, 312, 314, 321, 322, 330, 332+313, 333+313, 361, 362, 363, 391, 403+233, 405, 501
Methanol (67-56-1)	GHS02, GHS06, GHS08	H225, 301, 311, 331, 370	P210, 233, 240, 241, 242, 243, 260, 261, 264, 270, 271, 280, 301+310, 302+352, 303+361+353, 304+340, 307+311, 311, 312, 321, 322, 330, 361, 363, 370+378, 403+233, 403+235, 405, 501
Nitric acid	GHS03, GHS05, GHS06	H272, 290, 314, 331	P220, 260, 280, 303+361+353, 305+351+338, 310
N, N'- Methylenebisacrylamide (110-26-9)	GHS05, GHS06, GHS07, GHS08	H301, 302, 312, 317, 318, 332, 340, 350, 351, 360, 361, 372	P201, 202, 260, 261, 264, 270, 271, 272, 280, 281, 301+310, 301+312, 302+352, 304+312, 304+340, 305+351+338, 308+313, 310, 312, 314, 321, 322, 330, 333+313, 363, 405, 501
N, N, N', N'- Tetramethylethane-1,2-diamine (TEMED) (110-18-9)	GHS02, GHS05, GHS06	H225, H301+331, 314	P210, 233, 280, 303+361+353, 304+340+310, 305+351+338
Nonyl phenoxypolyethoxyl-ethanol (NP-40) (26027-38-3)	GHS05, GHS07, GHS09	H302, 315, 318, 319, 400, 410, 411	P264, 270, 273, 280, 301+312, 302+352, 305+351+338, 310, 321, 330, 332+313, 337+313, 362, 391, 501
Polyethylenimine (PEI) (49553-93-7)	GHS07	H312, 315	P280, 285, 302+352, 305, 313, 351
Potassium fluoride (7789-23-3)	GHS05, GHS06	H301+311+331, 318	P261, 280, 301+310, 302+352+312, 304+340+311, 305+351+338
Potassium hydroxide (1310-58-3)	GHS05, GHS07	H302, 314	P260, 264, 270, 280, 301+312, 301+330+331, 303+361+353, 304+340, 305+351+338, 310, 321, 330, 363, 405, 501
Sodium azide (26628-22-8)	GHS06, GHS08, GHS09	H300, 310, 330, 373, 410	P270, 273, 280, 302+352, 304+340, 310
Sodium dodecyl sulfate (SDS) (151-21-3)	GHS02, GHS05, GHS07	H228, 302+332, 315, 318, 335, 412	P210, 261, 280, 302+352, 305+351+338, 312

Sodium hydroxide (1310-73-2)	GHS05	H314	P260, 264, 280, 301+330+331, 303+361+353, 304+340, 305+351+338, 310, 321, 363, 405, 501
Sodium molybdate dihydrate (10102-40-6)	GHS07	H302, 312, 315, 319, 332, 335, 412	P261, 264, 270, 271, 273, 280, 301+312, 302+352, 304+312, 304+340, 305+351+338, 312, 321, 322, 330, 332+313, 337+313, 362, 363, 403+233, 405, 501
Sodium orthovanadate (13721-39-6)	GHS07	H302+312+332, 315, 319	P261, 280, 301+312, 302+352+312, 304+340+312, 305+351+338
Sulfuric acid (7664-93-9)	GHS05	H290, 314	P280, 301+330+331, 303+361+353, 305+351+338, 310
Tetrodotoxin (TTX) (4368-28-9)	GHS06	H300, 310, 330	P260, 262, 264, 280, 284, 301+310, 302+350, 304+340
Tris-(hydroxymethyl)-aminomethane (TRIS) (77-86-1)	GHS07	H315, 319, 335	P261, 264, 271, 280, 302+352, 304+340, 305+351+338, 312, 321, 332+313, 337+313, 362, 403+233, 405, 501
Tris[(1-benzyl-1H-1,2,3-triazol-4-yl)methyl]amine (TBTA) (510758-28-8)	GHS07	H315, 319, 413	P273, 501
Tris-(2-carboxyethyl)-phosphine hydrochloride (TCEP) (51805-45-9)	GHS05	H314, 318	P260, 280, 303+361+353, 304+340+310, 305+351+338, 363
2-[4-(2,4,4-trimethylpentan-2-yl)phenoxy]ethanol (Triton X-100) (9002-93-1)	GHS05, GHS07, GHS09	H302, 315, 318, 319, 400, 410, 411, 412	P264, 270, 273, 280, 301+312, 302+352, 305+351+338, 310, 321, 330, 332+313, 337+313, 362, 391, 501
Trypsin-EDTA (9002-07-7)	GHS08	H334	P261, 284, 342+311, 304+340, 501

Acknowledgements

During my doctoral studies many great and inspiring people accompanied me, scientifically but also privately, and have shaped my way. This work would not have been possible without their support, assistance, and guidance.

First, I would like to thank my parents for giving me the freedom to explore and pursue my own direction. I am very grateful for your support during all the years of my education, especially during my studies in Tyrol and Hamburg. Without your support throughout the years, I would have never made it to this point.

My deepest gratitude goes to my girlfriend Berit, who I had the pleasure to meet shortly after moving to Hamburg. In you I have found a person with whom I can share not only my passion for music but also for neuroscience. Your continuous and loving patience, empathy, encouragement, understanding and motivation has given me the strength to finish this work. I am more than happy to pursue my future path together with you.

Furthermore, I would like to thank my supervisors Marina Mikhaylova and Michael Kreutz for the possibility to conduct my doctoral studies in their groups. Being a classical chemist by training made it particularly challenging to perform my doctoral studies in a neuroscientific research environment. I initially started as a joint PhD student of Marina and Michael and later fully joined Marina's team. This was giving me the possibility to work in many different environments, laboratories and research institutions including the ZMNH as well as the Leibniz Institute for Neurobiology (LIN) in Magdeburg. I very much appreciate the opportunity of working in a highly interdisciplinary team, where people share their knowledge and expertise from multiple different areas. Specifically, I appreciate the help and guidance of Julia and Bas, two great scientists who have introduced me not only to many different techniques used in the lab including immunocytochemistry and TIRF microscopy but also supported me in many organizational questions after moving to Hamburg. Both of you have made my start in Hamburg and in the lab a lot easier. I wish you all the best and a lot of success in Berlin.

During this period, I was also lucky to collaborate with many excellent scientists from different countries and institutions. Special thanks go to Dmitry Molodenskiy and Dmitri Svergun from the BioSAXS group at EMBL Hamburg for their assistance and guidance with SAXS experiments at the P12 beamline. Additionally, I am very thankful for the help of Stephan Niebling and the team of the SPC facility at EMBL Hamburg for the possibility to conduct most of the biophysical characterization experiments in their facility. I had a great time performing experiments and measurements at the SPC facility in a very open, helpful, and supportive environment with many educative and fruitful discussions. At that time Prof. Alla Kostyukova was visiting the lab as a guest professor and I had the pleasure to collaborate with her during her stay in Germany. Being a specialist for protein biophysics in general and CD spectroscopy in particular, Alla was teaching me a lot about CD spectroscopy of proteins. I really enjoyed the discussions with you, and I wish you all the best for your main lab at the Washington State University (WSU). I would also like to thank Rajeev Raman from the LIN for introduction to and assistance with fluorescence spectroscopy experiments. Furthermore, thanks to Jeroen Demmers and Dick Dekkers from the Erasmus MC proteomics facility in Rotterdam for their help with mass spectrometry. I also want to thank Jasper Grendel from our lab for his help with the

114

Curriculum Vitae

Personal Data

Name: Michael Bucher

Date of Birth: 14.06.1993

Place of Birth: Innsbruck

Nationality: Austria

Education

2017 – 2022	**PhD candidate at the Institute of Biochemistry and Molecular Biology** (*University of Hamburg & Center for Molecular Neurobiology Hamburg (ZMNH) & Leibniz Institute for Neurobiology (LIN) Magdeburg*) Thesis: "Characterization of the structural and functional impact of autism-associated SHANK3 missense mutations" Supervisors: Prof. Dr. Marina Mikhaylova and Prof. Dr. Wolfram Brune Co-supervisors: Prof. Dr. Matthias Kneussel and Dr. Michael R. Kreutz
Jan. 2016 – Apr. 2017	**M.Sc. student at the Institute of Biochemistry** (*Center for Chemistry and Biomedicine, University of Innsbruck*) Thesis: "Analyses of binary transcription factor and kinase:effector interactions" Supervisors: PD Dr. Eduard Stefan and Prof. Dr. Georg Dechant
Oct. 2014 – Jan. 2016	**Master's Programme in Chemistry** (*Center for Chemistry and Biomedicine, University of Innsbruck*)
Since Oct. 2014	**Diploma Programme in Pharmacy** (*Center for Chemistry and Biomedicine, University of Innsbruck*) completed first diploma examination by Oct 2015
Oct. 2011 – Sep. 2014	**Bachelor's Programme in Chemistry** (*Center for Chemistry and Biomedicine, University of Innsbruck*) Thesis: "Characterization of recombinant CAD:PKA complexes" Supervisor: PD Dr. Eduard Stefan
2007 – 2011	**High school with focus on "Biology and Ecology"** (*PORG Volders, Tyrol, Austria*) A-levels examination in June 2011 (passed with distinction)

Scientific Techniques

- Expression, isolation, and purification of recombinant proteins (IMAC, SEC)
- Biophysical characterization of purified proteins (SAXS, CD spectroscopy, nanoDSF, fluorescence spectroscopy)
- Molecular dynamics simulations (GROMACS)
- Qualitative and quantitative assessment of protein:protein interactions (IP, pulldown assays, protein-fragment complementation)
- Microscopy techniques (TIRF-FRAP, spinning disk and laser scanning confocal microscopy, live imaging)
- Peptide-array based mapping of protein:protein interaction sites
- Molecular cloning and site-directed mutagenesis
- Standard cell culture and transfection of mammalian cells; preparation of mouse and rat hippocampal primary neuron cultures

Grants and Contributions

- EMBL project proposal for BioSAXS beam time (P12 beamline, PETRA III, EMBL/DESY, Hamburg, Germany)
  Title: *Structural and functional insights on the calcium-dependent regulation of myosin V via caldendrin*
- iNEXT grant for for BioSAXS beam time (P12 beamline, PETRA III, EMBL/DESY, Hamburg, Germany)
  Title: *The molecular identity of autistic synapses: A SHANK3 perspective*
- Travel grant for the EMBO workshop on molecular neurobiology (Fodele, Crete, 2018)

Sep. 2019	**IBRO Satellite Meeting on "Synaptic Function and Neural Circuitry" (Busan, South Korea)** *Short talk: The molecular identity of autistic synapses: A SHANK3 perspective*
May 2019	**EMBO Workshop on the "Characterization of post-translational modifications in cellular signalling" (Odense, Denmark)** *Poster: The molecular identity of autistic synapses: A SHANK3 perspective* (Michael Bucher, Jasper Grendel, Friederike Schröder, Michael R. Kreutz and Marina Mikhaylova) – EMBO Poster prize
May 2018	**EMBO Workshop on Molecular Neurobiology (Fodele, Crete)** *Poster: The molecular identity of autistic synapses: A SHANK3 perspective* (Michael Bucher, Rajeev Raman, Hans-Jürgen Kreienkamp, Dmitry Molodenskiy, Dmitri Svergun, Rob Meijers, Michael R. Kreutz and Marina Mikhaylova)

Additional education

Apr. 2019	Advanced training course according to the German Federal Law "Gentechnik-Sicherheitsverordnung" (GenTSV §15) *(BioMedConcept GmbH, Berlin, Germany)*
Nov. 2018	GE Healthcare - Customized Biacore™ Training *(EMBL Hamburg, Germany)*
Jan. 2018	Training course "Planning and execution of animal experiments on the mouse" *(Animal facility, University Medical Center Hamburg-Eppendorf, Germany)*

Teaching Experience

Feb. 2022	Advanced module Experimental Biophysics *(Humboldt-University of Berlin)* Lecture: Methoden zur Analyse von Proteinstruktur und -dynamik
Mar. 2015 – Jul. 2016	Laboratory Course in Basic Biochemistry for Chemists and Laboratory Course in Basic Biochemistry and Molecular Biology for Pharmacists *(Center for Chemistry and Biomedicine, University of Innsbruck)* student assistant
Oct. 2014 – Jul. 2015	Tutor for the basic lectures "Organic Chemistry I" and "Organic Chemistry II" for Chemists *(Center for Chemistry and Biomedicine, University of Innsbruck)*

Activities

Aug. 2015 – Sep. 2015	Studies on isolation and chemical purification methods for an experimental protein kinase C (PKC) inhibitor at Sandoz GmbH, Kundl
Aug. 2013 – Sep. 2013	Optimization studies on isolation of periplasmic expressed proteins and HPLC in-process-analytics at Sandoz GmbH, Kundl

Languages

- German: native
- English: fluent

Eidesstattliche Versicherung

Hiermit versichere ich an Eides statt, die vorliegende Dissertation selbst verfasst und keine anderen als die angegebenen Hilfsmittel benutzt zu haben. Die eingereichte schriftliche Fassung entspricht der auf dem elektronischen Speichermedium. Ich versichere, dass diese Dissertation nicht in einem früheren Promotionsverfahren eingereicht wurde.

_____

Datum, Unterschrift